The pulse shape of optical cerenkov radiation from extensive air showers

Andam, A. A.

THE PULSE SHAPE OF OPTICAL CERENKOV RADIATION FROM EXTENSIVE AIR SHOWERS

A. A. ANDAM, B.Sc.,M.Sc.

A Thesis submitted to the University of Durham in accordance with the Regulations for Admittance to the Degree of Doctor of Philosophy

Department of Physics
University of Durham

September 1981

CONTENTS

ACKNOWLEDGEMENTS.

I am grateful to Dr. K. J. Orford, my supervisor, for continued encouragement and criticism. My thanks also go to Dr. K. E. Turver for many helpful discussions.

Financial support for my research was provided by the Government of Ghana. This is gratefully acknowledged.

Professor B. H. Bransden and Professor A. W. Wolfendale are thanked for provision of research facilities in the Department of Physics, University of Durham.

I thank all members of the Extensive Air Showers Research Group, University of Durham (1978 - 1981) for their co-operation.

ABSTRACT

This Thesis is concerned with the computation and interpretation of Cerenkov light pulse shapes from digitised pulses.

The experiment to measure the characteristics of extensive air showers in the energy range 10^{15} eV - 10^{18} eV was conducted at the University of Durham EAS array in Dugway, UTAH, USA between 1977 and 1980. Systematic environmental monitoring of the experiment has been carried out to quantify weather conditions and assess data quality.

Computer programs have been developed and tested to retrieve pulse shape information from digitised Cerenkov light data. Three main data fitting methods are investigated and compared, and the theories underlying them are outlined.

A sample of the Dugway data has been analysed in detail after pulse shape reconstruction using unimodal quartic splines. The measured pulse shape parameters are interpreted to show the electron cascade development of the extensive air showers, and related to a proposed primary energy estimator. Suggestions are made for further pulse shape reconstruction techniques.

CHAPTER ONE

INTRODUCTION

1.1 Historical Background.

In 1900 C. T. R. Wilson, the originator of the Wilson Cloud Chamber, observed that an insulated gold leaf electroscope lost its charge even when the greatest care was taken to insulate it from known radiations. He attributed this residual conductivity to a radiation that ionized the gas in the electroscope (Wilson, 1901).

A decade later, Hess (1912) showed from the results of balloon flights, carrying electroscopes to altitudes of a few kilometres, that the ionisation decreased with height above sea level up to $\sim$ 700m and then increased again to as much as ten times its sea level value at $\sim$ 9km. The decrease in ionisation was due to a decrease in the contribution from the Earth's radioactivity, whilst the increase was interpreted as the effect of a corposcular radiation coming from outer space. This extra-terrestrial radiation was named "cosmic radiation" by Millikan (1939). Further experiments showed that cosmic rays were mainly positively charged and were more penetrating than gamma-radiation, the most penetrating radiation known at that time.

1.2 The Cosmic Radiation.

Hess's discovery of cosmic rays was important because it meant

that scientists now had access to a direct sample of matter originating from outside our solar system. As the radiation is a highly concentrated form of energy, exceeding the energy range of laboratory particle accelerators, it gives evidence to processes occuring in the cosmos that are still accessible only to speculation.

The cosmic ray spectrum makes up only a small part of the total radiation spectrum; yet its investigation has led to many discoveries in Physics. These include the discovery of the μ-meson and π-meson. The construction of high-energy particle accelerators, around the middle of this century, as sources more convenient and controllable than cosmic rays, was largely based on results from cosmic ray research.

Interest in the astrophysical aspects of cosmic rays is mainly centred on possible answers to three main questions :

(1) What is the energy spectrum of the radiation ?

(2) What is the mass composition of the radiation ?

and (3) Where do these rays originate from ?

Answers to these questions might contribute not only to our understanding of the Galaxy and the possible effects of the radiation on our Planet, but also the history of the universe.

1.2.1 The Energy Spectrum.

It is now well established that the cosmic radiation is made up of particles and photons with an energy range which extends from less than 10^9 eV to an upper limit greater than 10^{19} eV per nucleon. The

integral energy spectrum has been represented by a simple power law of the form

$$N(>E) \propto E^{-\gamma} \qquad 1.1$$

The exponent, γ, changes slowly with energy from $\sim$ 1.6 in the low energy range 10^{11} eV - 10^{15} eV (Grigorov et al, 1971) to $\sim$ 2.4 in the steeper region (after the "knee") between $\sim$ 3 x 10^{15} eV and 10^{17} eV.

The shape of the energy spectrum at the ultra high energy region ($\gtrsim$ 10^{18} eV) is rather controversial (Krasilnikov, 1973). As Figure 1.1 shows, recent experimental results do not all agree on the slope of the energy spectrum in this region. What seems clear is that γ does not increase substantially beyond $\sim$ 2.4 in the high energy ranges and might possibly even decrease. This, however, will have to be confirmed by further experiments.

The vast energy range of the primary energy spectrum precludes any attempt to study the whole spectrum by a single technique. Figure 1.2 gives a summary of the different methods used to measure the primary energy (Wolfendale, 1975). At energies below $\sim$ 10^9 eV direct satellite measurements can be made to yield information about the predominantly low mass particles.

Between 10^9 eV and $\sim$ 5 x 10^{11} eV most of the information about the primary spectrum has been obtained by balloon experiments. Measurements up to this upper limit have been classified, therefore,

FIGURE 1.1

THE PRIMARY ENERGY SPECTRUM (Juliusson, 1975)

FIGURE 1.2

SUMMARY OF MEASUREMENTS OF SOME OF THE PRIMARY COSMIC RAY COMPONENTS (Wolfendale, 1975)

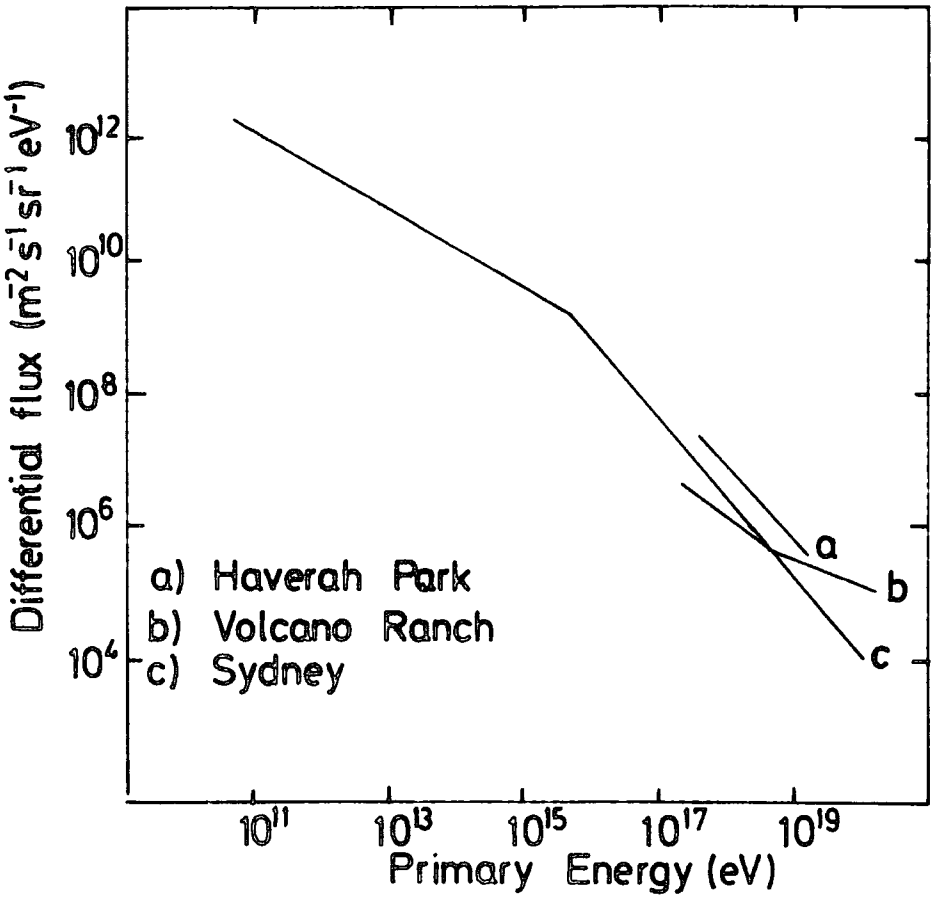
Differential flux (m⁻² s⁻¹ sr⁻¹ eV⁻¹)
10¹²
10¹⁰
10⁸
10⁶
10⁴
a) Haverah Park
b) Volcano Ranch
c) Sydney
a
b
c
10¹¹
10¹³
10¹⁵
10¹⁷
10¹⁹
Primary Energy (eV)

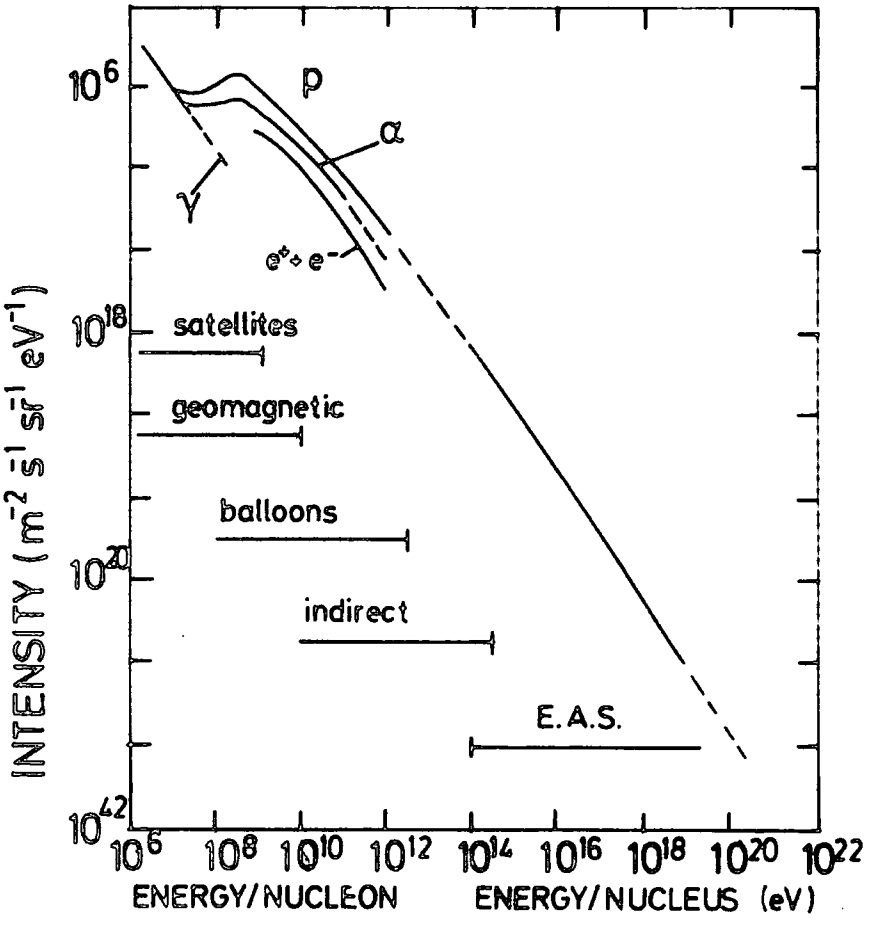
INTENSITY (m⁻² s⁻¹ sr⁻¹ eV⁻¹)
10⁶
10¹⁸
10²⁰
10⁴²
p
α
γ
e⁺+e⁻
satellites
geomagnetic
balloons
indirect
E.A.S.
10⁶
10⁸
10¹⁰
10¹²
10¹⁴
10¹⁶
10¹⁸
10²⁰
10²²
ENERGY/NUCLEON
ENERGY/NUCLEUS (eV)

as "direct", in contrast to indirect measurements on energies above $\sim 5 \times 10^{11}$ eV which are obtained by extrapolating results from sea-level muons and other particle studies. Above $\sim 10^{14}$ eV, studies of Extensive Air Showers provide a reliable means of obtaining information on the primary cosmic radiation.

1.2.2 The Mass Spectrum.

The mass composition of primary cosmic rays is not known to the same extent as the energy spectrum is known. Current available data indicate that the major constituent of the primary is a mixture of protons, alpha particles and heavier nuclei (mainly iron).

Table 1.1 gives a summary of results from experiments conducted to investigate the mass composition of the primary cosmic radiation. These observations confirm that heavy nuclei are present up to energies of the order of $\sim 4 \times 10^{14}$ eV.

Interest in the mass composition of the primary has been stimulated by the possibility of relating the mass to their place of origin. The particles are affected by the media through which they travel, by interaction as well as deflection in the galactic magnetic field. Heavy nuclei may be expected to be shorter lived than protons because of the greater probability of suffering collisions with interstellar atoms. The mass spectrum would then become more protonic with increasing energy.

On the other hand iron nuclei, with their higher charge, are less magnetically rigid than protons and would be expected to be contained in our Galaxy while protons will be expected to escape. An observed

TABLE 1.1

EXPERIMENTAL DATA ON THE MASS COMPOSITION OF THE PRIMARY COSMIC RADIATION.

energy (eV)	total no of events	percentage of protons and neutrons	percentage of α particles	percentage of heavier nuclei	Reference
3.7×10^{11}	46	80	13	7	Malhotra et al(1966)
$> 10^{12}$	112	46	16	38	McCusker (1967)
universal composition	——	≈ 99	< 1	$< .02$	——

primary cosmic radiation with predominant protonic flux would therefore indicate an extra-galactic source.

1.2.3 Some Theories on the Possible Origin of Cosmic Rays.

The exact origin of the cosmic radiation is still an unsolved problem. Any theory on the origin of the radiation must explain both the production and the acceleration machanism of the cosmic ray nuclei.

The very high energies observed led to assumptions that the sources might be unusual objects. Supernovae seem capable of providing such high energies (Ginzburg and Syrovatskii, 1964) and if cosmic rays were confined to our galaxy they would be acceptable as possible sources. Other stars and novae, the Sun, Galactic centre and pulsars have been proposed as plausible cosmic rays sources.

Experimental evidence indicates an all-isotropic distribution pervading space. The main reason for this might be that interstellar magnetic fields smear out any large directional anisotropies expected of Galactic-originated primaries, although the sources themselves might be discrete.

Marsden et al (1976) have reported a high anisotropy around 10^{11}eV - 10^{12} eV in a direction approximately parallel to the spiral arms in our region of the Galaxy. Osborne et al (1977) explained this anisotropy as the effect of particles from the Vela pulsar. There appears to be, therefore, some support for a galactic origin for low energy cosmic rays.

The propagation modes of the primary cosmic rays at higher energies indicate that they are unlikely to arrive at the Earth isotropically.

Pollock and Watson (1975) have reported that there is some evidence of anisotropy for ultra high energy cosmic rays near 10^{17} eV.

Above $\sim 10^{19}$ eV Berezinsky and Zatsepin (1969, 1971) have proposed that neutrinos, produced as secondaries of the interactions between protons and microwave photons in the metagalaxy, could be responsible for the cosmic radiation.

The search for the origin of cosmic rays is intertwined with questions on the mass composition, for a firm knowledge of the mass might rule out some of the proposed sources.

1.3 Extensive Air Showers.

There is strong interaction between the nuclei of atmospheric atoms and the primary cosmic ray particles incident at the top of the atmosphere. Such an interaction produces mesons and nucleons which form a compact "core" proceeding not far from the original direction of the initiating particles.

Further interaction occurs between these secondary mesons and nucleons, and the nuclei of other atmospheric atoms at lower levels of the atmosphere. Hence a "chain reaction" is set up in which several interactions take place while the primary particle is traversing the 1030 g cm^{-2} of atmosphere before reaching sea level. This atmospheric thickness constitutes about 12 interaction lengths for the nucleons.

With the atmosphere effectively acting as a particle amplifier, the resulting nucleon cascade is very much spread out into a shower of particles, suitably called an "Extensive Air Shower". Figure 1.3 shows the development of an extensive air shower (Kellerman, 1976).

The primary particle loses about half its initial energy at each

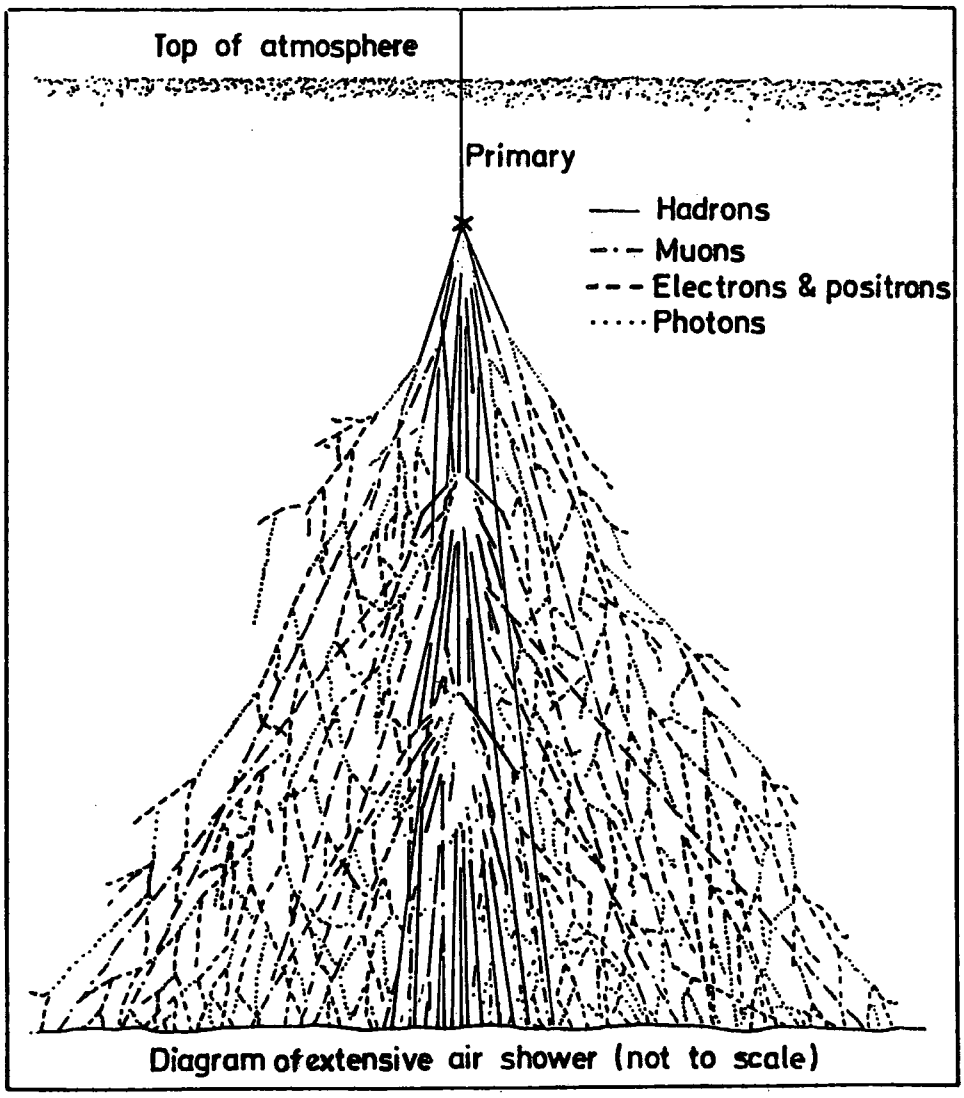

FIGURE 1.3

THE PARTICLE FORMATION IN AN EXTENSIVE AIR SHOWER.

(Kellerman , 1976)

interaction, (Matano et al, 1963), producing the nuclear-active particles. These are mostly pions together with kaons, nucleons, anti-nucleons and other strange particles. The interaction length of pions in air is short ($\sim$120 g cm^{-2}) and the pions quickly decay into muons, supplying the EAS with its highly penetrating muonic component. The neutral pions, with a lifetime of 10^{-16} s decay even faster than charged pions (lifetime of a charged pion is 2.6×10^{-8} s) and each resultant gamma-ray is then capable of initiating a photon-electron cascade.

1.3.1 Cascade Processes.

The nucleons and interacting pions, known collectively as the hadrons, average only about 10% of the shower; but they carry typically about 80% of the total energy. The EAS therefore consists of a large number of cascades, comprising a compact hadronic central core surrounded by an electron-photon component that is continuously nourished by decaying π°-mesons.

Cascade processes in EAS occur as a direct result of the various charges residing on the primary particles, and the electromagnetic and other processes of the shower components. A photon in the EAS, under the right conditions of the strong electric field surrounding an atomic nucleus in the atmosphere, can materialize into an electron-positron pair.

An electron of sufficiently high energy, approaching an atomic nucleus in the atmosphere, can also emit electromagnetic radiation. This is a consequence of the interaction of the electron in the Coulomb field of the nucleus, and is only possible if the closest distance of approach

is smaller than the atomic dimensions.

The effect of these processes of pair production, bremsstrahlung and ionization is a lateral spread of the EAS and a reduction of the energies of the particles. When the energies are reduced below a critical level at which ionisation becomes the dominant energy loss mechanism ($\sim$ 84 MeV in air), multiplication of the electromagnetic component ceases.

1.3.2 Observable Quantities.

As a result of the large lateral spread of the various components of an EAS, ground based particle and photon detection is possible. A typical EAS array comprises several particle and/or photon detectors spread over a large ground area of several km^2. These detectors measure the total light intensity, or particle density, depending on which component is under observation. Measurements are usually recorded when the array triggering criterion, often defined as the coincidences in two or more detectors, is met.

From the records computation of such shower parameters as the arrival direction of the shower, the accurate air shower core, electron number and photon density is made. These parameters contribute, through interpolation or extrapolation, to the evaluation of a primary energy estimator for the particular EAS array. For example, the electron number has been used as a primary energy estimator at the Volcano Ranch array, whereas the muon number is used at Sydney. At the Haverah Park array the electron densities recorded by water Cerenkov detectors, interpolated at 500m and 600m from the core, are used as primary energy estimators. The total Cerenkov light intensity at 100m and 150m from

the core have been proposed as energy estimators at Dugway. The philosophy behind this proposal, and the consequences of it to cosmic ray measurements at this array, will be outlined later in this Thesis.

1.4 Scope of This Work.

This work is primarily concerned with the computation and interpretation of Cerenkov light pulse shapes from the Dugway EAS array. The experiment to measure the characteristics of extensive air showers in the energy range 3×10^{15} eV to 2×10^{18} eV was conducted at the University of Durham EAS array in Dugway, UTAH, USA between 1977 and 1980.

The author was responsible for analysing the environmental monitoring of the experiment from 1978 to 1980. This involved the analysis of sky films and keeping up-to-date weather records to determine acceptable data prior to analysis. She also contributed to the analysis of the data, particularly in the area of pulse shape reconstruction.

Computer programs have been developed and tested to retrieve pulse shape information from the digitised Cerenkov light data from Dugway. Three main fitting procedures have been developed and tested.

This Thesis outlines the main data fitting procedures and compares them. The average pulse shape characteristics of the Cerenkov light measured at the Dugway array are given, as well as correlations between pulse shape parameters and other characteristics of the extensive air showers.

The measured pulse shape parameters are interpreted to show the cascade development of the extensive air showers and related to a proposed primary energy estimator at Dugway.

CHAPTER TWO

ATMOSPHERIC CERENKOV RADIATION

2.1 Introduction.

A charged particle traversing a dielectric polarizes the medium in the region of its track. Cerenkov (1934, 1937) was the first to observe the radiation that is emitted as a result of this polarization, if the velocity of the charged particle is greater than the phase velocity of light in the medium. His observation was the practical evidence of the classical electromagnetic theory of the Cerenkov effect proposed by Frank and Tamm (1937). The discussion in Section 2.2 is a simplified account of the basic principles of the Cerenkov effect.

2.2 The Physical Basis of the Cerenkov Effect.

For a simple case we consider one electron of velocity, v, moving through a dielectric medium. The individual atoms of the medium in the region close to the traversing electron will undergo distortion, Figure 2.1(a), as a direct result of the displacement of the negative charges of the atoms to one side. Any subsequent displacement of charge results in polarization at a different point, P', say, in the medium. Hence the passage of the particle through the medium will result in a very brief electromagnetic pulse at each elemental region of the medium. For a slowly moving particle, the resultant polarization field is completely symmetrical along the axis and in azimuth and no radiation occurs.

On the other hand, if the velocity of the electron, v, is large

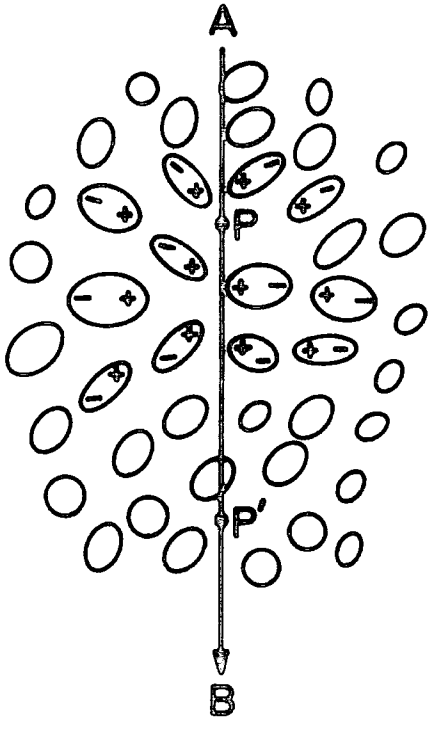

Fig. 2.1(A)

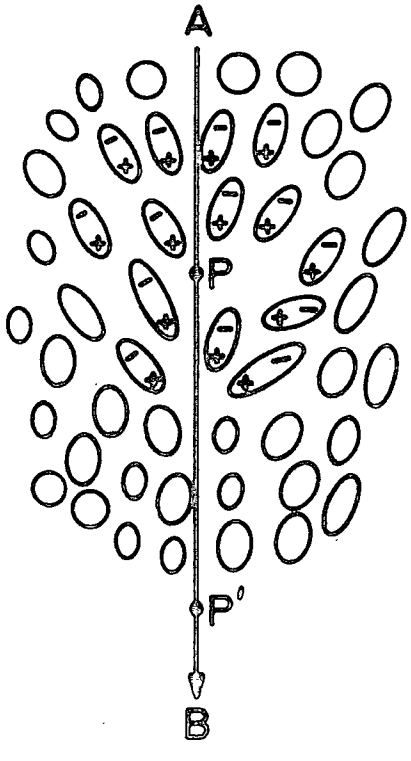

Fig. 2.1(B)

FIGURE 2.1

THE POLARIZATION SET UP IN A DIELECTRIC BY THE PASSAGE OF A CHARGED PARTICLE (A) AT LOW VELOCITY (B) AT HIGH VELOCITY.

compared with the velocity of light in the medium, the polarization field is no longer symmetrical along the axis, Figure 2.1(b). A brief electromagnetic pulse is radiated as a result of a momentary dipole field set up by the electron. Figure 2.2 is a schematic representation of the Huygens' construction of the light wavelets set up in this situation. A very fast particle, travelling at a velocity higher than the phase velocity of light in the medium can therefore set up such wavelets which result in a field if they are in phase with one another.

As shown in Figure 2.2, coherence of the wavelets occurs if the time taken by the particle to travel the track AB, $\Delta\tau$, is the same as the time light travels from A to C.

Hence the angle, θ , at which the wavelets from all points (such as P_1 , P_2 , P_3) on the track are coherent is given by

$$\cos\theta = \frac{1}{\beta n} \qquad 2.1$$

where n is the refractive index of the medium and the velocity of the particle, $v = \beta c$ (c = velocity of light).

Equation 2.1 is the fundamental Cerenkov relation from which three deductions may be made, for a medium of refractive index, n .

(1) At a critical velocity given by

$$\beta_{min} = \frac{1}{n} \qquad 2.2$$

the direction of radiation coincides with that of the particle. Cerenkov

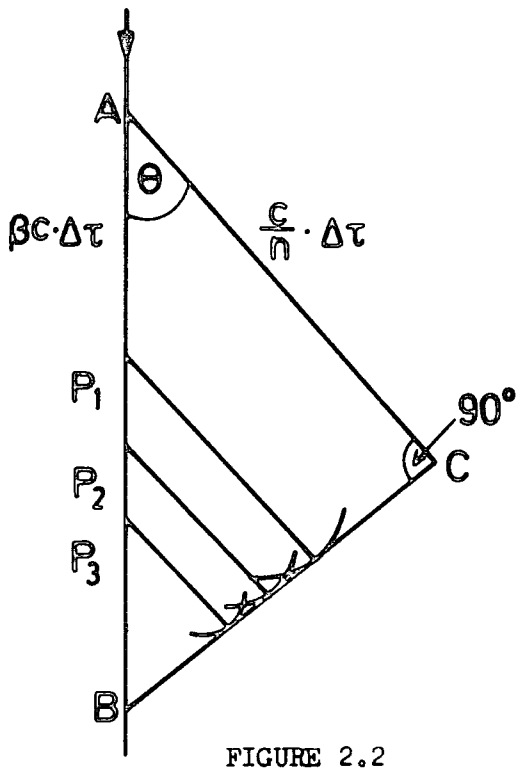

FIGURE 2.2

HUYGENS' CONSTRUCTION OF CERENKOV LIGHT WAVELETS.

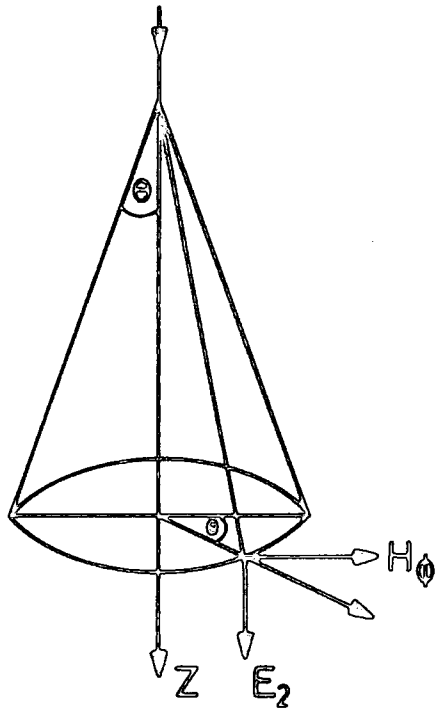

FIGURE 2.3

THE FORMATION OF THE CERENKOV LIGHT CONE, AND THE POLARIZATION VECTORS.

radiation cannot be emitted below this threshold velocity.

(2) There is a maximum angle of emission

$$\theta_{max} = \cos^{-1}\left(\frac{1}{n}\right) \qquad 2.3$$

for an ultra-relativistic particle, for which $\beta = 1$.

(3) Equation 2.1 can be satisfied for only the regions of the electromagnetic spectrum in which $n > 1$. These would be the ultra-violet, visible, infrared and microwave regions and preclude the x-ray region in which n is less than unity.

In practice, θ , is the semi-vertical angle of a solid cone of light emitted as a result of the Cerenkov effect, Figure 2.3. The light is polarized such that the electric vector $\vec{E}$ is always at right angles to the direction of propagation of the light and the magnetic vector $\vec{H}$ is tangent to the surface of the cone.

2.3 Cerenkov Radiation in Extensive Air Showers.

Research interest in Cerenkov radiation was stimulated by the suggestion by Blackett in 1948 that optical photon emission occurs when cosmic ray particles pass through the atmosphere. Blackett calculated the expected contribution of Cerenkov radiation to be only $\sim 10^{-4}$ of the total intensity due to starlight and other sources.

The requirement of a critical velocity for the emission of Cerenkov radiation (Equation 2.1) imposes a threshold energy as well. In air, the threshold energies for electrons, muons and protons are 21Mev,

4.4GeV, and 39GeV respectively. The main contribution to the light from extensive air showers is, therefore, made by electrons. These arrive simultaneously at ground level in sufficient numbers to give rise to a detectable amount of light. Jelley and Galbraith (1953, 1955) began measurements of this light component of EAS which were later confirmed by other workers including Nestorova and Chudakov (1955), Boley et al (1961) and Krieger and Bradt (1969).

2.4 Detection of Cerenkov Radiation.

Since the refractive index of air is nearly unity, Cerenkov light from an air shower particle is emitted at only a small angle to the direction of the particle (typically $\sim 1.3^{\circ}$). This directionality of the optical photon component can be used to advantage to define the arrival direction of air showers quite accurately.

The wide lateral and angular spread of the secondary electrons in the EAS gives rise to a distribution of the light over large distances from the axis of the shower. Thus a single light detector is able to detect showers whose axes fall within a large area around it.

In the last decade, some studies of optical Cerenkov radiation were carried out through measurement, at ground level, of the light originating at different heights in the atmosphere from air showers of a given energy. Such measurements have been used to determine the position of the electron cascade maximum in the longitudinal development of the showers (e.g. See Orford and Turver, 1976). By extrapolation, information on the electron cascade can lead to a knowledge of the growth of the shower, offering an insight into the mass of the primary particle.

The light profiles of atmospheric Cerenkov light have also been studied for information on extensive air showers. The initial observation by Boley (1964) of the information on the electron cascade development, obtainable through pulse shapes, was followed by measurements by Fomin and Khristiansen (1971) and Efimov et al (1973). The Durham group (See Orford and Turver (1976), Hammond et al (1978), Andam et al (1981)) has combined direct observations with theoretical predictions to study in detail the pulse shape of atmospheric Cerenkov light and relate it to the longitudinal electron cascade development of the EAS.

Protheroe (1977) has determined theoretically, the densities of optical photons, electrons and muons in extensive air showers, (Figures 2.4(a,b)). The higher density of optical photons reduces the sampling problems usually encountered when measuring electrons or muons, and gives Cerenkov light observations an advantage over the study of other components of extensive air showers at all core distances.

One major limitation in the observation of Cerenkov light is that the experiments have to be performed during clear, moonless nights and away from any location that might have intense artificial lights. Desert regions and mountain altitudes give good, clear sky conditions, and even in these locations the experiment can only be run about 10% of the time.

However, this limitation is a small price to pay for the high quality data obtainable from optical Cerenkov radiation studies.

2.5 Computer Simulations of Cerenkov Light in Extensive Air Showers.

The most useful way of checking the validity of measurements on

FIGURE 2.4(A)

THE LATERAL DISTRIBUTION AT SEA LEVEL OF PIONS (π), MUONS (μ), ELECTRONS (e), GAMMA-RAYS (γ) AND CERENKOV LIGHT PHOTONS ($\check{C}$) (Protheroe, 1977)

FIGURE 2.4(B)

THE AVERAGE NUMBERS OF PIONS (π), MUONS (μ), ELECTRONS (e), GAMMA-RAYS (γ) AND CERENKOV LIGHT PHOTONS ($\check{C}$) AS A FUNCTION OF ATMOSPHERIC DEPTH. (Protheroe, 1977)

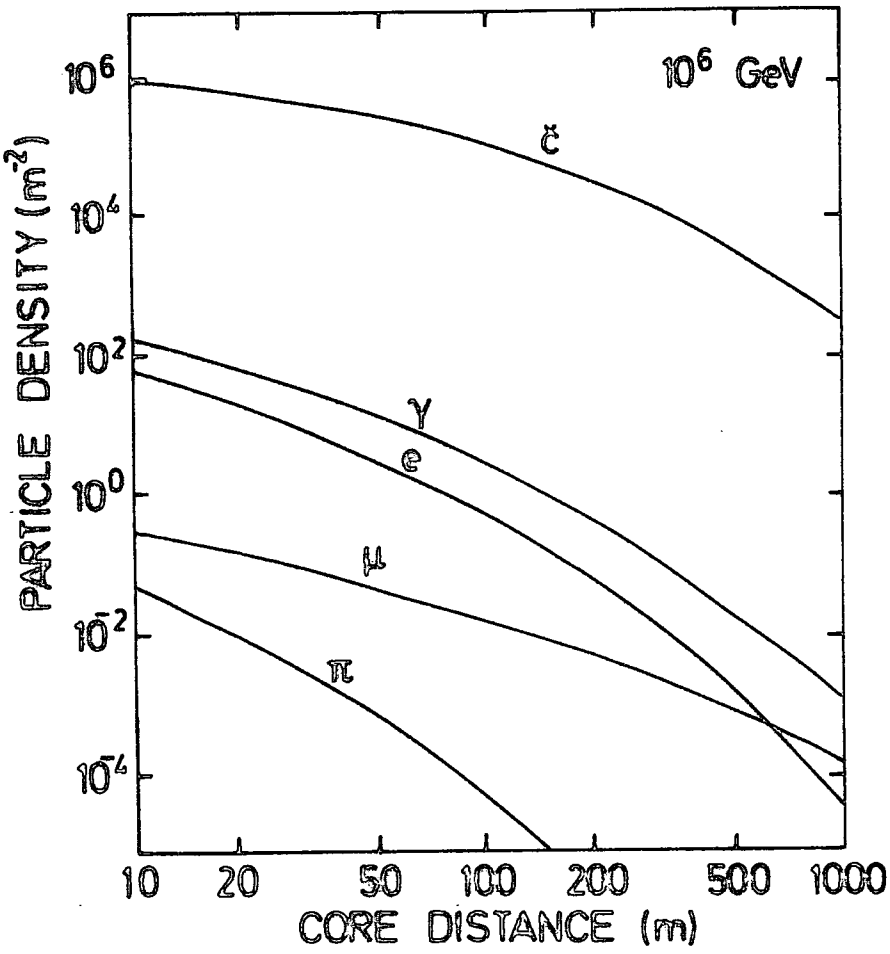
10^6 GeV
č
γ
e
μ
π
PARTICLE DENSITY (m^{-2})
10^6
10^4
10^2
10^0
10^{-2}
10^{-4}
10
20
50
100
200
500
1000
CORE DISTANCE (m)

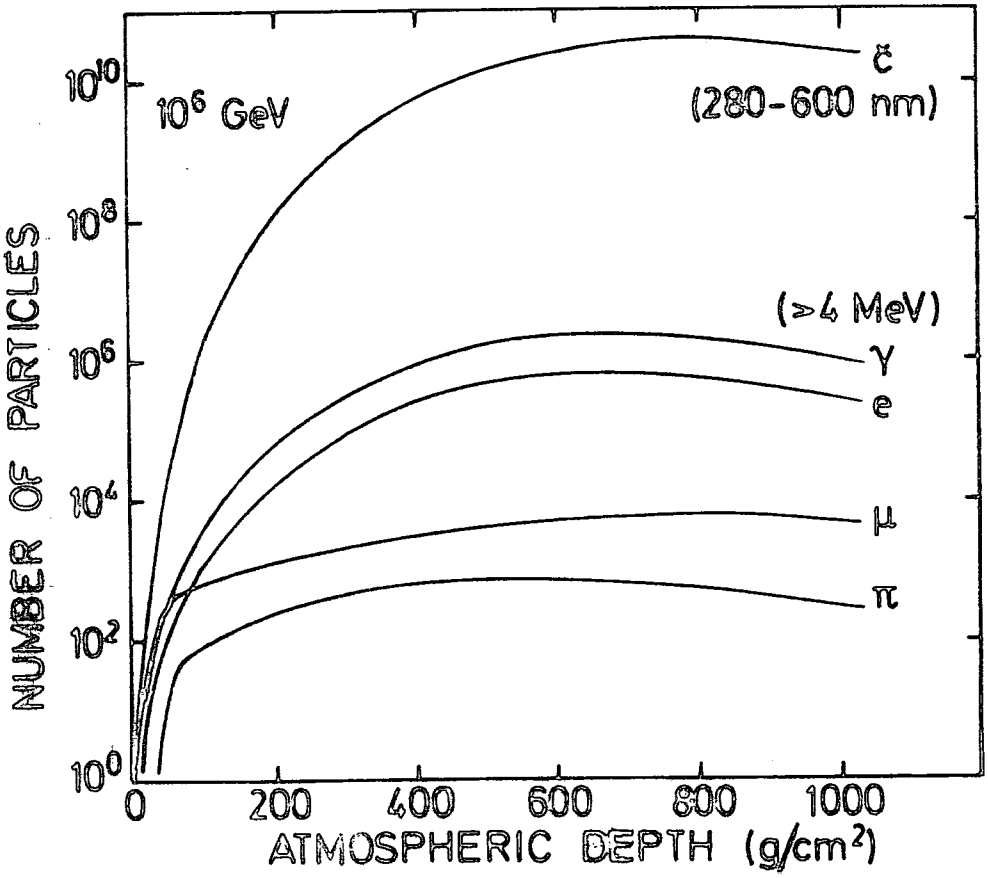
10^6 GeV
č
(280-600 nm)
(≥4 MeV)
γ
e
μ
π
NUMBER OF PARTICLES
10^{10}
10^8
10^6
10^4
10^2
10^0
0
200
400
600
800
1000
ATMOSPHERIC DEPTH (g/cm^2)

extensive air showers is to compare the observations with theoretical predictions. Computer simulations have been made by various workers including the Durham group (the most recent being those of Protheroe and Turver (1977, 1979) and McComb and Turver (1981)), using models of the propagation of cosmic rays through the atmosphere and assumptions about the primary particles. Confidence in the accuracy of the representation of high energy nuclear interactions is maintained through adequate testing of the predicted behaviour. The most recent theoretical studies at Durham have been based on Feynman's proposals of scaling (for the pion-momentum distribution), (Feynman (1969)) with constant p-N and π-N cross-sections and an iron-nucleus initiated primary.

Protheroe and Turver (1977, 1979) confined their simulations to vertical showers in the energy range 10^{17} - 10^{18} eV. The simulations were, in the main, applicable to the Haverah Park and Volcano Ranch experiments. McComb and Turver (1981) have extended this work to cover primary energies from 10^{15} eV to 10^{18} eV. Their computation uses the model atmosphere and the geomagnetic field characteristics appropriate to Dugway (i.e. appropriate to the experimental data analysed in this Thesis). The simulation data now available from the Durham group, and summarized below, cover the zenith angle range 0° - 60° and core distance range 25 - 500 metres.

2.5.1 Simulated Cerenkov Light Lateral Distribution.

The simulations of McComb and Turver (1981) show that the optical photon density does not depend on the mass of the primary or the model used for nuclear interactions. A shower may be classified only by the

depth of electron cascade maximum. In Table 2.1, four different showers, whose characteristics are described below, are listed according to their depths of maxima. Figure 2.5 shows the lateral distribution of the optical photon density for these four shower types, spanning the energy range 10^{15} eV - 10^{18} eV. There is a marked flattening of the lateral distribution, at all energies, as the zenith angle increases. This is more evident for the low energy showers, indicating that for an EAS array designed to measure such showers, problems will be encountered in locating accurate core positions for showers more inclined than $\sim 45^{\circ}$.

2.5.2 Simulated Cerenkov Light Pulse Shapes.

Information contained in the time structure of the simulated Cerenkov light pulse can be used to predict the development of the electron cascade. Results from theoretical studies (See e.g. Protheroe and Turver (1977, 1979)) have confirmed that the Cerenkov light pulse shape is sensitive to changes in shower development.

The pulse shape parameters which have been studied in most detail theoretically are :

(1) the Peak Height ;

(2) the Rise Time (the time between 10% and 90% of the peak height on the leading edge) ;

(3) the Full Width at Half Maximum - FWHM (the time between 50% on the leading edge and 50% on the back edge) ;

(4) the Top Time (the time between 90% on the leading edge and 90% on the back edge) ;

and (5) the Fall Time (the time between 90% and 50% on the back edge).

TABLE 2.1

EXTENSIVE AIR SHOWER PARAMETERS FROM COMPUTER SIMULATIONS.

(McComb and Turver, 1981)

SHOWER SERIAL	depth of maximum ($g\ cm^{-2}$)	depth of 10% ($g\ cm^{-2}$)	size at maximum (electrons)
A	495	140	2.98×10^5
B	595	205	3.04×10^6
C	695	270	3.04×10^7
D	795	320	2.99×10^8

FIGURE 2.5

THE LATERAL DISTRIBUTION OF SIMULATED SHOWERS - IRON PRIMARY

(McComb and Turver, 1981)

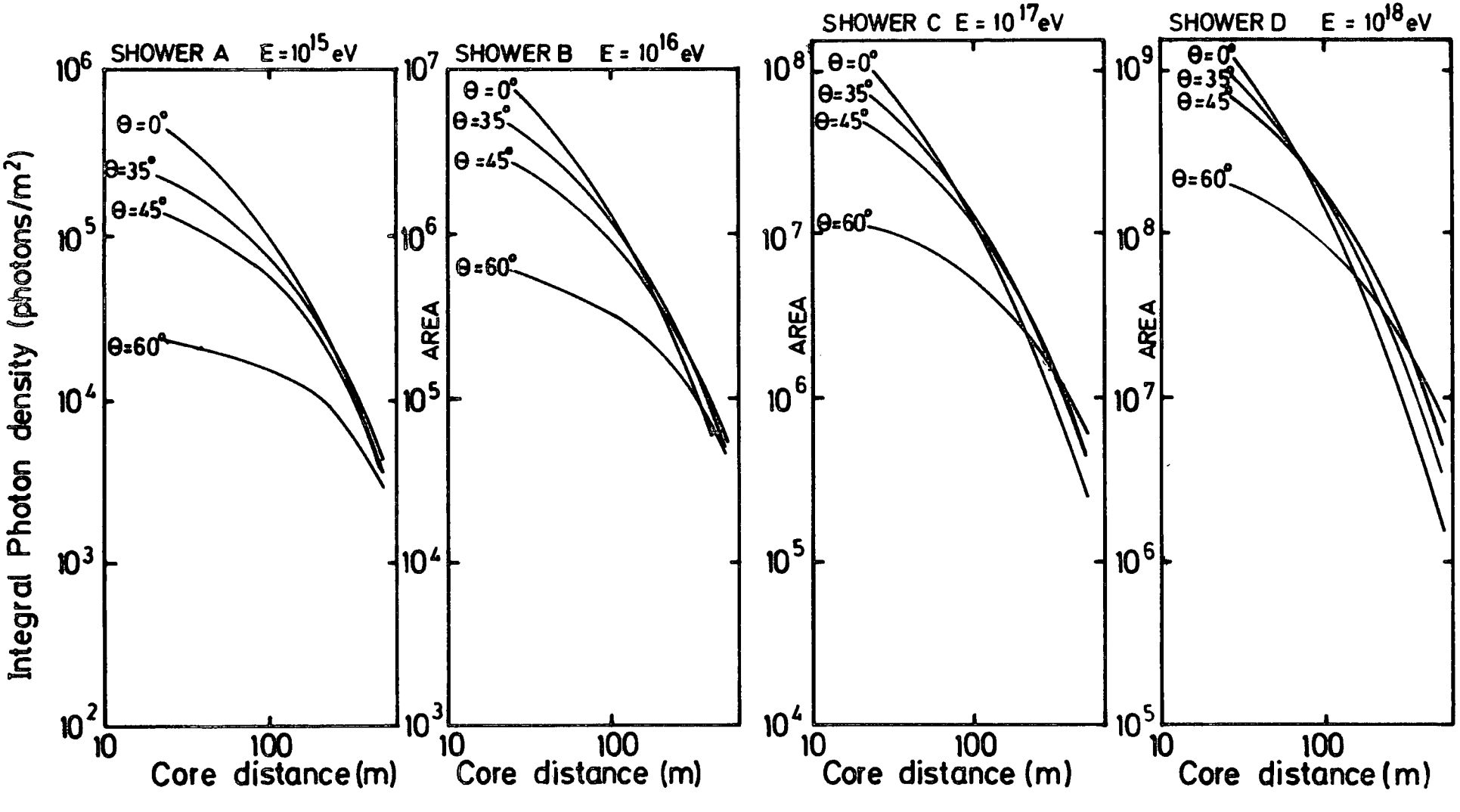
SHOWER A E = 10^15 eV
SHOWER B E = 10^16 eV
SHOWER C E = 10^17 eV
SHOWER D E = 10^18 eV
Integral Photon density (photons/m^2)
AREA
Core distance (m)
θ=0°
θ=35°
θ=45°
θ=60°

Early simulation work (e.g. Gaisser et al (1978), Protheroe and Turver (1977)) have shown that the FWHM and Rise Time vary monotonically with depth of electron cascade maximum. The Top Time and Fall Time exhibit deviations from this simple monotonic behaviour with depth of electron cascade maximum.

Figure 2.6 illustrates the Peak Height lateral distribution for the four types of showers listed in Table 2.1. The Peak Height lateral distribution, like the area lateral distribution (Figure 2.5), shows a flattening for inclined showers which is more pronounced for small showers (10^{15} - 10^{16} eV).

Figures 2.7 and 2.8 illustrate the variation of Rise Time, FWHM, Fall Time and Top Time with core distance for the same set of showers at four zenith angles. The FWHM graphs portray a definite broadening of the pulse for highly inclined showers close to the core.

The FWHM is the pulse shape parameter which has been most widely investigated both theoretically and experimentally around the World. Figures 2.9 and 2.10 show the predicted dependence of FWHM at 300m on zenith angle and depth of maximum. Computer simulations predict that the sensitivity of FWHM(300m) to changes in depth of maximum decreases with increasing zenith angle.

Close to the core, the FWHM exhibits a departure from the expected variation. There is an observed broadening of the pulse as well as an increase in sensitivity of FWHM to variations in depth of maximum for small, inclined showers.

The dependence of simulated pulse Rise Time at 300m, $t_{rise}(300m)$, on zenith angle and depth of maximum is shown in Figures 2.11 and 2.12. Figures 2.13 and 2.14 illustrate the predicted variation of the Fall

FIGURE 2.6

THE PEAK HEIGHT STRUCTURE FUNCTION OF SIMULATED SHOWERS - IRON PRIMARY.

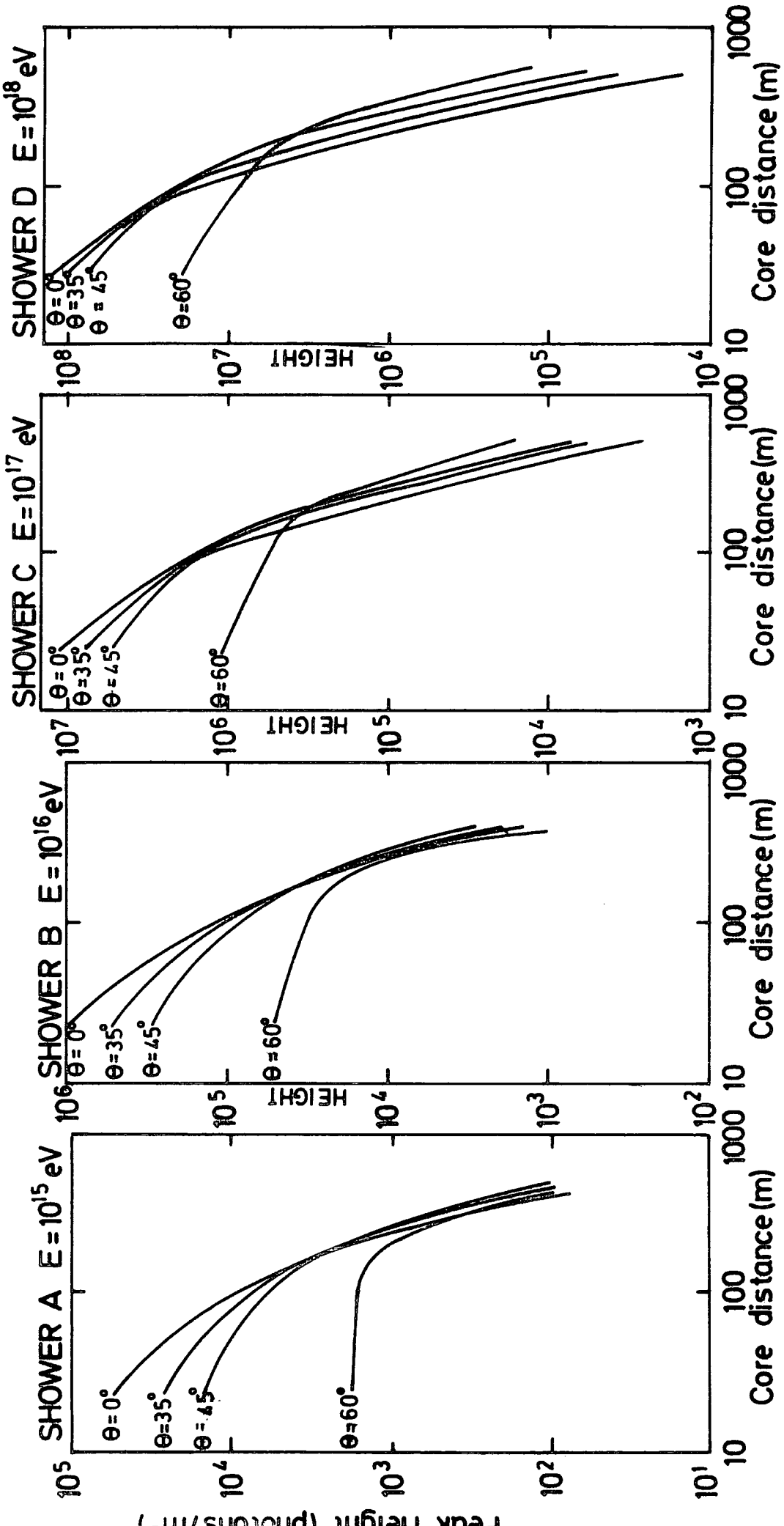
SHOWER A E=10^15 eV
SHOWER B E=10^16 eV
SHOWER C E=10^17 eV
SHOWER D E=10^18 eV
θ=0°
θ=35°
θ=45°
θ=60°
HEIGHT
Core distance (m)
Peak Height (photons/m²)

FIGURE 2.7

VARIATION OF SIMULATED PULSE SHAPE PARAMETERS

WITH CORE DISTANCE - LOW ENERGY SHOWERS.

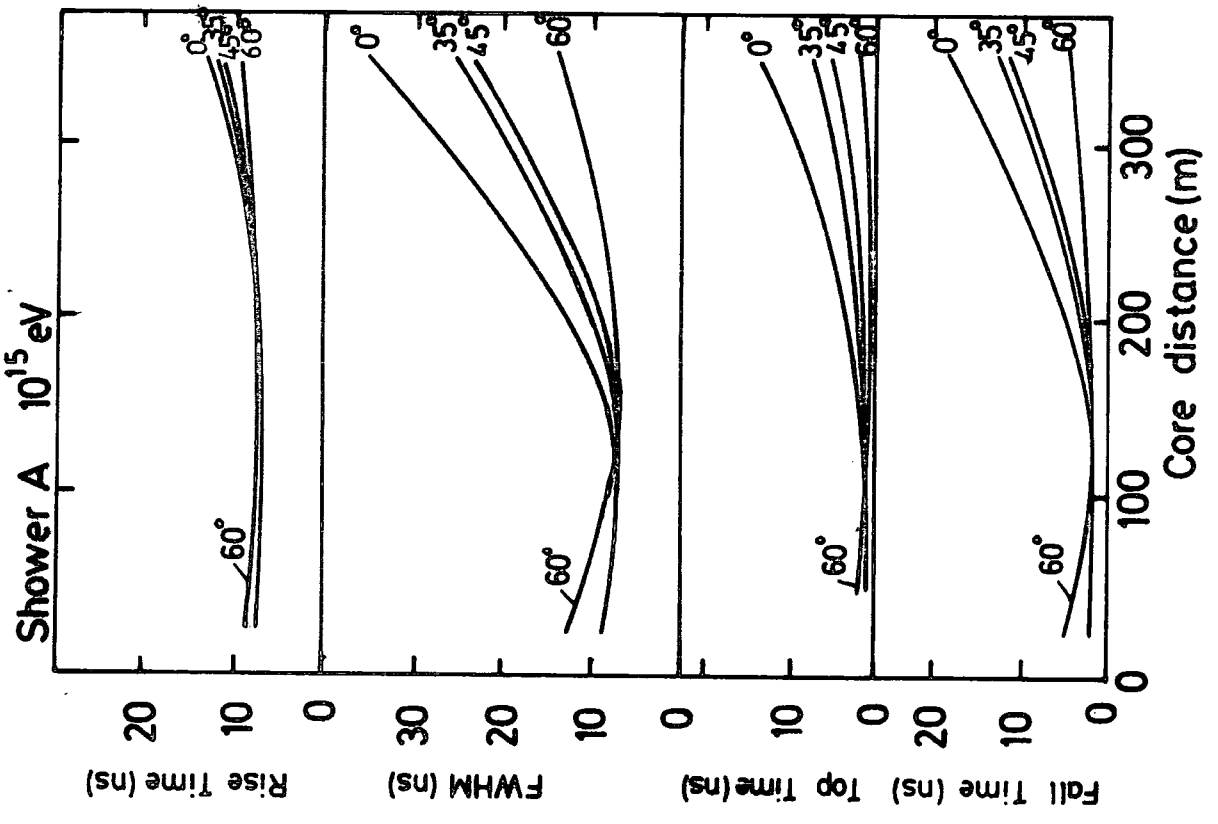
Shower A 10^15 eV
Rise Time (ns)
FWHM (ns)
Fall Time (ns) Top Time (ns)
Core distance (m)
0°
35°
45°
60°

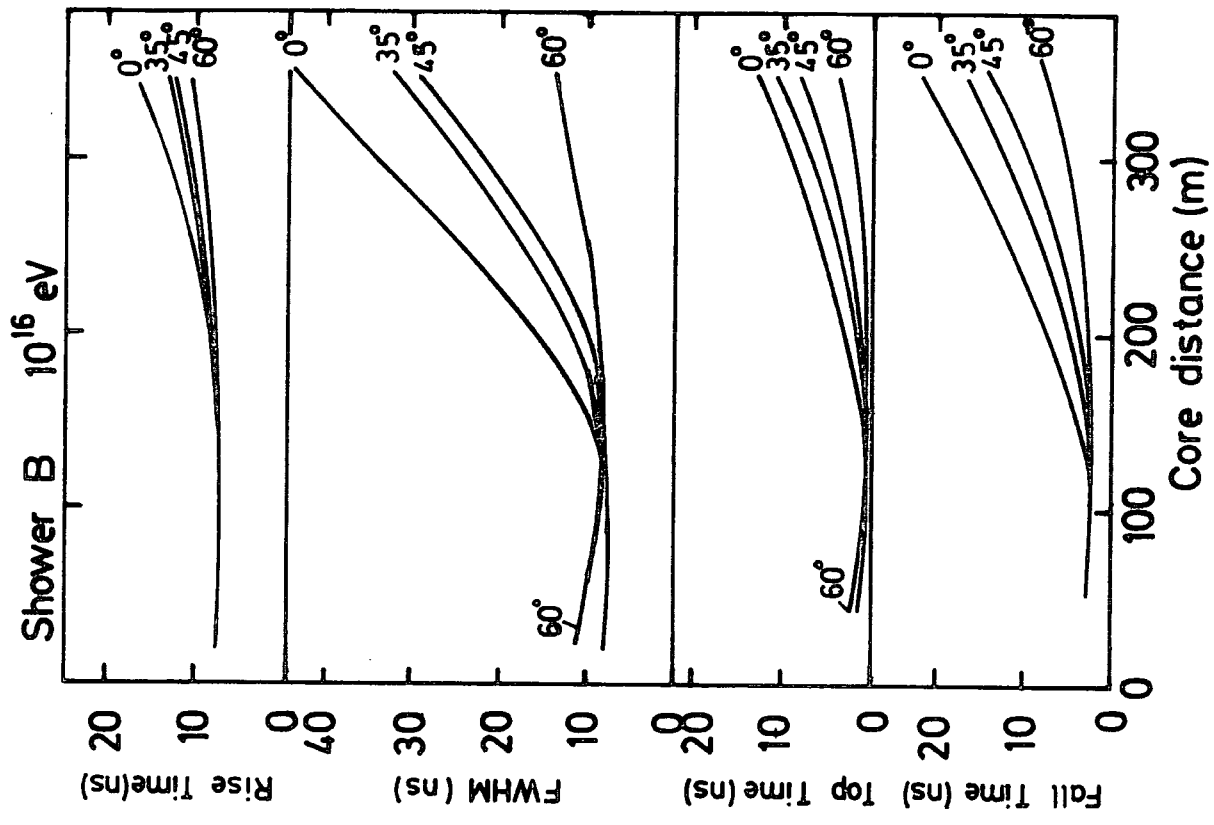
Shower B 10^16 eV
Rise Time (ns)
FWHM (ns)
Fall Time (ns) Top Time (ns)
Core distance (m)
0°
35°
45°
60°

FIGURE 2.8

VARIATION OF SIMULATED PULSE SHAPE PARAMETERS

WITH CORE DISTANCE - HIGH ENERGY SHOWERS.

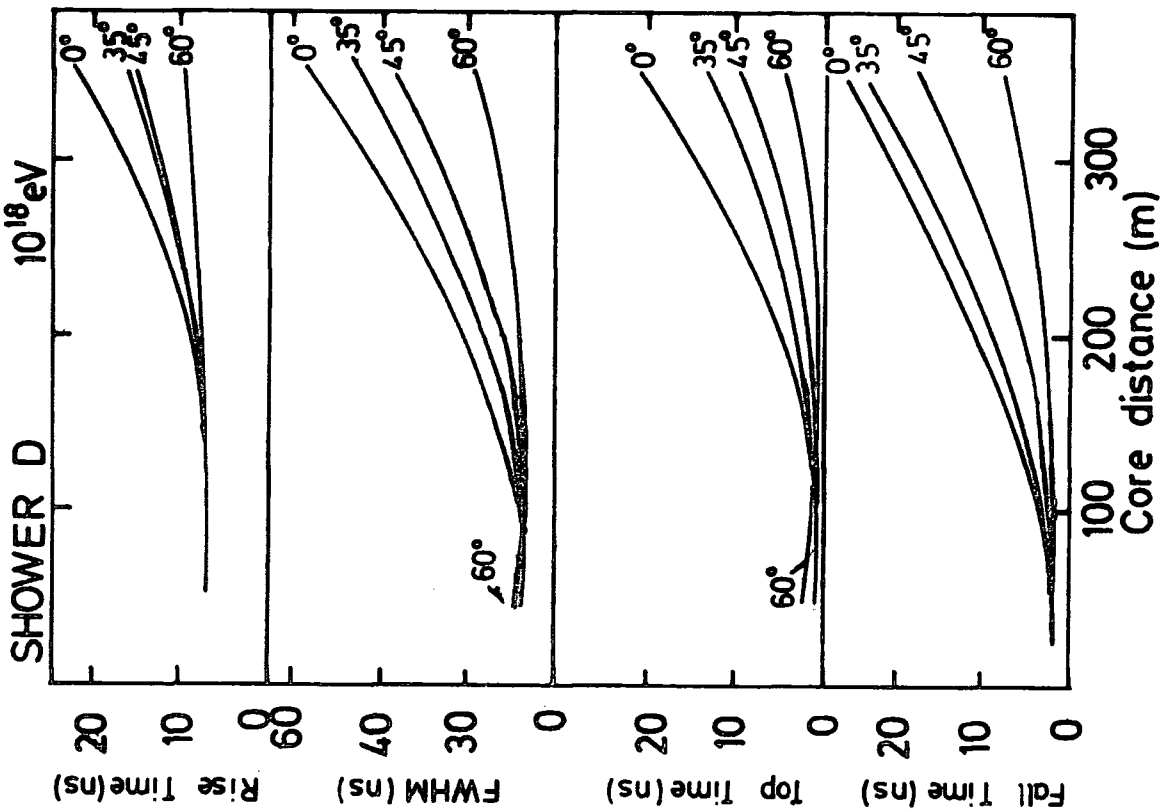
SHOWER D
10^{18}eV
0°
35°
45°
60°
Rise Time (ns)
FWHM (ns)
Top Time (ns)
Fall Time (ns)
Core distance (m)

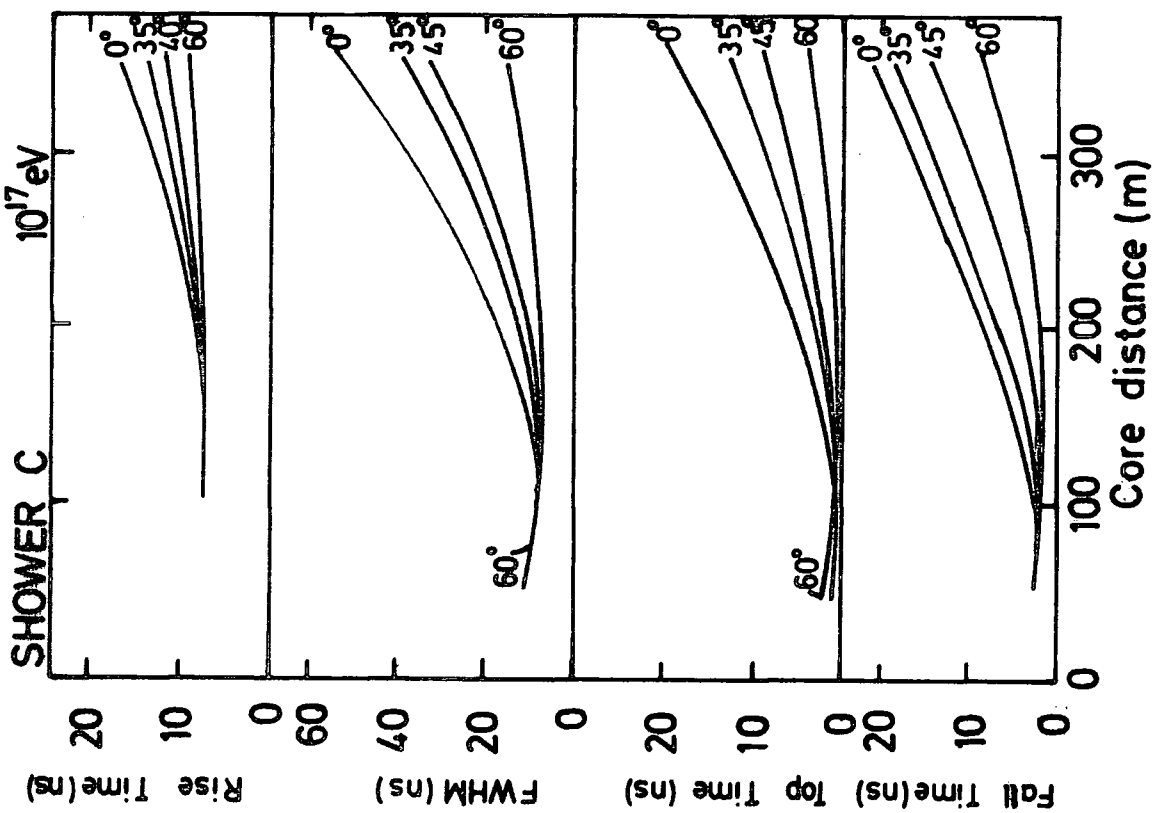
SHOWER C
10^{17}eV
0°
35°
45°
60°
Rise Time (ns)
FWHM (ns)
Top Time (ns)
Fall Time (ns)
Core distance (m)

FIGURE 2.9

VARIATION OF FWHM(300m) WITH ZENITH ANGLE FROM COMPUTER SIMULATIONS.

FIGURE 2.10

FWHM(300m) DEPENDENCE ON DEPTH OF MAXIMUM - PREDICTED FROM COMPUTER SIMULATIONS (McComb and Turver, 1981)

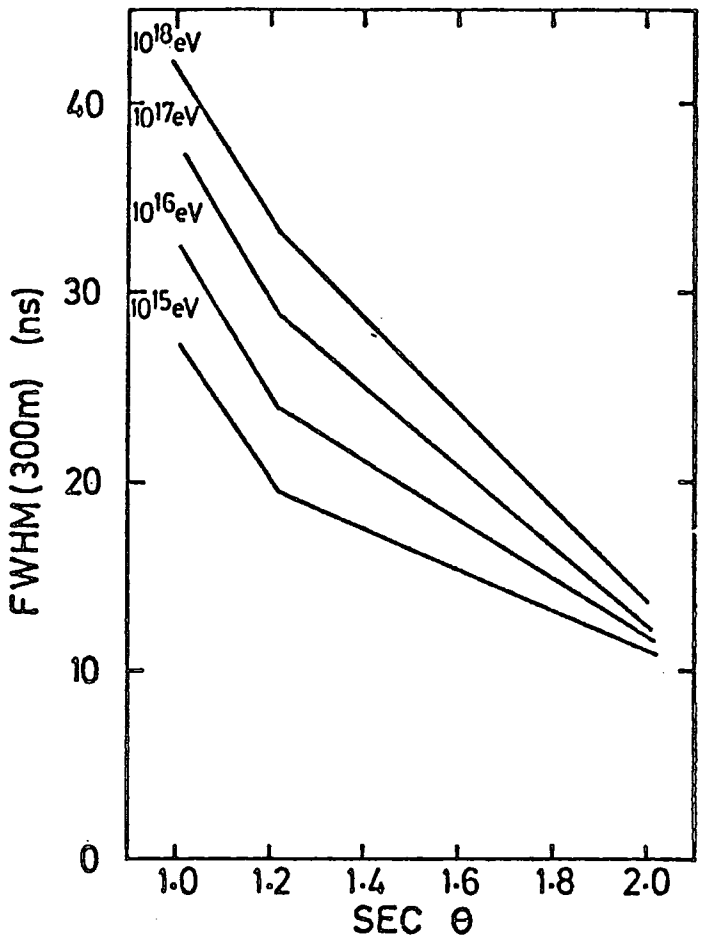
10^{18}eV
10^{17}eV
10^{16}eV
10^{15}eV
FWHM(300m) (ns)
0
10
20
30
40
1·0
1·2
1·4
1·6
1·8
2·0
SEC θ

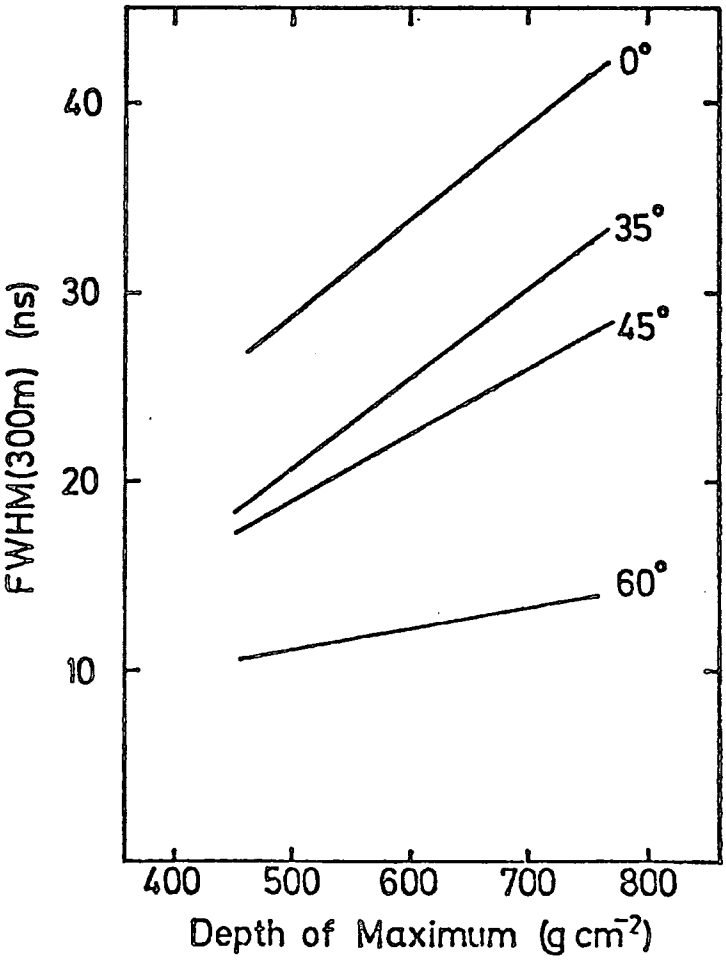
0°
35°
45°
60°
FWHM(300m) (ns)
10
20
30
40
400
500
600
700
800
Depth of Maximum (g cm^{-2})

FIGURE 2.11

PREDICTED VARIATION OF RISE TIME AT 300m WITH ZENITH ANGLE - FROM COMPUTER SIMULATIONS.

FIGURE 2.12

PREDICTED VARIATION OF RISE TIME AT 300m WITH DEPTH OF MAXIMUM - FROM COMPUTER SIMULATIONS.

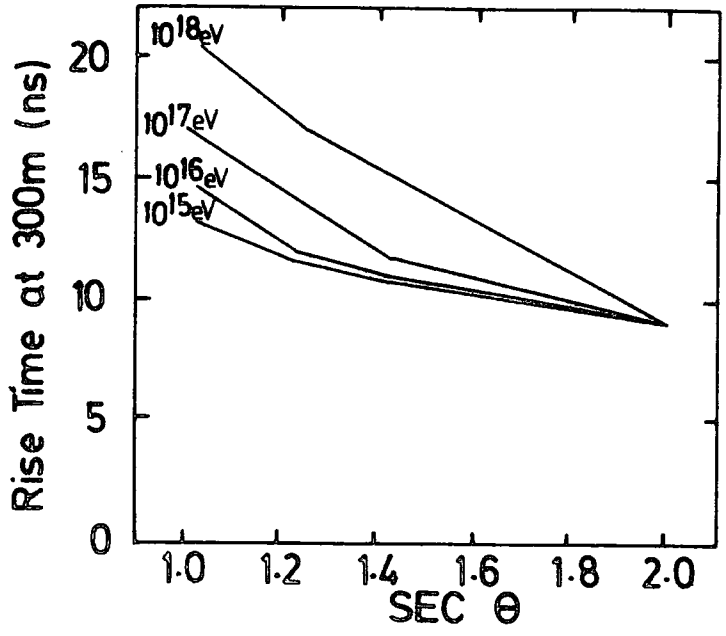
Rise Time at 300m (ns)
20
15
10
5
0
10^{18}eV
10^{17}eV
10^{16}eV
10^{15}eV
1·0
1·2
1·4
1·6
1·8
2·0
SEC θ

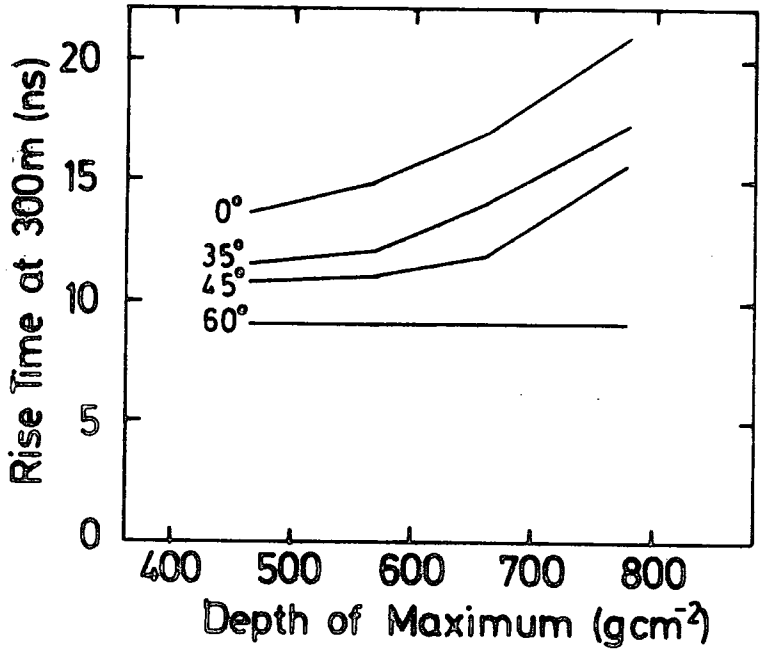
Rise Time at 300m (ns)
20
15
10
5
0
0°
35°
45°
60°
400
500
600
700
800
Depth of Maximum (gcm^{-2})

FIGURE 2.13

VARIATION OF FALL TIME AT 300m WITH ZENITH ANGLE - FROM COMPUTER SIMULATIONS.

FIGURE 2.14

PREDICTED VARIATION OF FALL TIME AT 300m WITH DEPTH OF MAXIMUM - FROM COMPUTER SIMULATIONS.

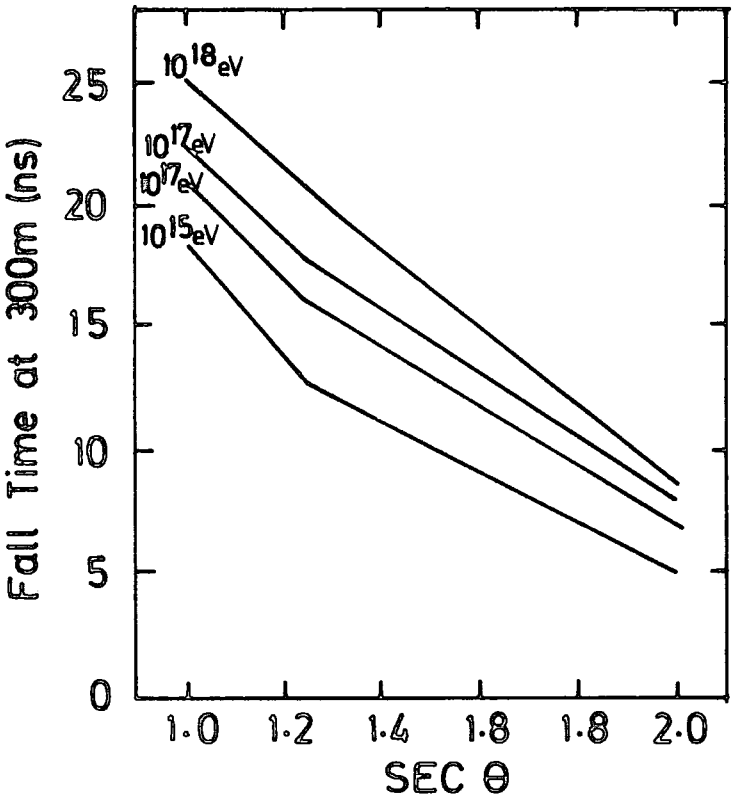
Fall Time at 300m (ns)
25
20
15
10
5
0
10^{18}eV
10^{17}eV
10^{17}eV
10^{15}eV
1·0
1·2
1·4
1·8
1·8
2·0
SEC θ

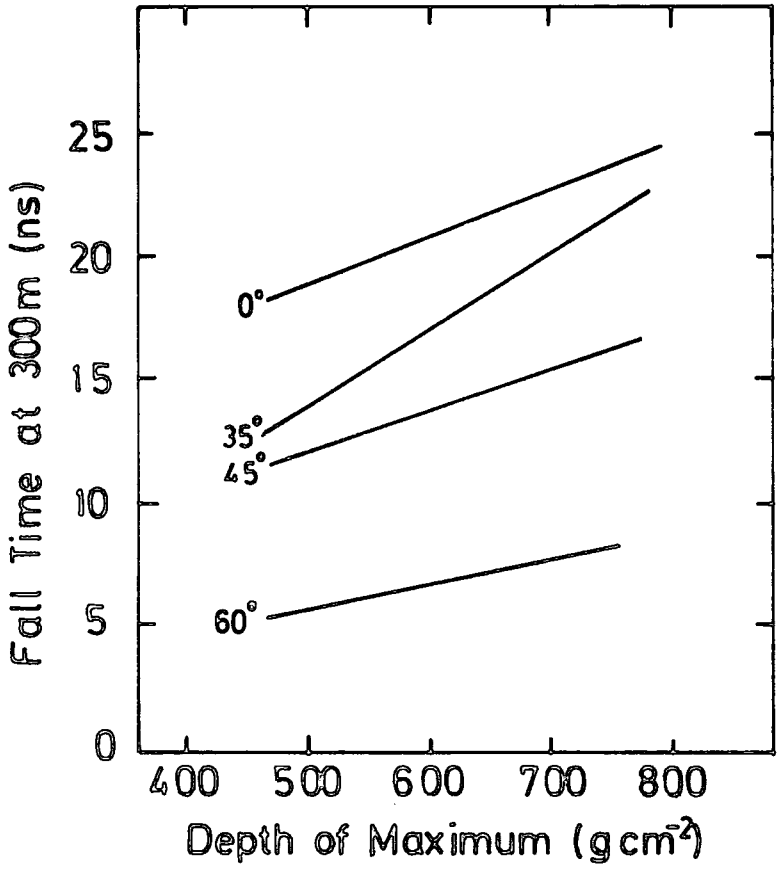
Fall Time at 300m (ns)
25
20
15
10
5
0
0°
35°
45°
60°
400
500
600
700
800
Depth of Maximum (g cm⁻²)

Time at 300m, $t_{fall}(300m)$, with zenith angle and depth of maximum. These two pulse shape parameters ($t_{rise}(300m)$ and $t_{fall}(300m)$) exhibit a complex variation with zenith angle and depth of maximum. There is a reduced sensitivity to changes in depth of maximum for highly inclined showers, but this reduction in sensitivity is more prominent for Rise Time than for Fall Time.

2.5.3 Shower Imaging.

Theoretical studies have been used by Protheroe and Turver (1977) to predict the origin in the atmosphere of the light observed at various times in the pulse. Their method involved dividing the electron cascade into sub-showers with corresponding sub-pulses of the Cerenkov light.

The results of their computer simulations, summarized in Figure 2.15 and Figure 2.16 indicate that at core distances greater than 100 metres, the earliest observed light originates high in the atmosphere. The Cerenkov light pulse, measured at ground level, maps directly the development of the electron cascade in the atmosphere. For example, if the shower front at the 10% level on the leading edge is regarded as a sphere, the centre of the sphere locates the region where the shower reaches 10% of its development.

Orford and Turver (1976) used this observation to reconstruct the development of showers through measurements of the percentage points, by treating each shower front at the percentage point as a spherical front. This technique of shower imaging is now employed routinely by the Durham Group and promises to be an important tool in the study of the electron cascade development.

FIGURE 2.15(a)

THE ELECTROMAGNETIC CASCADE DIVIDED INTO SUB-SHOWERS.

(Protheroe and Turver, 1977)

FIGURE 2.15(b)

THE LATERAL DISTRIBUTIONS OF THE SUB-SHOWERS SHOWN IN FIGURE 2.15(a) (Protheroe and Turver, 1977)

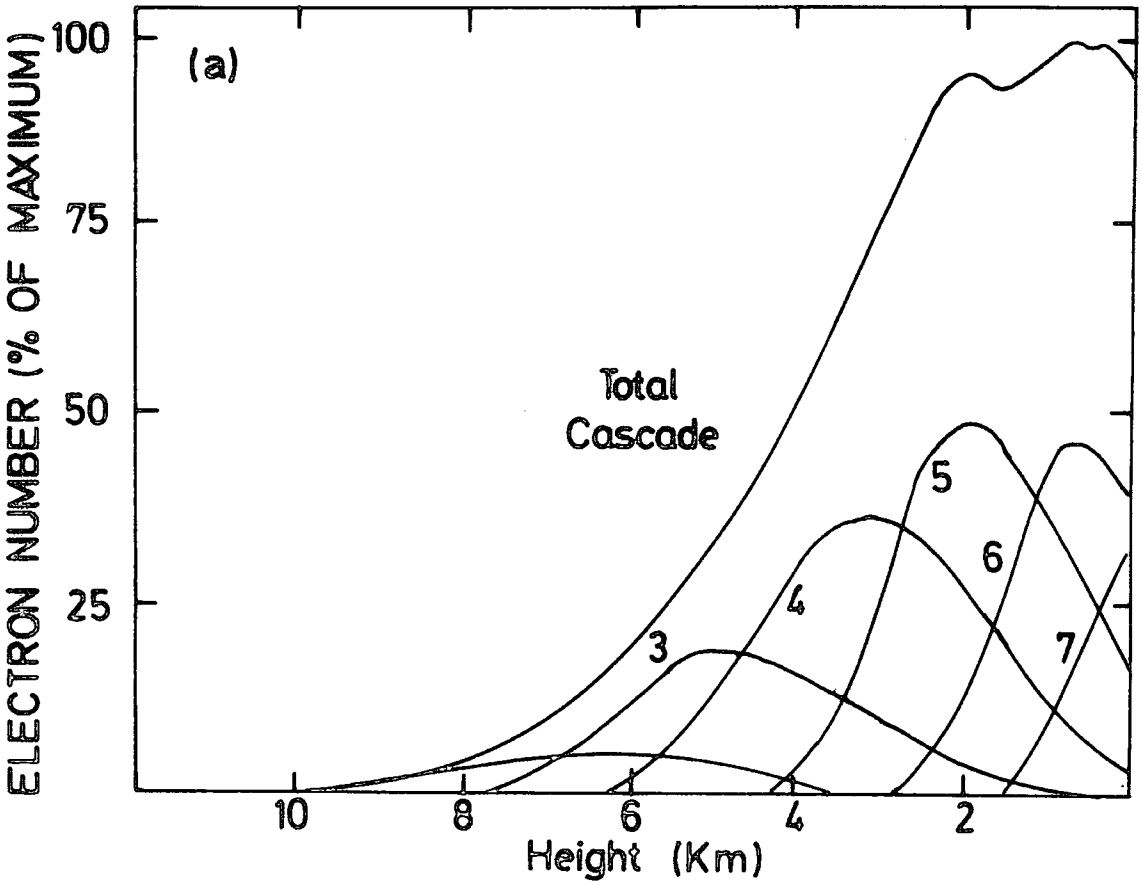
(a)
ELECTRON NUMBER (% OF MAXIMUM)
100
75
50
25
Total
Cascade
3
4
5
6
7
10
8
6
4
2
Height (Km)

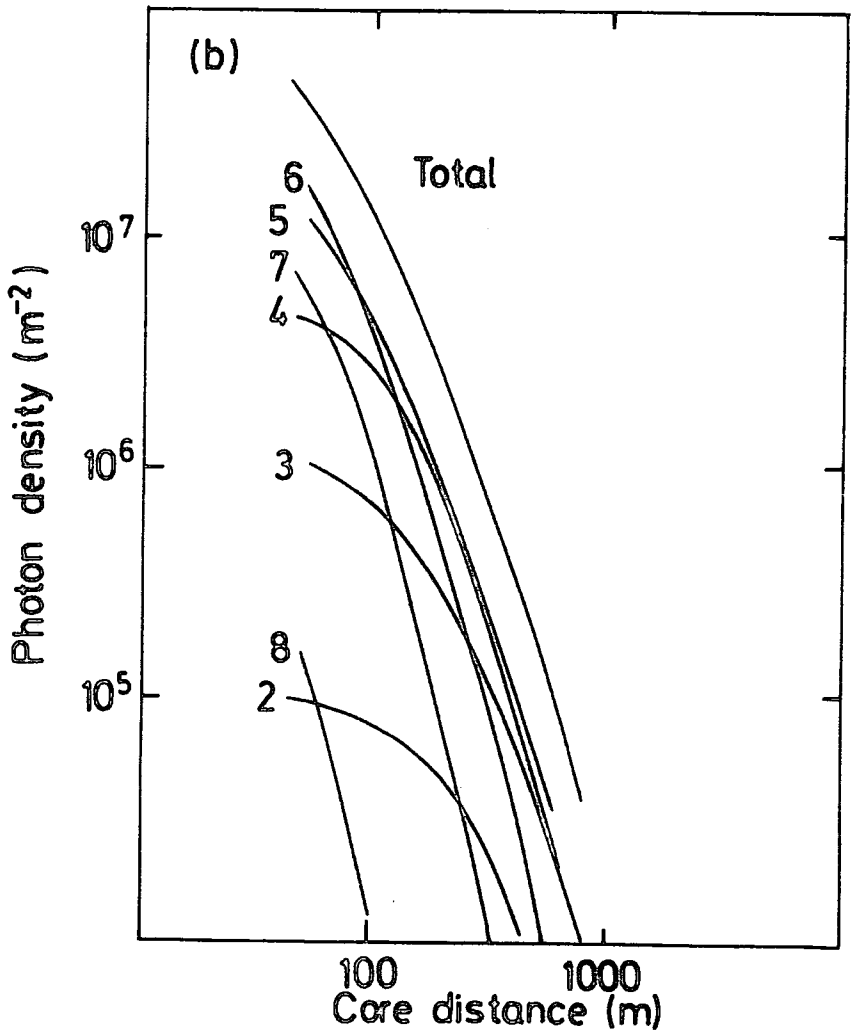
(b)
Photon density (m⁻²)
10⁷
10⁶
10⁵
Total
6
5
7
4
3
8
2
100
1000
Core distance (m)

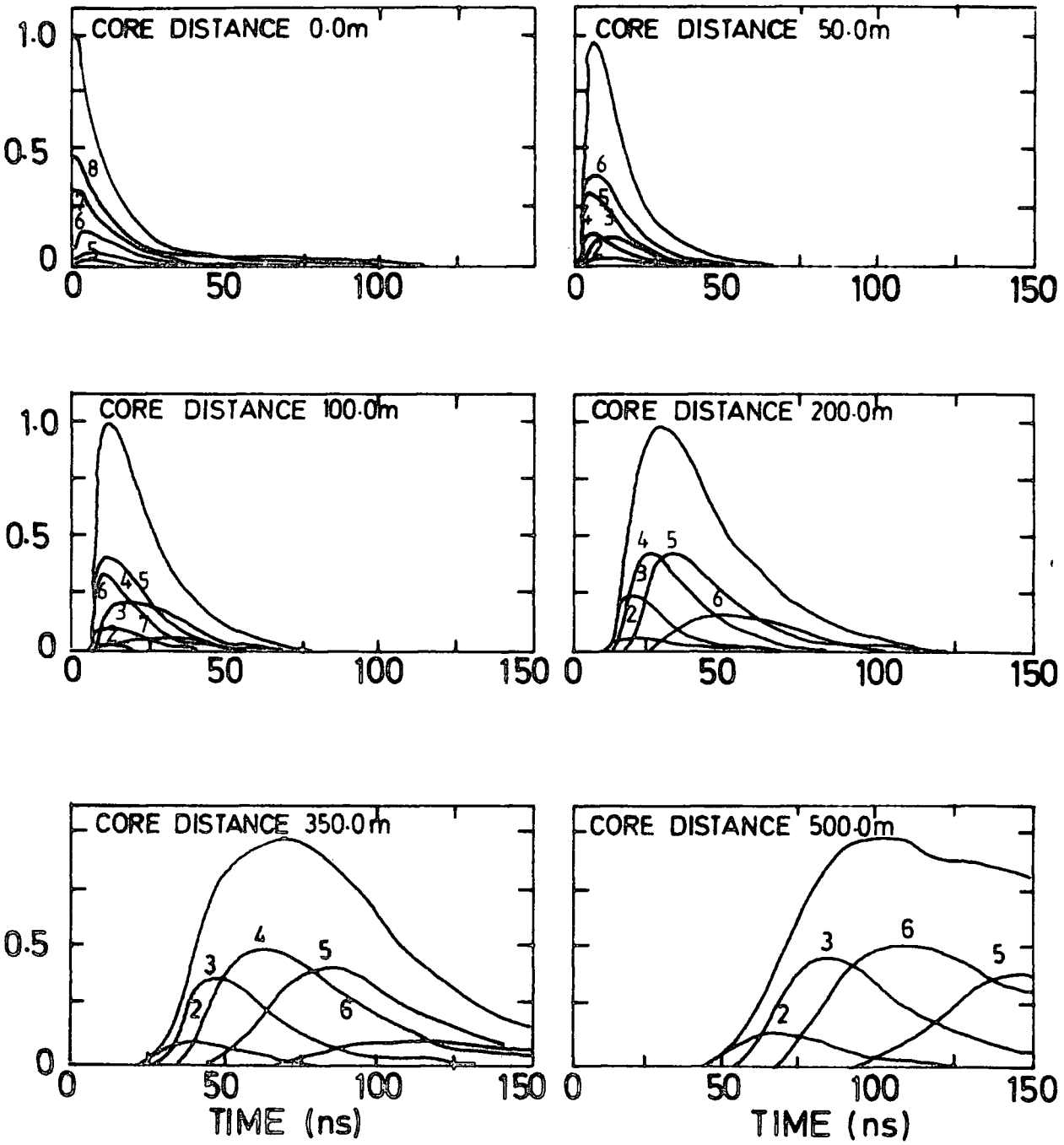

FIGURE 2.16

THE CERENKOV LIGHT SUB-PULSE PROFILES FROM THE SUB-SHOWERS SHOWN IN FIGURE 2.15(A)

(Protheroe and Turver, 1977)

CHAPTER THREE

THE DUGWAY ATMOSPHERIC CERENKOV LIGHT DETECTOR ARRAY.

3.1 Experimental Set-Up.

The construction and commissioning of the Dugway extensive air shower detector array has been described in detail by Shearer (1980). The array was located at a longitude of 112^{o} 49' W, latitude 40^{o} 12' N and an elevation of 1451 metres above sea level in the Great Salt Lake Desert, Utah, USA, at an atmospheric depth of 862 $g\ cm^{-2}$. The data analysed in this Thesis were obtained during the periods of September 1978 to March 1979 and August 1979 to March 1980. During this period the array dimension was reduced twice in order to measure extensive air showers in the energy range 10^{15} eV to 10^{18} eV.

The array characteristics were modified and updated for the Winter 1978/79 run on the basis of the results of an initial run of a similar array during the Winter of 1977/78 (Shearer, 1980). Between September 1978 and November 1979 the array was operated with the configuration shown in Figure 3.1.

Eight atmospheric Cerenkov light detectors were installed (labelled for logistic purposes as detectors 0, 1, 2, 3, 4, 5, 6, 7), with detector 1 as a central detector, detectors 2, 3, 4 (the 'outer' detectors) each at 400 metres from it and detectors 5, 6, 7 (the 'inner' detectors) at 200 metres from the centre. Detector 0 was located half-way between detector 1 and detector 2. The array

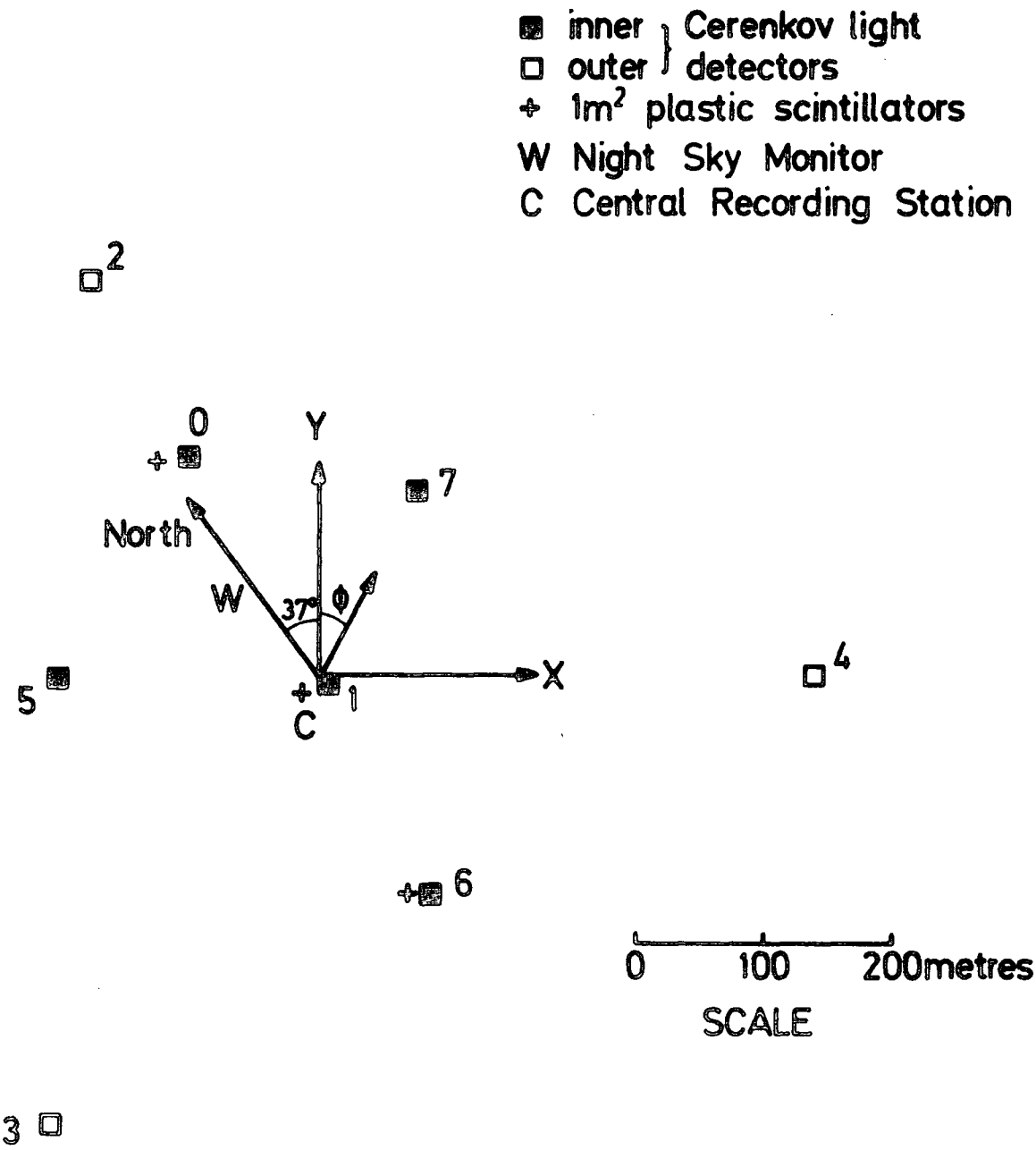

FIGURE 3.1

LAYOUT OF THE 400 metre RADIUS DUGWAY EAS ARRAY.

therefore covered a circle of 400 metre radius. This layout, according to a theoretical study by Orford (private communication), gave the largest number of 7-fold responses with core distances up to 500 metres.

To determine night sky clarity and weather conditions the following apparatus were installed :

(1) A 2-inch diameter photomultiplier viewing the night sky directly ;

(2) A 35 mm. time lapse camera to photograph the star trails at the zenith ;

(3) Temperature sensors to record the temperature 6 inches and 5 ft. above ground level, the underground temperature 6 inches below ground, and individual detector temperatures.

and (4) A pressure transducer to record atmospheric pressure.

In addition, three 1 m^2 plastic scintillators were located beside detectors 0, 1 and 6 to measure the electron density and determine the separation of the light and particle fronts.

Each detector comprised a portable aluminium casing (60 x 55 x 90 cm) which housed a fast response, 12 cm. diameter RCA type 4522 photomultiplier and its electronics system. The RCA type 4522 photomultiplier has been described by Orford et al (1977). Transmitting cables, linking the detectors to the central power point, were used to send the EAS records and DC monitoring levels from the detectors to the central recording station and synchronising pulses to the detectors from a coincidence system. The central recording station was a Tektronix 4051 computer which was used to control the shutters on the photomultipliers and to store the data to bring back to Durham for analysis.

The photomultipliers were run at anode currents approximately 1%

of their maximum rating (500 μA), (Chantler et al, 1979), and the output was taken from the 11th. dynode and amplified (x100) by 2 LeCroy VV 100 amplifiers. According to the records of Chantler et al (1979) this gave a photomultiplier/amplifier gain of 60,000 and a pulse rise time of $\sim$2.5 ns.

The array triggering criterion was the simultaneous response of all three detectors making up any of the triangles defined by detectors 2, 5, 7 ; 3, 5, 6 ; 4, 6, 7 ; and 5, 6, 7 or any three of the edge detectors in a row. The average count rate for this configuration of detectors was 15 events per hour.

In January 1980, the array dimensions were halved, whilst keeping the same basic configuration, to a 200 metre radius array. A further reduction of the array size to a 100 metre radius array was made in February 1980. These changes were made to reduce the energy threshold of the array in order to measure extensive air showers of energy $< 10^{16}$eV. The count rate was significantly increased and was $\sim$80 events per hour for the 200m. array and more than 100 events per hour for the 100m array.

3.2 Calibrations.

Shearer (1980) has given a detailed account of the calibrations made at Dugway. Six main calibrations were carried out for each Cerenkov light detector, namely :

(1) The photomultiplier gain ;

(2) The charge digitisation ;

(3) The photomultiplier transit time ;

(4) The time of arrival digitisation ;

(5) The detector synchronisation ;

and (6) The detector positions.

The detector positions had to be known accurately in order to maintain detector synchronisation to $< 1ns$ (Chantler et al, 1979). Each detector's position was carefully measured with an infrared telluorometer to an accuracy of about 1cm. (Walley, private communication). Because of the need to calibrate detector positions, and test each detector's response thoroughly after it had been moved, the changes in the array geometry from the 400m. array to the 200m. and 100m. arrays were accomplished in stages over a period of several weeks (November 1979 to January 1980). During this time, separate detectors were moved one at a time, (Walley, private communication), and each detector was checked after moving. The intermediate array geometries which resulted from these changes are shown schematically in Figure 3.2, together with the three main arrays.

The first five calibrations listed above were made at the beginning of each period of observation and repeated periodically throughout the run. It was important to ensure the stability of the photomultiplier gain and the digitisation of EAS records as well as the photomultiplier transit time. To check this stability an air shower was simulated by applying a constant current driven LED pulse to each photomultiplier and recording the resultant 'calibration event' (Shearer, 1980). This calibration was done after every 13th. recorded EAS and used to decalibrate the data before systematic analysis (See Chapter 5).

FIGURE 3.2

DIFFERENT ARRAY GEOMETRIES AT DUGWAY.

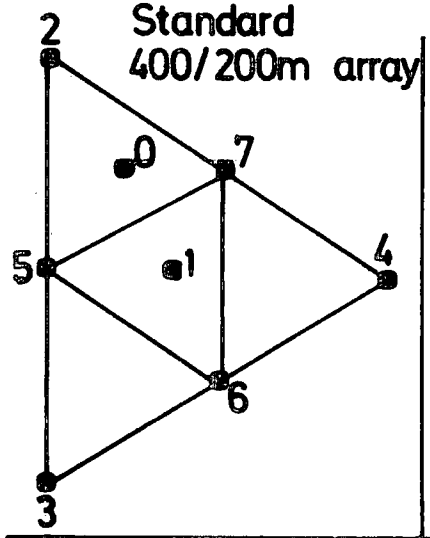
Standard
400/200m array
2
0
7
5
1
4
6
3

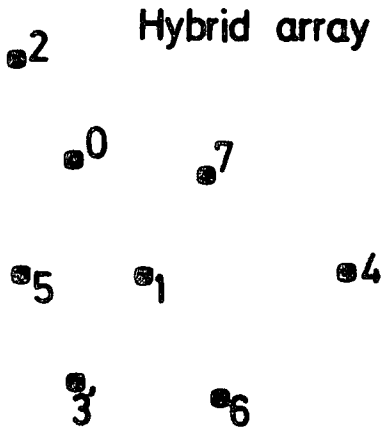
Hybrid array
2
0
7
5
1
4
3'
6

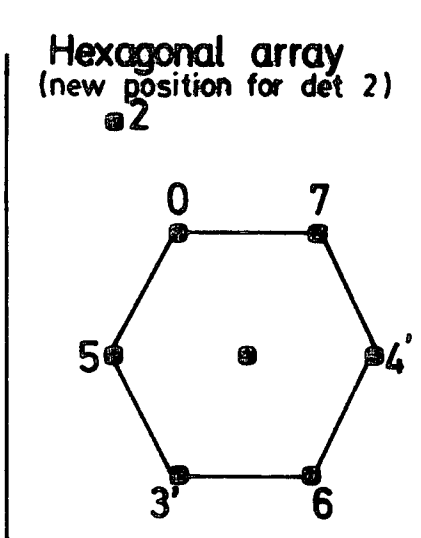
Hexagonal array
(new position for det 2)
2
0
7
5
4'
3'
6

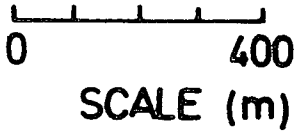
0
400
SCALE (m)

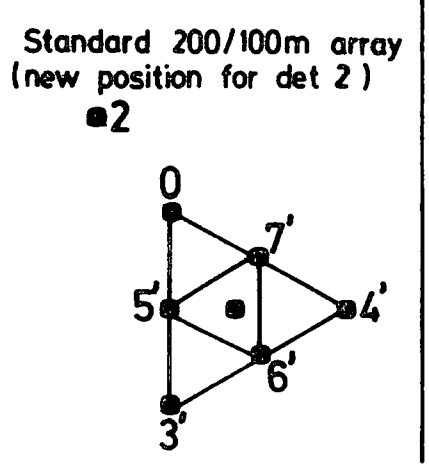
Standard 200/100m array
(new position for det 2)
2
0
7'
5'
4'
6'
3'

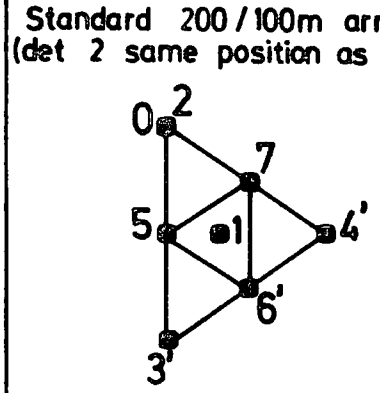
Standard 200/100m array
(det 2 same position as det 0)
0
2
7
5
1
4'
6'
3'

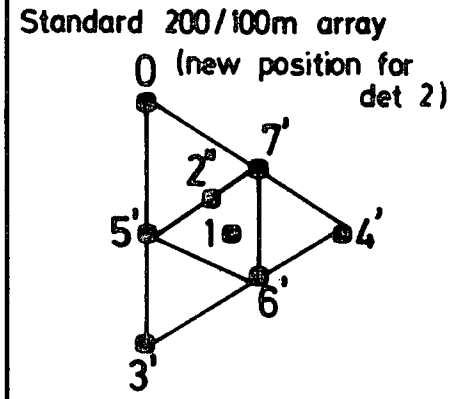
Standard 200/100m array
0
(new position for
det 2)
7'
2"
5'
1
4'
6'
3'

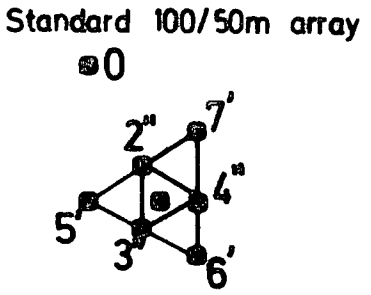
Standard 100/50m array
0
2"
7'
4"
5'
3"
6'

3.3 The Optical Cerenkov Pulse Digitisation.

The Dugway experiment was designed to record the characteristics of Cerenkov light pulses (i.e. the arrival time, photon density and a measure of the pulse shape) in digital format which could be stored on magnetic tape. The light pulse parameters were digitised at each detector by means of the electronics system illustrated in Figure 3.3 and the results transmitted to the central computer by cables.

As soon as an EAS coincidence was registered, a time stretcher with a resolution of 0.7ns (Chantler et al, 1979) was used to record the time of triggering of each detector with respect to the EAS coincidence. The total number of optical photons, measurable in terms of the total area of the pulse, was also recorded using an integrator.

To determine the pulse shape, the charge was measured sequentially through the pulse in narrow time intervals. The amount of charge in each time interval (10ns) was then stored, to be used in further analysis to reconstruct the pulse shape (See Chapter 4). This record was taken only if the amplified signal from the detector exceeded a preset discrimination threshold (nominally 20mV). If the signal exceeded this threshold, a series of gating pulses, each of 10ns width, were generated to measure the charge over a time interval which depended on the individual detector's position in the array geometry. If no coincidence was registered within 5μs after the triggering of one detector (Chantler et al, 1979), the digitisation system was reset for the next EAS record.

For the inner detectors (0, 5, 6, and 7) and the central detector 1 the pulses were short, as these detectors were often close to the shower

FIGURE 3.3

SCHEMATIC DIAGRAM OF ELECTRONICS SYSTEM FOR PULSE DIGITISATION.

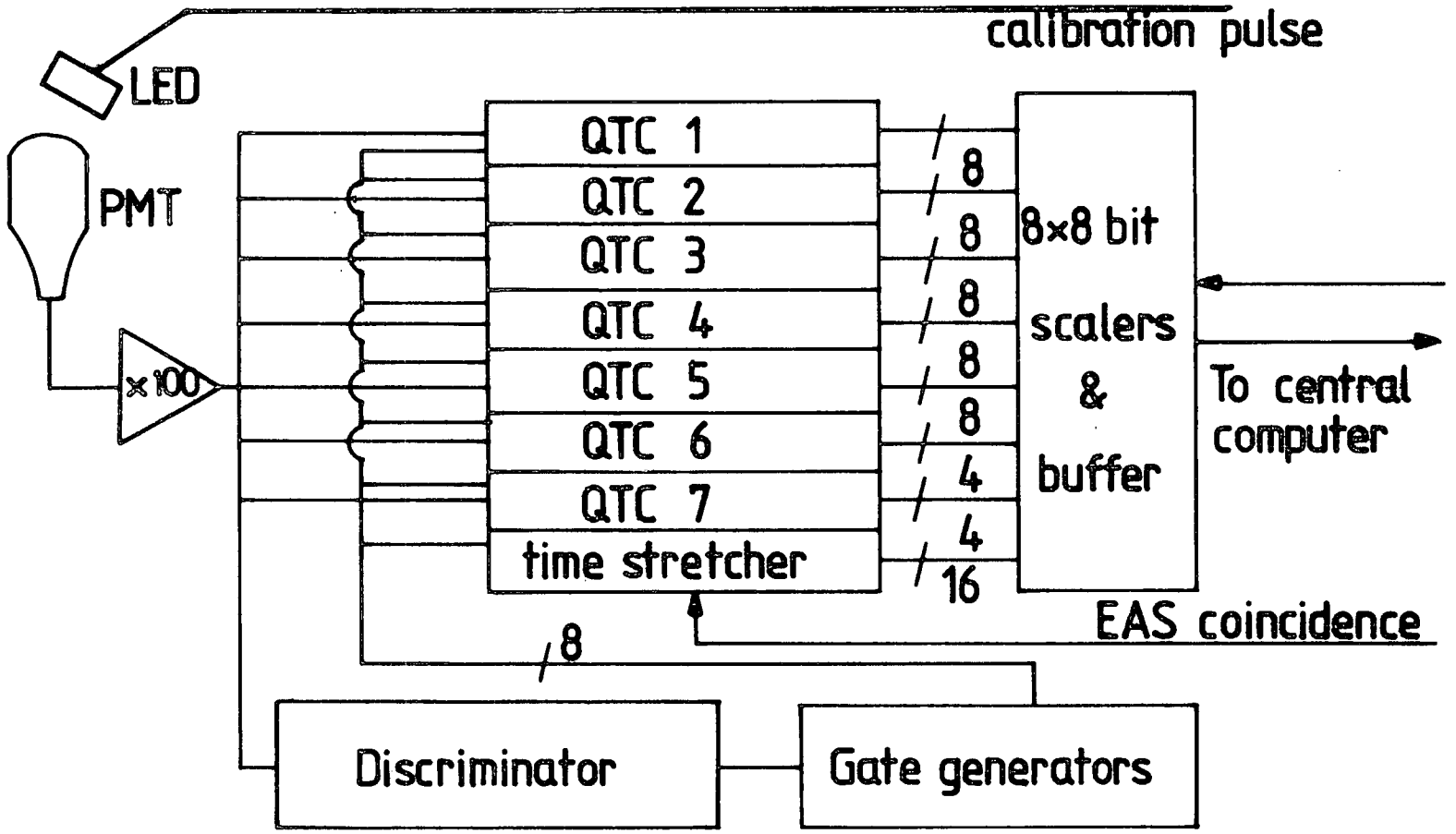

QTC: charge to time converter. Le Croy QT100B

PMT: RCA 4522 in mu-metal shield

LED: Hewlett-Packard 5082-4982 (GREEN)

axis. The pulse was therefore measured sequentially over 60 ns. For the outer detectors, sampling was started 10 ns before the discrimination threshold, and the pulse was measured over 70 ns. The slice configurations for the 400 metre array are illustrated in Figure 3.4.

Figure 3.5 shows the slice configurations for the 200m and 100m arrays. The pulses from the 200m and 100m arrays, being of lower energy primaries, were expected to be narrow. The pulses were digitised 10 ns before the discrimination level for all detectors, to account for the sharp leading edge, and only over a 50 ns time interval (i.e. all detectors now had a precursor slice and only 5 instead of 6 slices). The sum of the areas of the 5 or 6 slices was sent to the central logging computer.

After each EAS was recorded, the anode current, temperature of the photomultiplier and the temperature of the electronics system were digitised, (Shearer, 1980). During the 1978/79 run only the 2-inch photomultiplier reading and the pressure were recorded as atmospheric monitoring information. In 1979/80 the pressure, sensor box temperature and the ambient temperature 6 inches and 5 feet from ground level were all digitised as part of atmospheric monitoring records.

3.4 Environmental Monitoring.

Atmospheric conditions were carefully monitored during each night of operation. The information obtained was used to quantify weather conditions at the array site and to give an index of data quality. The suitable periods for observation, in which the moon was below the horizon for most of the night, covered the last few weeks of the Autumn and most of the Winter. The array site is in a steppe region with relatively

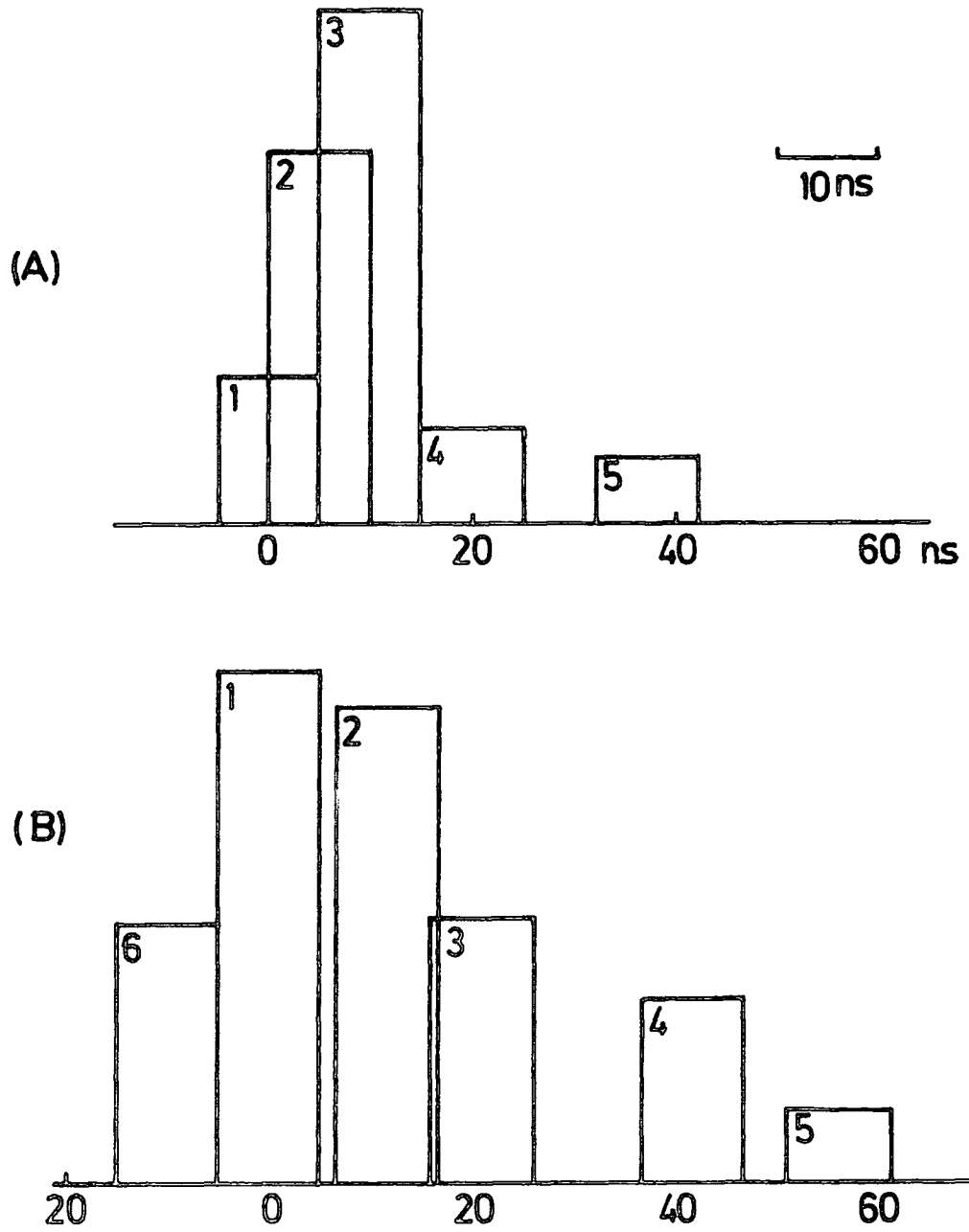

FIGURE 3.4

RELATIVE SLICE POSITIONS FOR THE 400 metre ARRAY.

(A) INNER DETECTOR (B) OUTER DETECTOR

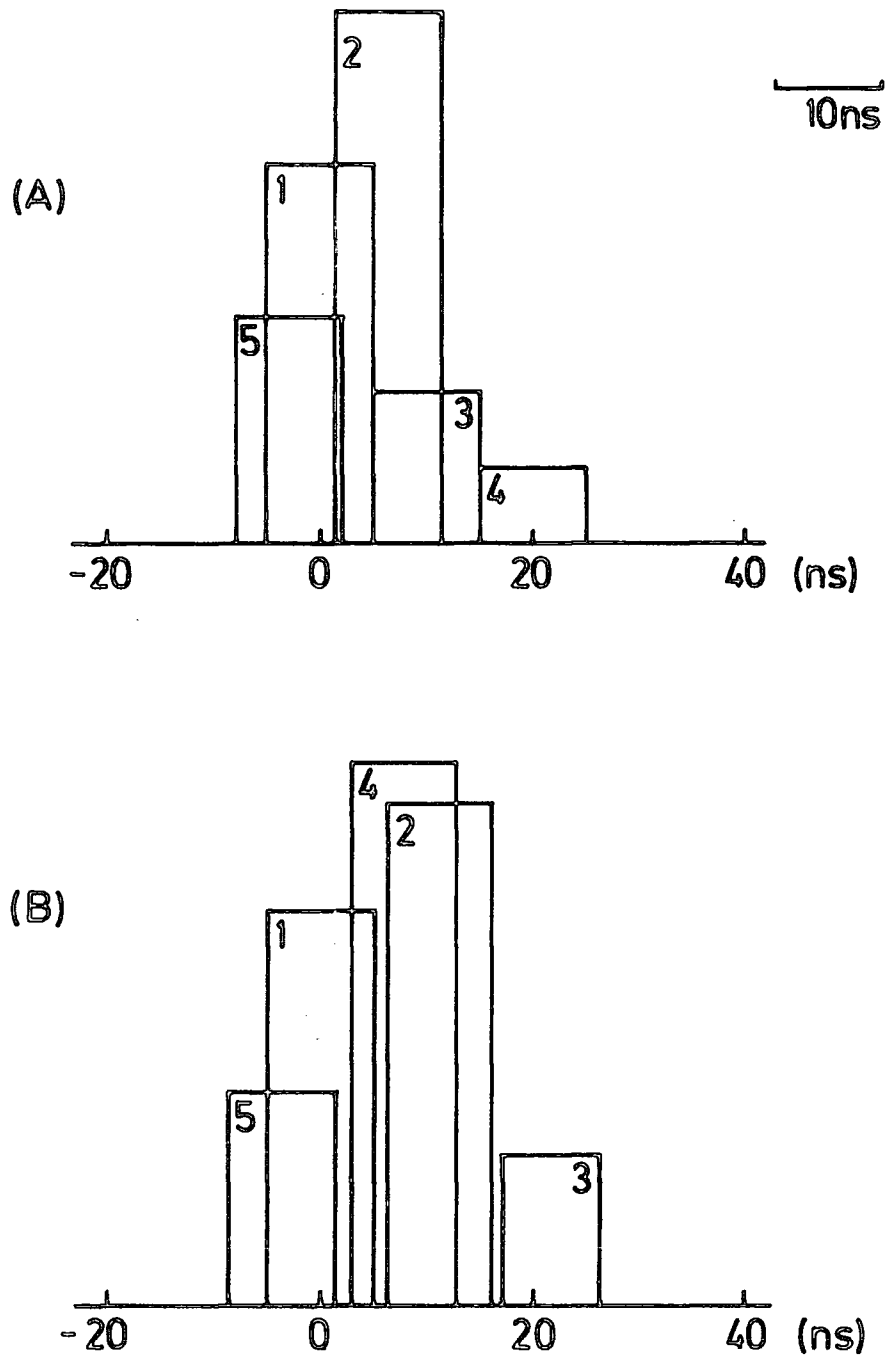

FIGURE 3.5

RELATIVE SLICE POSITIONS FOR THE 200m AND 100m ARRAYS.

(A) INNER DETECTOR (B) OUTER DETECTOR

severe seasonal temperature extremes and large diurnal ranges of temperature. The overnight temperature dropped as low as -20 ^{o}C whilst the day temperature could go up to > 40 ^{o}C in Summer.

For example, the temperatures recorded for 1978/79 are shown in Figure 3.6. January was the coldest month for Winter 1978/79 with an average of -10.4 ^{o}C and average minimum and maximum of -13.0 ^{o}C and -6.6 ^{o}C respectively. October was the hottest month for this period with an average diurnal range of 6.2 ^{o}C to 13.5 ^{o}C. To counteract the extreme temperature variations, all the detectors were thermostatically controlled to operate at a temperature of 20 ^{o}C.

The average minimum pressure recorded for Winter 1978/79 was 849 mb. in December. The average maximum pressure recorded during this same period was 856 mb. in November 1978. Figure 3.7 shows the variation for the average pressure and the average maximum and minimum pressures for Winter 1978/79. The curves all show a drop in the pressure from November to December and a sharp rise from December to January.

As expected in this region, the weather during the Winter months exhibited a fair amount of variation of cloudiness. The cloud cover was carefully monitored throughout each night. Only data from nights when the sky was consistently clear of clouds (quantitatively monitored through star trail pictures) were used in the analysis.

3.5 Sky Films as a Measure of Sky Brightness for Data Quality Control.

The greatest importance was attached to establishment of the relative clarity of the sky at the time of each EAS record. To estimate sky clarity, two quantities were measured, viz :

(1) The brightness of the night sky recorded by a 2-inch diameter

FIGURE 3.6

DUGWAY - WINTER 1978/79, TEMPERATURE VARIATION PER MONTH.

FIGURE 3.7

DUGWAY - WINTER 1978/79, PRESSURE VARIATION PER MONTH.

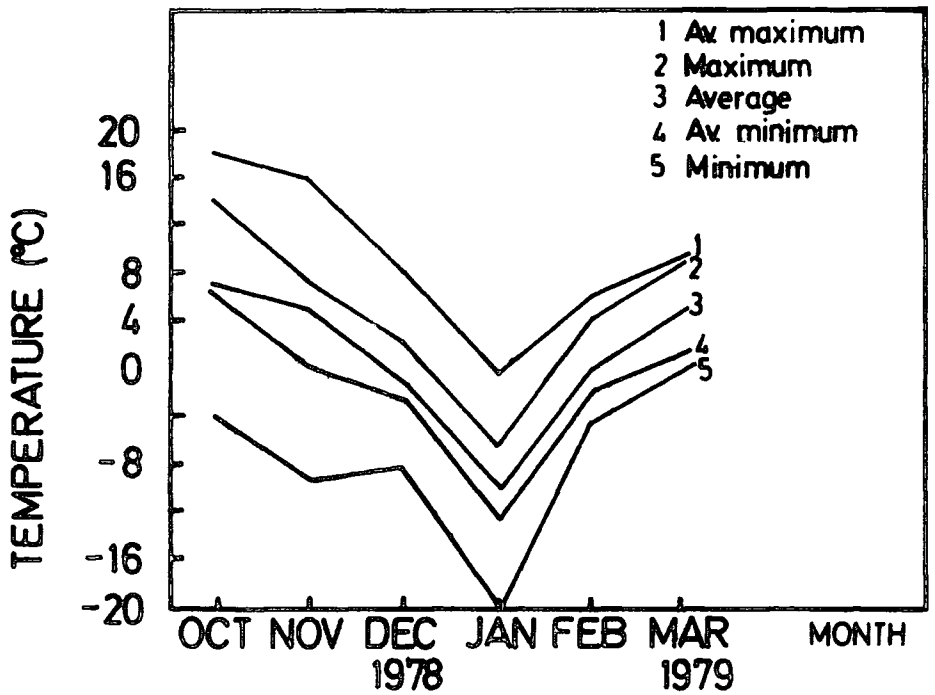
1 Av. maximum
2 Maximum
3 Average
4 Av. minimum
5 Minimum
TEMPERATURE (°C)
20
16
8
4
0
-8
-16
-20
OCT NOV DEC JAN FEB MAR
1978
1979
MONTH

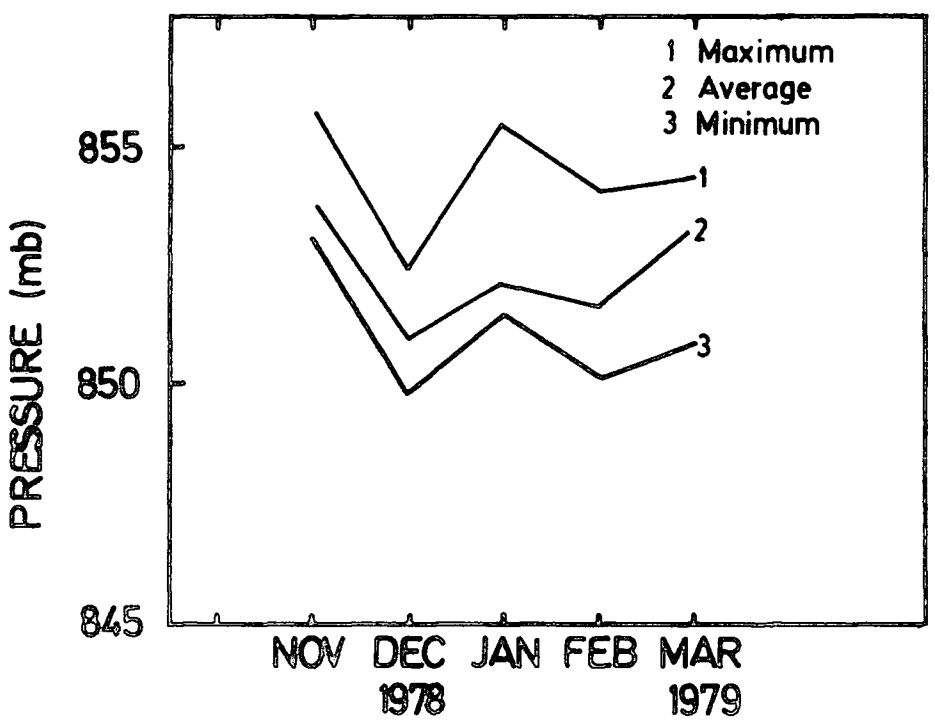
1 Maximum
2 Average
3 Minimum
PRESSURE (mb)
855
850
845
NOV DEC JAN FEB MAR
1978
1979

photomultiplier after each event.

and (2) the sky clarity monitored from the star trails on 35 mm time lapse camera records.

Figure 3.8 shows typical 2-inch PMT profiles. These illustrate, broadly, the variation of the array's performance as the sky clouds over and brightens up again during any one night.

During the Winter of 1978/79 the star trail pictures were taken with one camera pointing vertically. Two additional cameras were used during the Winter of 1979/80, giving three cameras pointing North, South and in the vertical direction.

The maximum detectable stellar magnitude (i.e. the magnitude of the faintest star) was estimated after locating the stars in view during the period. For example, at approximately 0645 GMT (or 2345 Mountain Standard Time) on 24 September 1979, some of the stars in view at the site are shown in Figure 3.9. In determining the stellar magnitudes the convention in the Smithsonian Astrophysical Observatory Star Atlas was followed, a low order of magnitude indicating a bright star and vice versa. The highest order of magnitude in the SAO Star Atlas is 9; our prints of star trails gave a highest order of magnitude of 8 on prime weather nights.

The time for each print was found from the start of the film on the calculated time interval of 14.5 minutes between adjacent frames. To obtain a measure of the sky conditions, all the prints for the night were scanned. For example, on the night of 24 September 1979 the prints show that at 0750 GMT, the sky clouded over for approximately 30 minutes and then brightened up again. The prints for this time of the night are shown in Figures 3.10(a-d). Figure 3.10(d) shows how the clouds have chopped up the star trails when the sky begins to brighten up again. A

FIGURE 3.8

2 INCH PMT PROFILES FOR (A) CLEAR NIGHT
(B) BAD WEATHER NIGHT

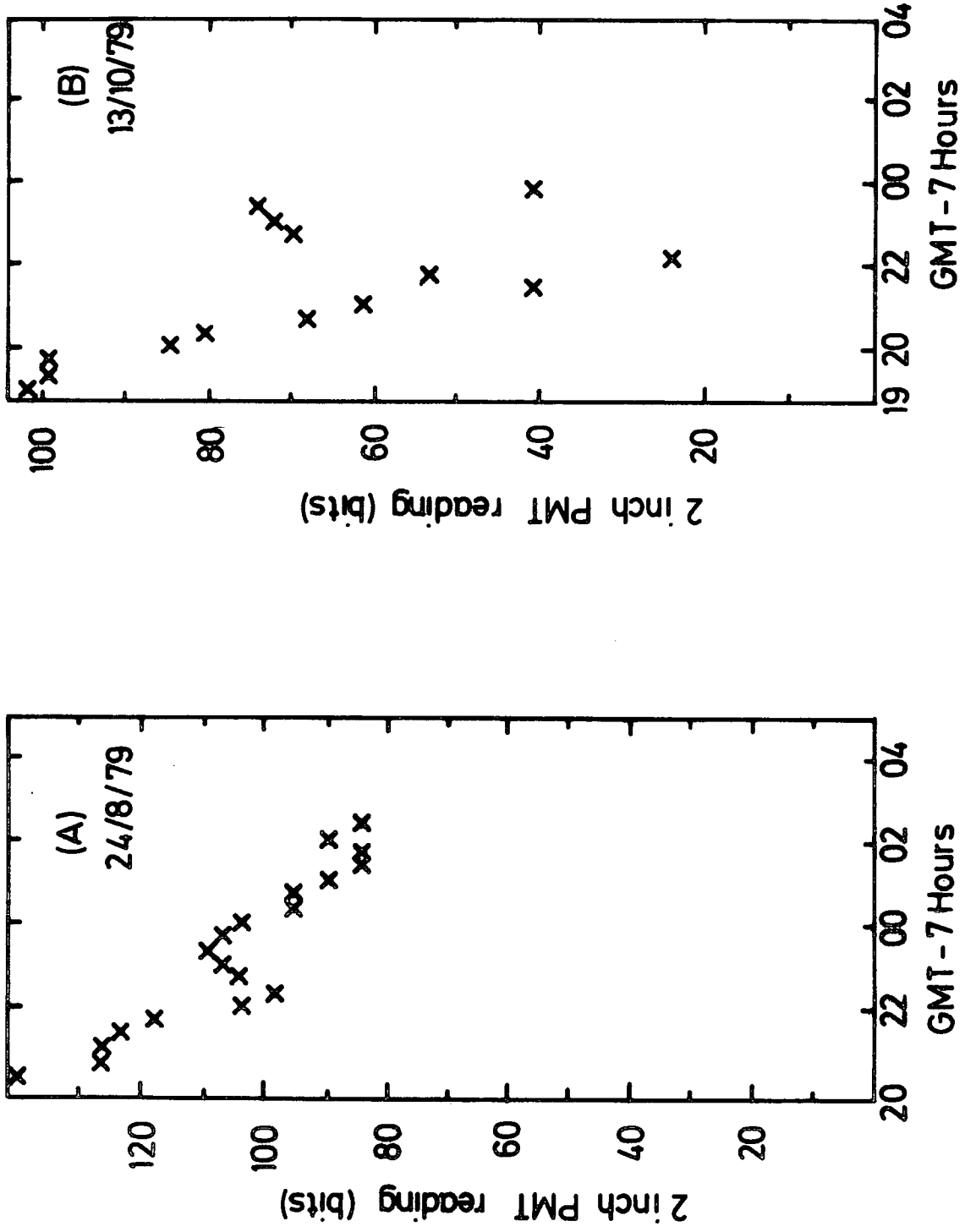
(A)
24/8/79
2 inch PMT reading (bits)
120
100
80
60
40
20
20
22
00
02
04
GMT-7 Hours
(B)
13/10/79
2 inch PMT reading (bits)
100
80
60
40
20
19
20
22
00
02
04
GMT-7 Hours

FIGURE 3.9

STAR TRAILS FROM NORTH-LOOKING CAMERA FOR THE NIGHT OF 24 SEPTEMBER 1979, TIME $\simeq$ 0645 GMT.

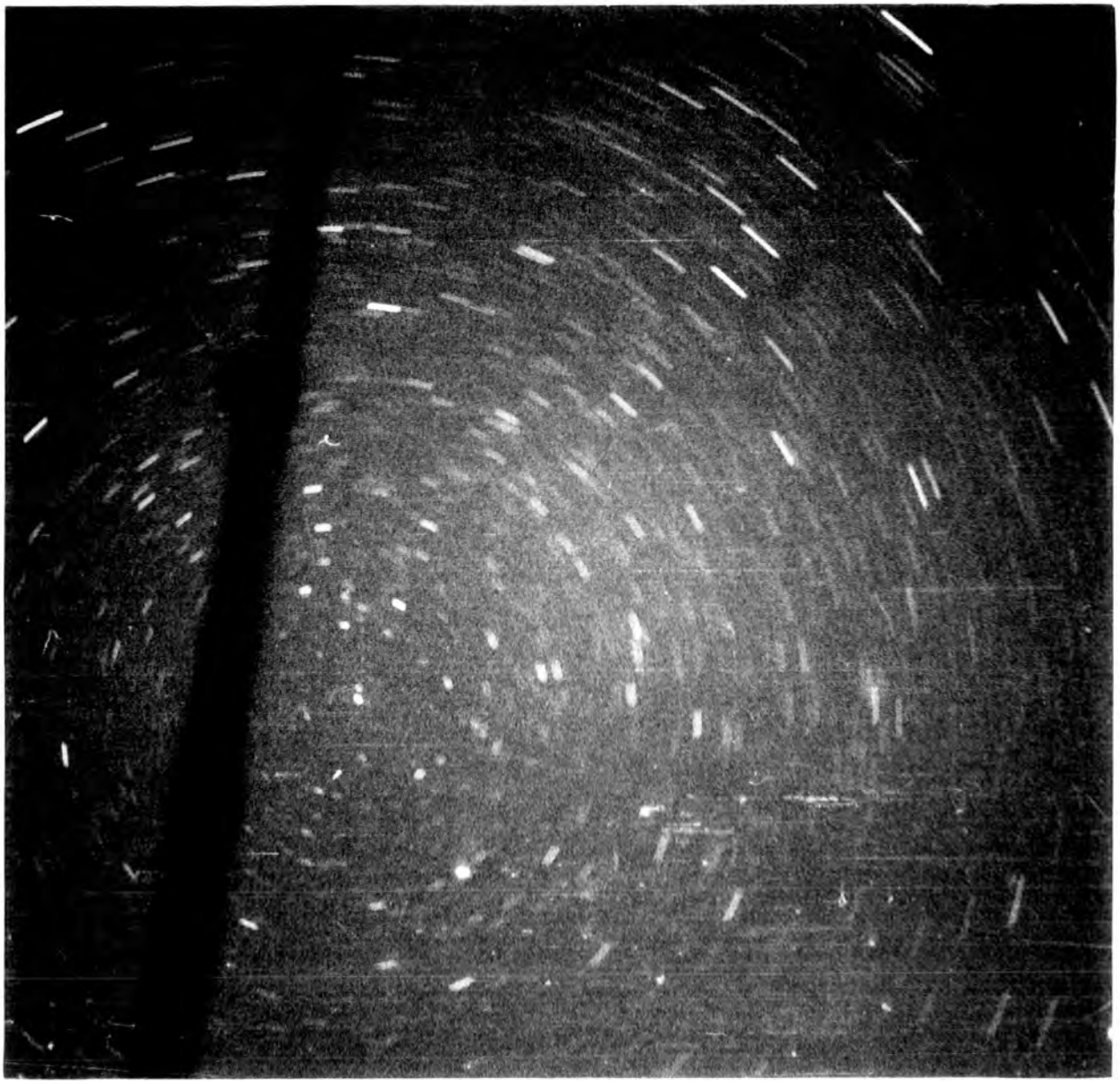

FIGURE 3.10

STAR TRAILS FROM NORTH-LOOKING CAMERA FOR THE NIGHT OF 24 SEPTEMBER 1979 (BAD WEATHER NIGHT) SHOWING CHANGES IN SKY CLARITY.

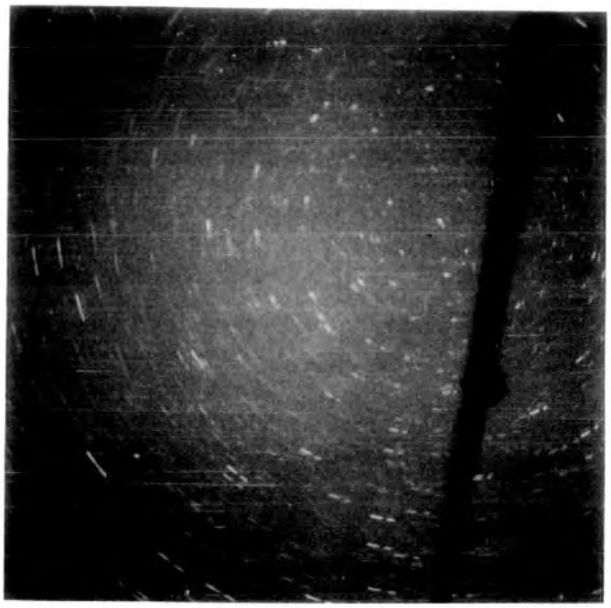

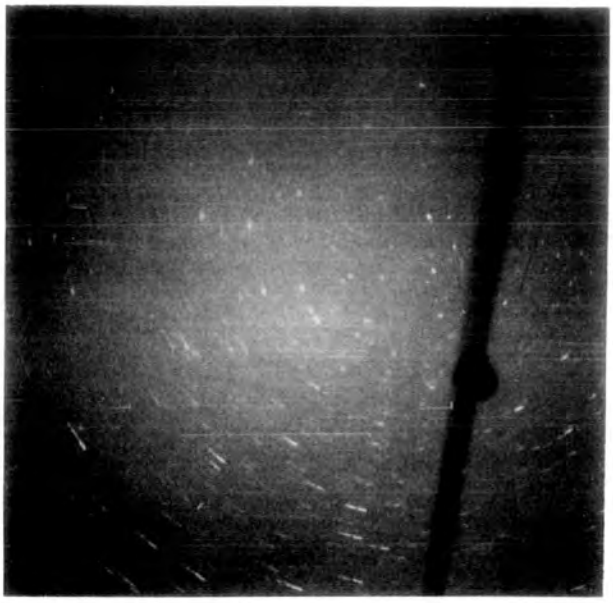

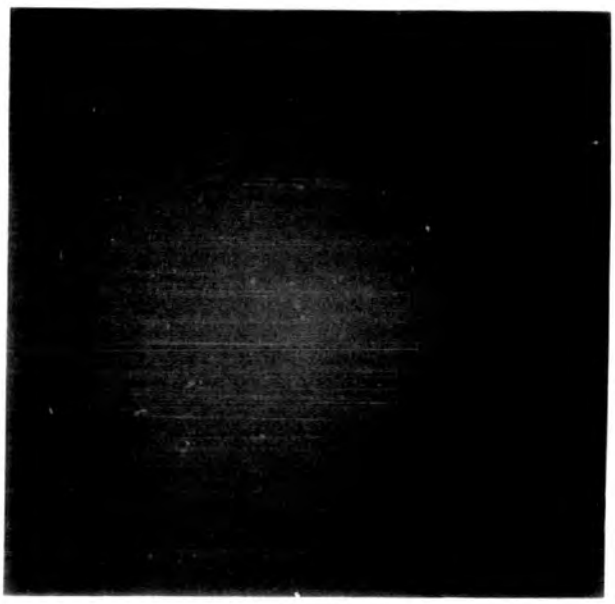

night like this, with patches of clear sky and cloud cover, was flagged as bad weather night and data from this night were not included in the analysis.

The atmospheric monitoring records for the night of 24 September 1979 are summarized in Figure 3.11. The records show a correlation between maximum detectable stellar magnitude and the PMT current, as well as the array trigger rate. This correlation is illustrated further in Figures 3.12 and 3.13. In Figure 3.12 the sky brightness (measured in PMT reading) is plotted for all data blocks from August to November 1979. On the same graph, the count rate per data block is also shown. Figure 3.13 shows the variation of count rate with sky brightness.

Figures 3.11, 3.12, and 3.13 indicate a dependence of observed Cerenkov light on night sky brightness and underline the importance of monitoring atmospheric conditions.

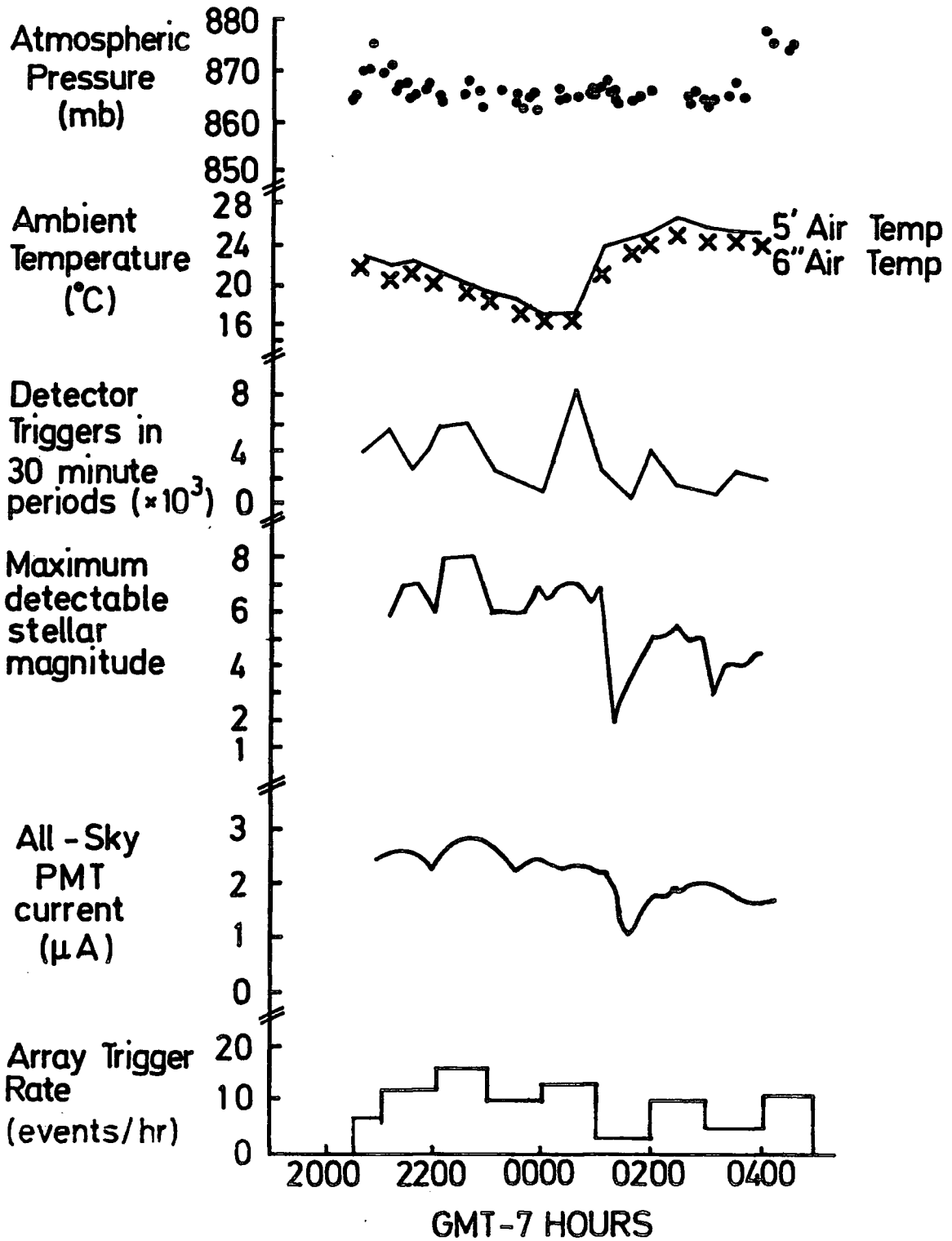

FIGURE 3.11

ATMOSPHERIC MONITORING INFORMATION FOR THE NIGHT OF 24 SEPTEMBER 1979.

FIGURE 3.12

COUNT RATE AND SKY BRIGHTNESS PER DATA BLOCK FOR

400m ARRAY, 1979/80

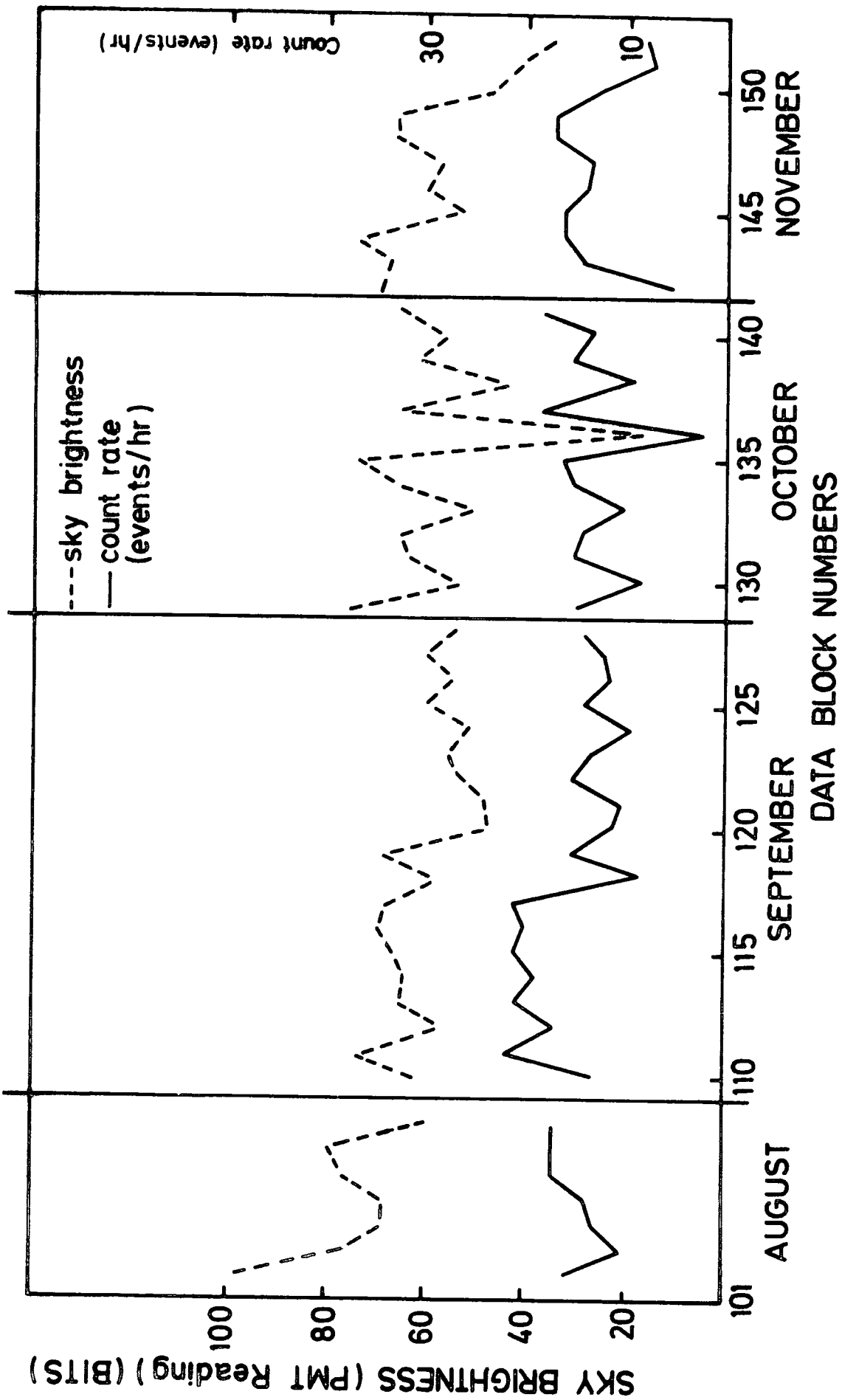
SKY BRIGHTNESS (PMT Reading) (BITS)
100
80
60
40
20
Count rate (events/hr)
30
10
---sky brightness
— count rate (events/hr)
101
110
115
120
125
130
135
140
145
150
AUGUST
SEPTEMBER
OCTOBER
NOVEMBER
DATA BLOCK NUMBERS

FIGURE 3.13

VARIATION OF COUNT RATE WITH SKY BRIGHTNESS.

WINTER 1979/80

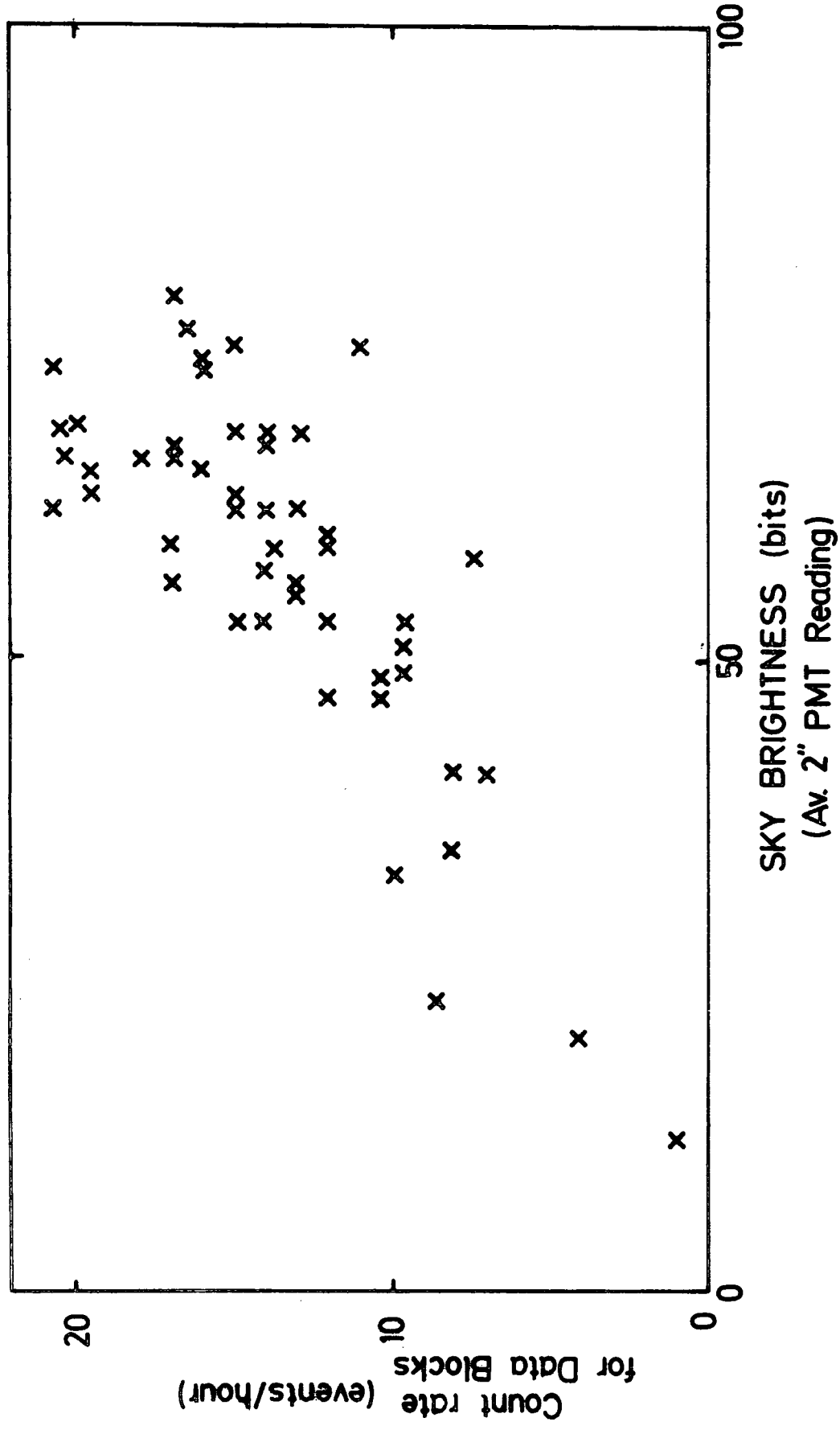
Count rate for Data Blocks (events/hour)
20
10
0
0
50
100
SKY BRIGHTNESS (bits)
(Av. 2" PMT Reading)

CHAPTER FOUR

PULSE SHAPE RECONSTRUCTION.

4.1 Introduction.

4.1.1 A Review of Methods of Pulse Shape Measurement.

The accurate determination of pulse shape parameters is necessary because of the important information on cascade development contained in the Cerenkov light profile. To date, most of the measurements on pulse shape have been made from photographs of oscilloscope displays of the light pulses. This technique has been used at Haverah Park (Hammond et al, 1978), Yakutsk (Kalmykov et al, 1979), and Adelaide (Thornton et al, 1979). From the oscilloscope photographs the pulse width and the time taken to reach a prescribed height have been measured.

4.1.2 Digitised Pulses from the Dugway Experiment.

At the Dugway Extensive Air Shower array, the pulse shape data were obtained in the form of a set of partially overlapping slices (See Section 3.3), which made up a histogram representation of the Cerenkov light pulse. The aim of this approach was to store all the information in a compact form on magnetic tape to bring back to Durham for future systematic analysis, after reconstruction of the light pulse shape. The obvious advantage of this technique over measurements from oscilloscope displays is the lack of bulky quantities of printed photographs to handle,

and the fact that once the digitised information had been transferred to computer discs and magnetic tapes they could be stored indefinitely. In addition, systematic data fitting procedures are more reproducible than measurements from photo-prints; and, provided a reliable method of numerical analysis could be evolved, the problem would then reduce to the errors of reconstruction which can also be assessed and allowed for.

4.1.3 Special Problems in the Reconstruction of Digitised Pulses.

The retrieval of pulse shape information from digitised pulses is not without its own problems, however. It is of crucial importance to have a thorough and up to date record of all decalibration constants for an accurate evaluation of the slice heights and times.

The digitising electronics must be checked and calibrated regularly to ensure that the sequential charge measurement is effectively done over the total time interval required. If there is a missing slice, as a result of malfunctioning of any of the electronic units used in generating the gating pulses, the reconstructed pulses would be distorted, resulting in pulse shapes which are not physically tenable.

The backbone of any information retrieval from the digitised pulse shape data is an effective data fitting procedure. The data fitting procedure used should cope with all light pulse sizes. The fitted curve should not merely be smooth for aesthetic satisfaction but should also enable us to compute efficiently the parameters of the original Cerenkov light pulse.

Hence, given the points :

$$x_1 < x_2 < \ldots \ldots < x_n < x_{n+1}$$

and the heights :

h_1 , h_2 , ... , h_n

where h_i is the height over the interval $[\, x_i \, , \, x_{i+1} \,]$, we require an approximation that would make the area $h_i \, \Delta x_i$ as close as possible to the integral of the underlying curve AB over the interval $[\, x_i \, , \, x_{i+1} \,]$, (See Figure 4.1).

We define the quantity ε as :

$$\varepsilon = \int_{x_1}^{x_{n+1}} F(x)\, dx \; - \; \sum_{i=1}^{n} h_i \Delta x_i \qquad 4.1$$

$$i = 1, 2, \ldots \qquad \ldots, n$$

where $F(x)$ is the smoothing function used, and choose a data fitting procedure to make ε^2 as small as possible. That is, we require the smoothing function, $F(x)$, to satisfy the least squares minimization condition :

$$\varepsilon^2 = \left[\int_{x_1}^{x_{n+1}} F(x) dx \; - \; \sum_{i=1}^{n} h_i \Delta x_i \right]^2 \Longrightarrow 0 \qquad 4.2$$

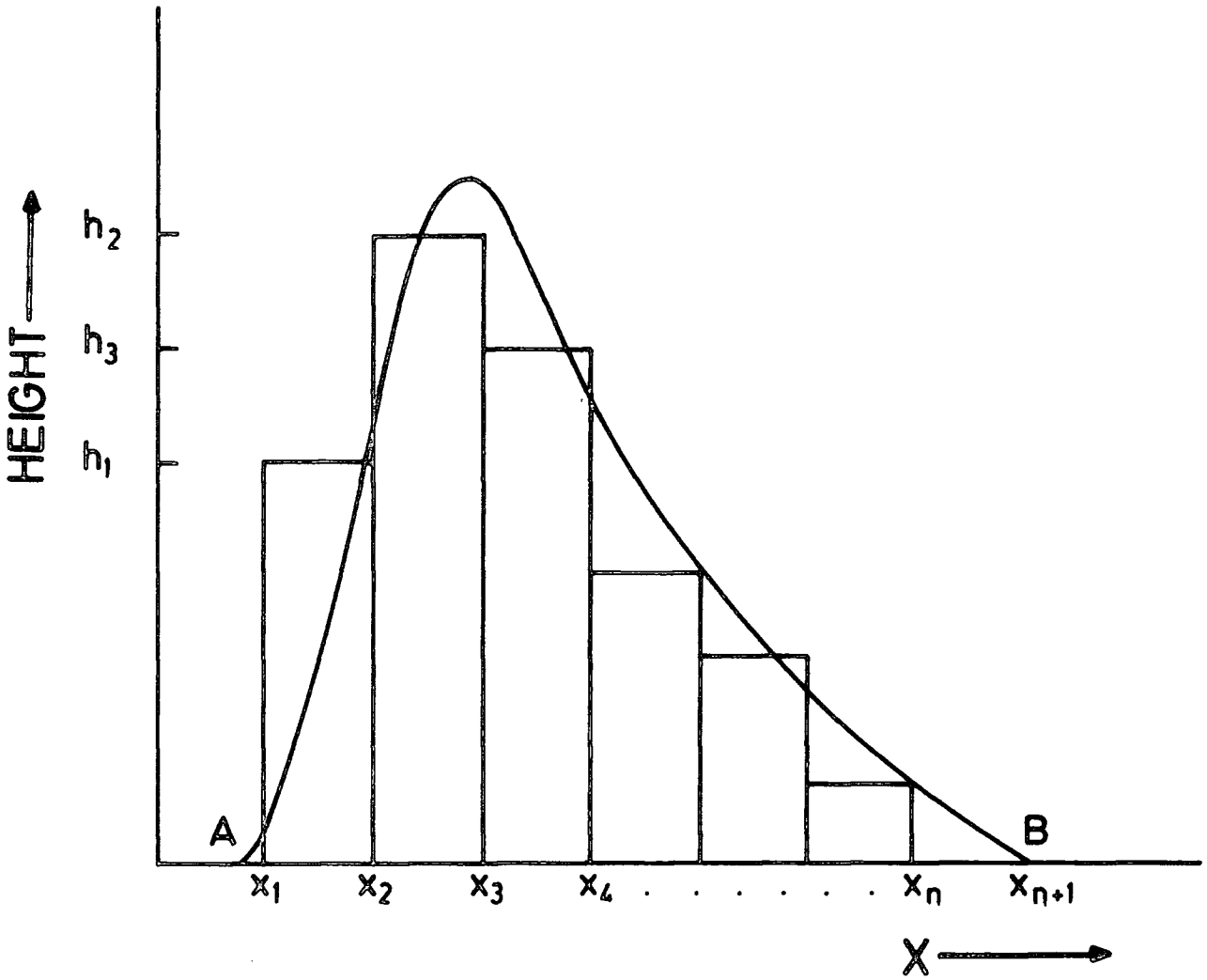

FIGURE 4.1

"AREA MATCHING" CURVE APPROXIMATION TO A HISTOGRAM.

4.1.4 Polynomial Approximation to Pulse Shape and its Limitations.

As a first approximation the function, $F(x)$, may be chosen as an n- degree polynomial :

$$F(x) = a_o + a_1 x + a_2 x^2 + \ldots + a_n x^n \qquad 4.3$$

Polynomial approximation is popular because polynomials can be evaluated, differentiated, and integrated easily and in finitely many steps using just the basic arithmetic operations; and their sums, products and differences are also polynomials.

However, in polynomial approximation, very high order polynomials are required to make the fitted curve change rapidly at the peak. This introduces smoothing problems as the very high order polynomials tend to fit the curve to all the given points, resulting in curve oscillation and interpolation at the cost of smoothing.

Another major limitation of polynomial approximation is the analyticity of polynomials. The behaviour of a polynomial is globally dependent on local properties in the interval of approximation. Therefore, if the function, $F(x)$, is badly behaved anywhere in the interval of approximation, then the approximation is poor everywhere. This global dependence on local properties restricts the use of a single polynomial to represent many physical quantities. Most physical quantities have functional forms whose behaviour in one region of the approximation interval does not necessarily reflect their behaviour throughout the interval. Any appropriate fitting procedure to practical data must therefore be able to allow for such variations in functional form.

4.2 Use of Moments to Determine Pulse Shape.

4.2.1 Second Moment as a Measure of Pulse Width.

A simple way to evaluate the pulse width from the Dugway data without recourse to elaborate data fitting procedure is to find the root mean square deviation of the slices about the mean, (i.e. the square root of the second order central moment).

We define our measure of the width of the Cerenkov light pulse as the square root of the variance of the slice widths, and denote it by M_2. The variation of M_2 with core distance should reflect the pulse width dependence on core distance.

For our computation, the histogram in Figure 4.1 may be treated as grouped data from a continuous distribution given in frequency form. If the frequency of the value x is $f(x)$, then the n^{th} moment of the distribution, μ_n, may be defined as :

$$\mu_n = \frac{\int_{-\infty}^{\infty} x^n f(x)\,dx}{\int_{-\infty}^{\infty} f(x)\,dx} \qquad 4.4$$

from which the Second Moment, μ_2, is directly derived as :

$$\mu_2 = \frac{\int_{-\infty}^{\infty} x^2 f(x)\,dx}{\int_{-\infty}^{\infty} f(x)\,dx} \qquad 4.5$$

For a continuous distribution sample :

x_1 , x_2 , . . . , x_n

of size n , the Second Moment is : (Pollard, 1977)

$$\mu_2 = \frac{1}{n}\sum_{\text{all } x} x^2 f(x) - \bar{x}^2 \qquad 4.6$$

where the mean, $\bar{x}$, is :

$$\bar{x} = \frac{1}{n}\sum_{\text{all } x} x\, f(x) \qquad 4.7$$

and the sample size, n , is :

$$n = \sum_{\text{all } x} f(x) \qquad 4.8$$

But the variance, σ^2 , is the same as the Second Order Central Moment, μ_2 . Hence,

$$M_2 = \sigma = \mu_2^{1/2} \qquad 4.9$$

and

$$M_2 = \left\{ \frac{\sum x^2 f(x)}{\sum f(x)} - \left[\frac{\sum x f(x)}{\sum f(x)} \right]^2 \right\}^{1/2} \qquad 4.10$$

For our purpose, x , $f(x)$ are the slice width in time, t , and corresponding slice height, $h(t)$, respectively.

Oscilloscope displays of Cerenkov light show the pulses to have a skew distribution with a long tail to the right. The third order central moment of such a distribution would be positive and would give a measure of the growth of the pulse (i.e. a measure of the Rise Time).

4.2.2 Second Moment of Simulated Pulses Compared with FWHM.

Computer simulation data have been used to check the validity of Second Moment as a measure of pulse width. The computer program developed for this purpose reads in pulse heights at given times and simulates the slicing of the pulse, with the slice configuration of the particular detector under study. The night sky background noise was also simulated and added to the slices. This was done by a random number generating subroutine with a Gaussian distribution of RMS 5mV. The RMS of 5mV was chosen from considerations of the night time pedestal calibrations. The slice heights were rounded to the nearest integer multiple of 2mV to account for bit quantisation.

A matrix of simulated pulses, of different widths and heights has been investigated. The variation of the width parameter, M_2 , with

the simulated pulse FWHM is shown in Figure 4.2. The graph does not show a direct one-to-one relation between M_2 and simulated pulse FWHM. For pulses of FWHM > 16ns, M_2 is systematically less than FWHM for all pulse heights. For pulses of FWHM between 6ns and 12ns the value of M_2 obtained depends on the height of the pulse. This variation is more evident for very narrow pulses (FWHM < 8ns). Hence, for these pulses, M_2, can be used as a reliable measure of width only after systematic correction to the measured value.

4.2.3 An Estimate of Peak Height from Second Moment and Photon Density.

In order to determine an alternative measurement to Peak Height from Moments, the quantity :

$$H_s = \frac{\sum SL}{M_2} \qquad 4.11$$

has been computed, where $\sum SL$ is the total light intensity (optical photon density) for the simulated pulse.

Figure 4.3 illustrates the relationship between H_s and the Peak Height of simulated pulses. This relationship shows a consistent over-estimate of H_s for medium to broad pulses, on account of the low value of the pulse width shown in Figure 4.2. For these pulses, the computed height parameters, H_s would need to be corrected systematically before they can be interpreted to give a consistent indication of pulse heights.

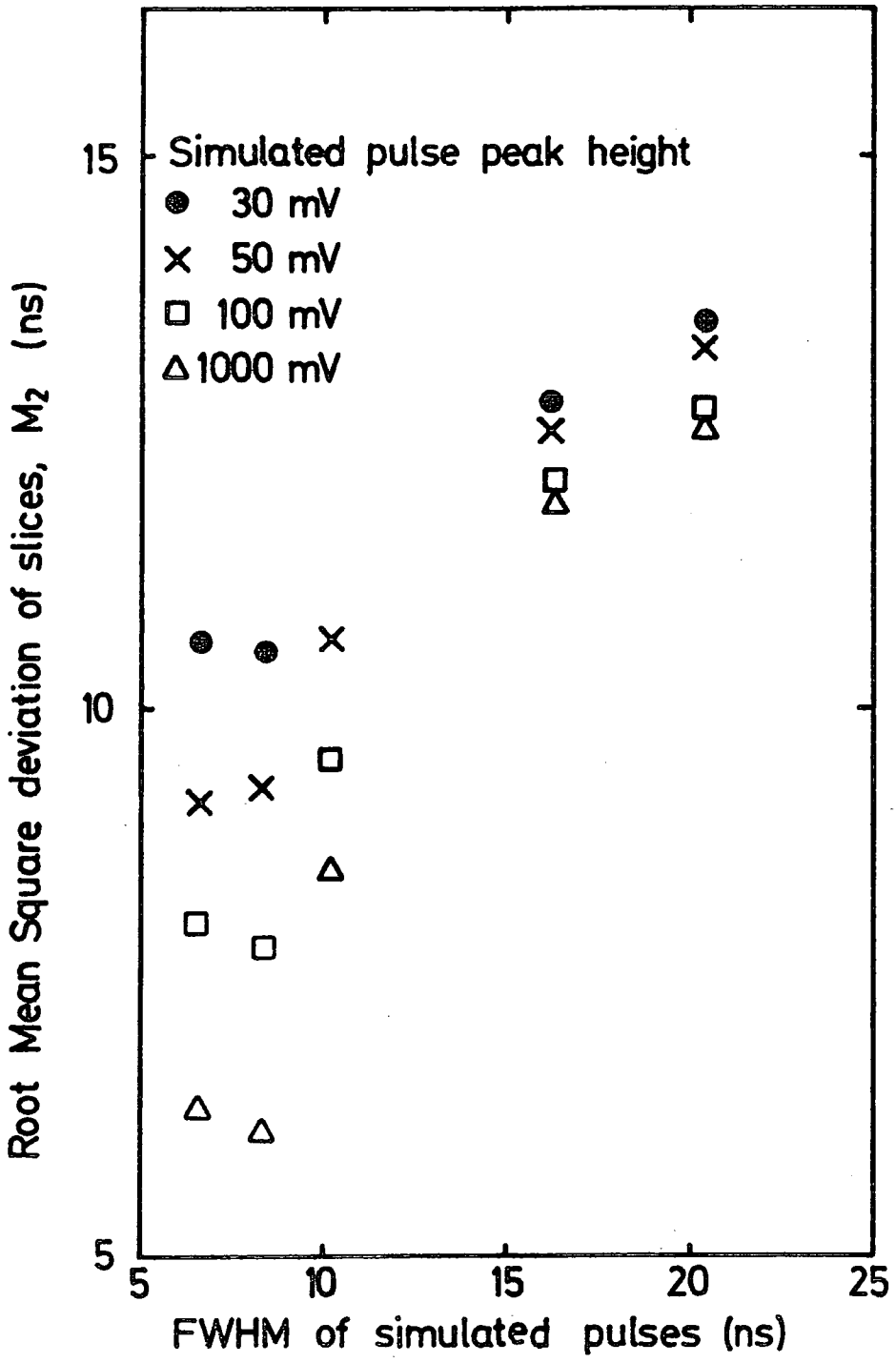

FIGURE 4.2

THE RELATION BETWEEN M_2 AND FWHM FOR SIMULATED PULSES

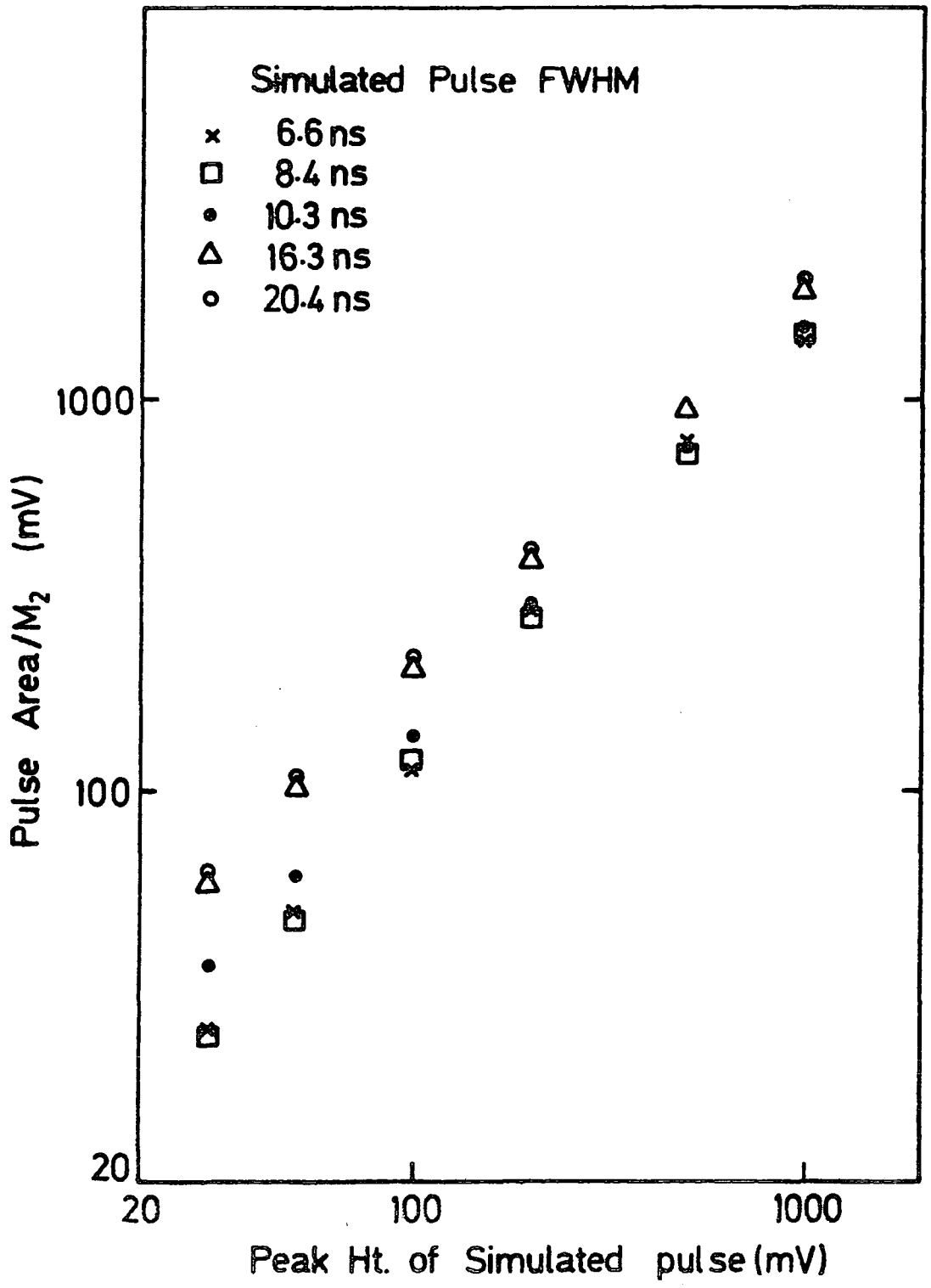

FIGURE 4.3

H_s , A DERIVED MEASURE OF PULSE HEIGHT, COMPARED WITH THE PEAK HEIGHT OF SIMULATED PULSES

4.2.4 Limitations in the Use of Moments as Pulse Shape Estimators.

The main disadvantage in the use of Moments is the critical dependence on slice positions. This dependence implies that any loss of information due to inaccurate slice position would lead to the evaluation of a width that is too narrow. Furthermore, the evaluation of M_2 does not account for the overlapping of the slices and this can lead to differences in pulse width due mainly to a detector's ability to slice up the pulses.

It appears therefore, that the use of Moments is limited to only the small fraction of well measured pulses from detectors whose slices do not overlap. For most of the data we require systematic pulse shape reconstruction techniques that would account for the total pulse area.

4.3 Trial Unimodal Functions.

One possibility of reconstructing the pulse shape is to fit a unimodal fast-rising, slow-decaying function to the observed slices. Our choice of such a function has been guided by the observed shapes of the Cerenkov light pulses from oscilloscope displays. One class of functions which satisfy this condition, and are quick to compute, is the Pearson type functions. The use of a Pearson type function has been investigated for reconstruction of the Dugway data and the results are summarized below.

4.3.1 Pearson Function.

The general form of the Pearson type III function is :

$$P(t) \propto t^{\delta} e^{-t/\beta} \qquad 4.12$$

where δ and β are constants. Equation 4.12 is really a combination of two equations ; the first part :

$$P(t) \propto t^{\delta} \qquad 4.13$$

indicates the growth of the pulse (or the leading edge) while the exponential part :

$$P(t) \propto e^{-t/\beta} \qquad 4.14$$

represents the back edge of the pulse. By combining different values of δ and β we are able to produce distributions with varying degrees of skewness and kurtosis. The results of this theoretical study are summarized in Figure 4.5.

For our computation we have used an equation of the form :

$$P(t) = A(t+\tau)^{\delta} e^{-(t+\tau)/\beta} \qquad 4.15$$

where $P(t)$ is the pulse height at a given time, t ,

τ is a time-axis parameter to account for the different slice

FIGURE 4.5

SOME OF THE DIFFERENT DISTRIBUTIONS OBTAINED BY VARIOUS COMBINATIONS OF β AND δ IN THE PEARSON FUNCTION :

$$P(t) = t^{\delta} e^{-t/\beta}$$

Function: $P(t) = t^{\delta} e^{-t/\beta}$

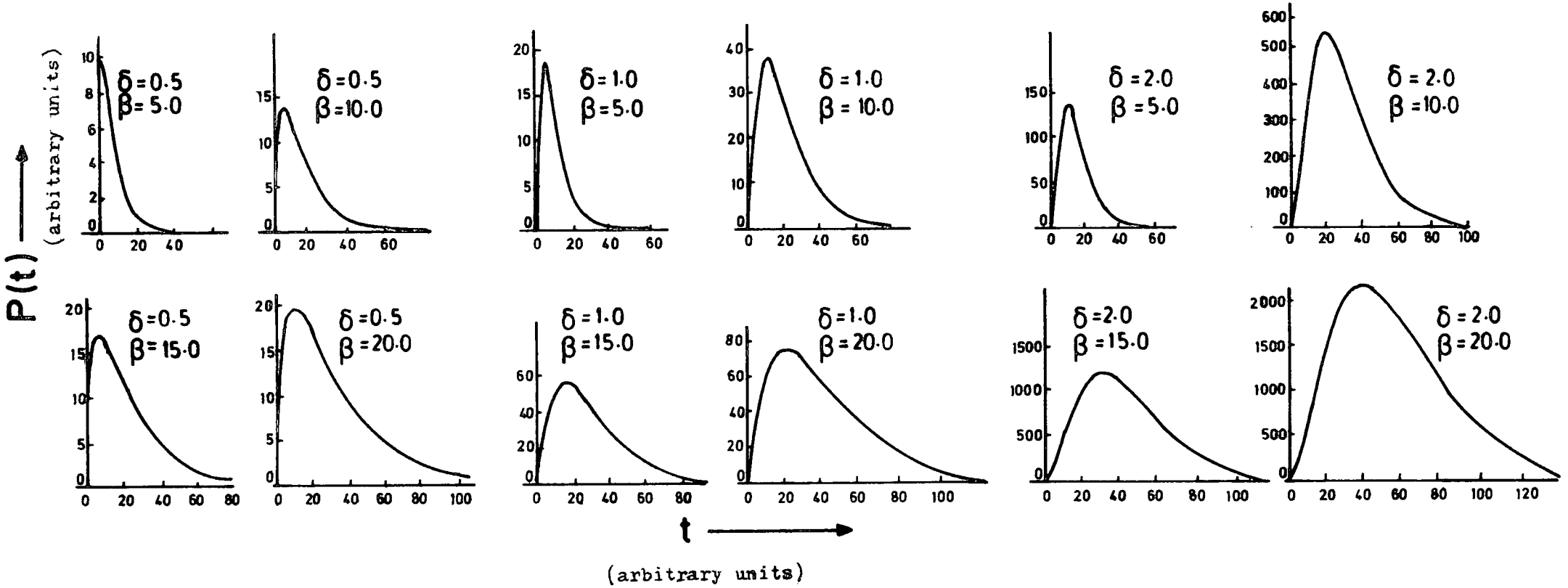

configurations of the detectors ,

and A is a normalisation factor.

P(t) is then used as the function F(x) in the least squares minimization criterion in Equation 4.2.

To compute P(t) two main options are open to the programmer :

(1) The values of τ , δ and β may be fixed at pre-determined levels (on the basis of theoretical studies) with the normalisation factor being allowed to vary until ε^2 in Equation 4.2 is a minimum.

(2) τ , δ and β may be used as variables, with the constraint that the integral of the function P(t) over the time interval used should be equal to the area under the histogram, (Figure 4.1).

The second option has been used in this work because it allows more flexibility in the reconstruction and gives a fit that is unique to every set of slice configuration. The least squares minimization package MINUIT (James and Roos, 1975) has been used to vary τ , δ and β between prescribed limits to satisfy the least squares criterion in Equation 4.2. MINUIT uses a combination of a Monte Carlo searching technique and the Simplex method of Nelder and Mead (1967).

A useful approximation that eliminates the need for an integration, and therefore saves computing time, is :

$$\int_0^\infty x^n e^{-ax} dx = \frac{\Gamma(n+1)}{a^{n+1}} \qquad 4.16$$

Hence,

$$\int_0^\infty P(t)\,dt = A \left[\frac{a^{n+1}}{\Gamma(n+1)} \right] \int_0^\infty (t^n e^{-at})\,dt = A \qquad 4.17$$

where $n = \delta$

$a = 1/\beta$ in Equation 4.15 ,

and A = area of the pulse, used as a normalisation factor.

4.3.2 Pearson Function Fits to Simulated Pulses.

Computer simulation pulses of different widths and sizes have been divided into slices appropriate to the detector characteristics, using a technique similar to that used in the study on Second Moments (See Section 4.2.2). The histograms formed by the slices have been fitted with Pearson type III functions as described in Section 4.3.1.

In Figure 4.6 the Pearson function fits to the simulated pulses are shown against the expected pulse shapes from the simulation data. The graphs are drawn to different scales for each set of simulated pulse and Pearson fit.

The results summarized in Figure 4.6 indicate that Pearson functions can cope with the reconstruction of Cerenkov light pulses of height > 50 mV and medium width ($\gtrsim 20$ ns). For narrow pulses, there is a systematic trend to over-estimate the pulse width and under-estimate the height. Hence, the Pearson function fits to simulated pulses of width 10 ns or less are all wider, but have a reduced height, compared to the input simulated pulse. This might be due to the strong effect of the exponential part of Equation 4.15, which causes the fitted shape to fall before it has developed along the full length of the leading edge.

The wide spectrum of pulse sizes and widths expected from our data necessitates the use of a fitting function that is more flexible than Pearson type functions.

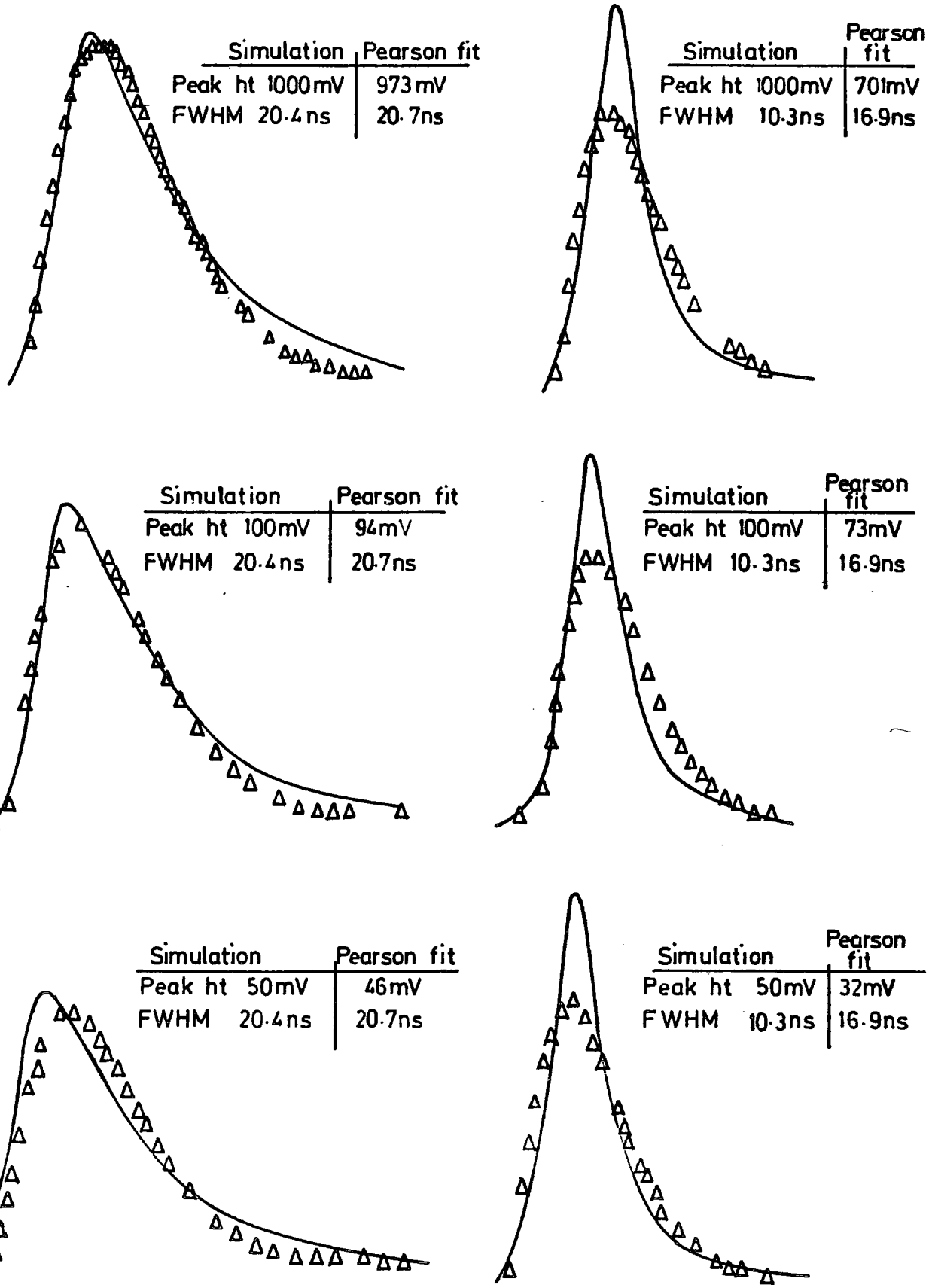

FIGURE 4.6

PEARSON FUNCTION FITS TO SIMULATED CERENKOV LIGHT PULSES.

—— INPUT SIMULATED PULSE Δ PEARSON FIT

4.4 Pulse Shape Reconstruction with Splines.

In the previous Sections of this Chapter attention has been drawn to the limitations of polynomials, Second Moments and Pearson functions as effective tools for the retrieval of pulse shape information from digitised data.

Second Moments are quick to compute but depend critically on the slice positions, and give only an approximate determination of the pulse shape.

Pearson functions give adequate reconstruction of the shapes of medium to wide pulses, but are not flexible enough to cope with small, narrow pulses.

Polynomials, like Pearson functions, are not flexible enough as smoothing functions; and they also have the major drawback of a global dependence on local properties.

The most effective way to represent physical data is to choose a fitting function that allows for the irregularities in functional form. The set of mathematical functions called 'splines', first proposed by Schoenberg in 1946, have just this inherent flexibility.

Splines are localised fits or piecewise polynomials whose segments are defined only in a limited range of the independent variable, with the constraint that the polynomial segments must have continuity of function and derivative at the joints or 'knots'. This inherent property gives rise to a function that is smooth and continuous anywhere inside the boundary limits but vanishes outside the boundaries.

The similarity between a mathematical spline and the old draughtsman's tool consisting of a strip of bamboo with lead weights, or the modern plastic 'Flexi-curve' is not hard to find.

This remarkable flexibility of splines has been put to advantage in the reconstruction of the pulse shapes from the Dugway data (i.e. the function $F(x)$ in Equation 4.2 has been chosen as a spline). In the following Sections, the basic theory of splines is outlined and the use of splines in our data analysis procedure is discussed in detail.

4.4.1 Brief Theory of Splines.

For a set of real numbers, strictly increasing in the order :

x_1 , x_2 , ... , x_n ,

a spline function $S(x)$ of degree m (or order $m+1$) with the knots :

x_1 , x_2 , ... , x_n ,

is a function defined on the entire real line having the following two properties :

(a) In each interval (x_i , x_{i+1}) for

$i = 0, 1, \ldots n$,

$S(x)$ is given by some polynomial of degree m or less.

(b) $S(x)$ and its derivatives of orders $1 , 2 , \ldots , m-1$ are continuous everywhere in the interval of approximation.

These properties enable us to divide the curve into sections (See Figure 4.7) and treat each section as an entity with the constraint that adjacent polynomials must have

(i) the same function, $F(x)$;

(ii) the same slope, $F'(x)$; and

(iii) the same curvature, $F''(x)$.

Hence, in the fitting procedure, any suitable spline function may be chosen to fulfil the least squares minimization criterion in Equation 4.2.

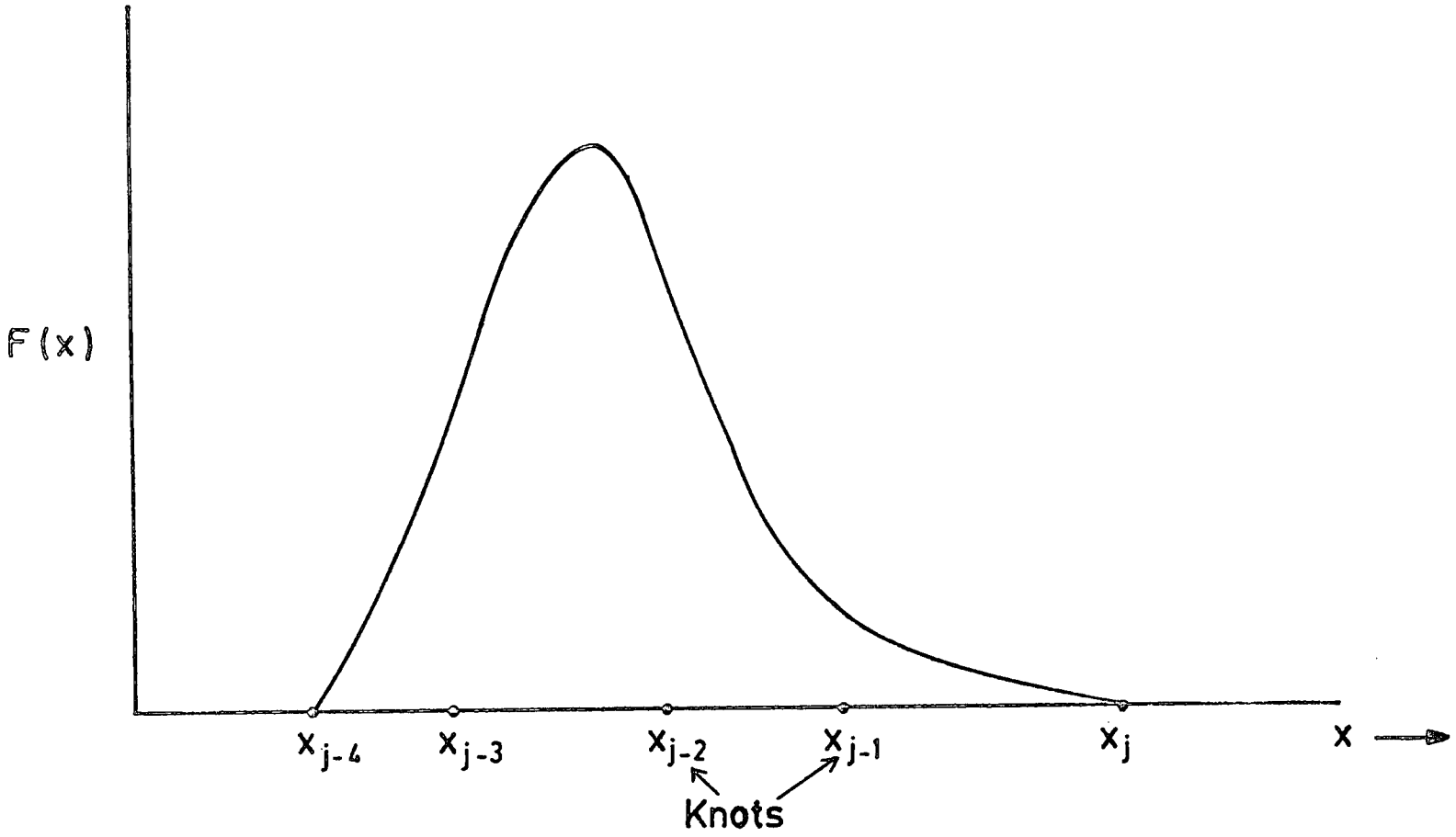

FIGURE 4.7

THE KNOTS OF A CUBIC SPLINE, $M_{4j}(x)$

Suitable functions include the exponential function (whose limit is the well-known Gaussian) and Taylor's series, (Rice, 1969).

In general, the simplest spline function to satisfy the conditions outlined in (i), (ii), and (iii) above is a cubic B-spline whose basis is the truncated power function :

$$X_+^n = \begin{cases} X^n & , \text{ for } X \geq 0 \\ 0 & , \text{ for } X < 0 \end{cases} \qquad 4.18$$

Definition :

Let

$$F(x) = (x_r - x)_+^{n-1}$$

$$= \begin{cases} (x_r - x)^{n-1} & , \text{ for } x_r \geq x \\ 0 & , \text{ for } x_r < x \end{cases} \qquad 4.19$$

Then the B-spline can be evaluated on the r^{th} knot position, x_r, using this definition and the divided differences of $F(x)$ in x_r for any fixed x.

We define the first divided difference of $F(x)$ on x_1, and x_o as $M(x_o, x_1)$ where

$$M(x_o, x_1) = \frac{F(x_1) - F(x_o)}{x_1 - x_o} \qquad 4.20$$

The divided difference of order m is :

$$M(x_j; x_o, \ldots x_m) = \frac{M(x_j; x_1, \ldots x_m) - M(x_j; x_o, \ldots x_{m-1})}{x_m - x_o} \qquad 4.21$$

It follows from Equation 4.21 that :

$$M(x_j; x_o, x_1) = \frac{M(x_j, x_1) - M(x_j, x_o)}{x_1 - x_o} \qquad 4.22$$

and

$$M(x_j, x_i) = F(x_i) \qquad 4.23$$

By expansion of the divided difference formula the localised spline of order n (or degree n-1), which we denote here as M_{ni}, is defined as :

$$M_{ni}(x) = M(x_j ; x_0, x_1, \ldots, x_n)$$

$$= \sum_{i=0}^{n} \frac{F(x_i)}{\prod_{\substack{j=0 \\ j \neq 1}}^{n} (x_i - x_j)} \qquad 4.24$$

with the property that :

$$\int_{-\infty}^{\infty} M_{ni}(x)\,dx = \frac{1}{n} \qquad 4.25$$

The relationship in Equation 4.25 can be allowed for by using $\frac{1}{n}$ as a normalisation factor in the computation.

4.4.2 An Algorithm for Computing the B-Spline.

The computer program developed to evaluate the spline in our fitting procedure has been based on the algorithm proposed by Cox (1972). Although B-splines may be evaluated directly from the divided difference definition, Cox has pointed out that some evaluation may fail because of cancellation of nearly equal terms. Our computation used his stable method based on the recurrence relation :

$$M_{ni}(x) = \frac{(x - x_{i-n})M_{n-1,i-1}(x) + (x_i - x)M_{n-1,i}(x)}{x_i - x_{i-n}} \qquad 4.26$$

where M_{ni} is a spline of order n ending on knot x_i ; $M_{n-1,i-1}(x)$, $M_{n-1,i}(x)$ are the $(n-1)$th divided differences on x_{i-1} and x_i respectively.

A unimodal quartic spline has been chosen in this work as the fitting function. There is a maximum of 7 data points (i.e. a maximum of 6 slices plus 1 discriminator level). Constrained by the 2 end knots, we are left with 5 degrees of freedom, justifying our choice of a quartic spline with $n = 5$, and 6 knots.

The use of Equation 4.26 involves the calculation of all backward divided differences preceding $M_{ni}(x)$. For example, for a quartic spline, ($n = 5$), the elements in the triangular array in Table 4.1 are computed.

It is worth noting that :

$$M_{ij}(x) = \begin{cases} 1/(x_j - x_{j-1}) \ , & \text{for } x_{j-1} \leq x \\ 0 & \text{, for all other values of } x \end{cases} \qquad 4.27$$

Equation 4.27 therefore reduces the number of individual calculations required.

TABLE 4.1

TRIANGULAR ARRAY OF ELEMENTS FOR A QUARTIC SPLINE

	1st divided differences	2nd divided differences	3rd divided differences	4th divided differences	5th divided differences
x_{i-5}					
	$M_{1,i-4}$				
x_{i-4}		$M_{2,i-3}$			
	$M_{1,i-3}$		$M_{3,i-2}$		
x_{i-3}		$M_{2,i-2}$		$M_{4,i-1}$	
	$M_{1,i-2}$		$M_{3,i-1}$		$M_{5,i}$
x_{i-2}		$M_{2,i-1}$		$M_{4,i}$	
	$M_{1,i-1}$		$M_{3,i}$		
x_{i-1}		$M_{2,i}$			
	$M_{1,i}$				
x_i					

If, for example, $x_{i-2} \leqslant x < x_{i-1}$, all the terms in the first divided difference column are zero except $M_{1,i-1}$ and the triangular array (Table 4.1) reduces to Table 4.2. Only the terms in the rhomboidal array in Table 4.2 then need be computed.

To compute the spline we set :

$$M_{ij} = M_{ij}(t) \quad , \quad j = 1, i-n+1, i-n+2, \ldots, i \qquad 4.28$$

We compute

$$M_{rj} = \frac{(t-t_{j-r})M_{r-1,j-1} + (t_j - t)M_{r-1,j}}{t_j - t_{j-r}} \qquad 4.29$$

where t_j and t_{j-r} are the times for the observed slice heights and t is any given time, for

$j = i-n+r , \quad i-n+r+1 , \quad \ldots , i$

$r = 2 , \quad 3 , \quad \ldots , n .$

Then

$$M_{ni}(x) = M_{ni} \qquad 4.30$$

TABLE 4.2

RHOMBOIDAL ARRAY OF ELEMENTS FOR A QUARTIC SPLINE OBTAINED BY APPLYING THE RELATION IN EQUATION 4.27

	1st divided differences	2nd divided differences	3rd divided differences	4th divided differences	5th divided differences
x_{i-5}					
	0				
x_{i-4}		0			
	0		0		
x_{i-3}		0		$M_{4,i-1}$	
	0		$M_{3,i-1}$		$M_{5,i}$
x_{i-2}		$M_{2,i-1}$		$M_{4,i}$	
	$M_{1,i-1}$		$M_{3,i}$		
x_{i-1}		$M_{2,i}$			
	0				
x_i					

4.4.3 Splines with Fixed Knot Positions.

As a consequence of its basic definition, the shape of a spline does not depend on the two end knots but only on the position of the middle knots.

Assuming a unimodal spline for the pulse, and no other information about the structure of the underlying data, an initial choice of closely spaced knots around the peak and a rapidly decreasing density of knots away from the peak would seem appropriate. This would require a prior guesstimate of the turning point in the pulse, a random and time-consuming process. A solution to this is the use of variable knots.

4.4.4 Splines with Variable Knot Positions.

De Boor and Rice (1968(a), 1968(b)) have shown that approximation to data by splines improves greatly if the knots are free variables. This improvement is illustrated by their data (p. 18 of Ref. 1968(a), p. 15 of Ref. 1968(b)), which have been plotted by this author, in Figure 4.8. These curves show the close approximation of the optimized spline, with 7 knots used as variables, to experimental data relating to a thermal property of titanium. Superimposed on the smooth fit are the oscillatory fits of a fixed knot cubic spline.

4.4.5 Use of MINUIT to Relax Knot Positions.

The quartic spline in this work has been computed as a variable-knot spline. The knots have been allowed to vary between pre-set boundaries, while satisfying non-linear least squares minimization criteria, by the

FIGURE 4.8

CUBIC SPLINE FIT WITH (A) 7 FIXED KNOTS (B) 7 VARIABLE KNOTS TO OBSERVED DATA RELATING TO A THERMAL PROPERTY OF TITANIUM (de Boor and Rice, (1968 a), (1968 b))

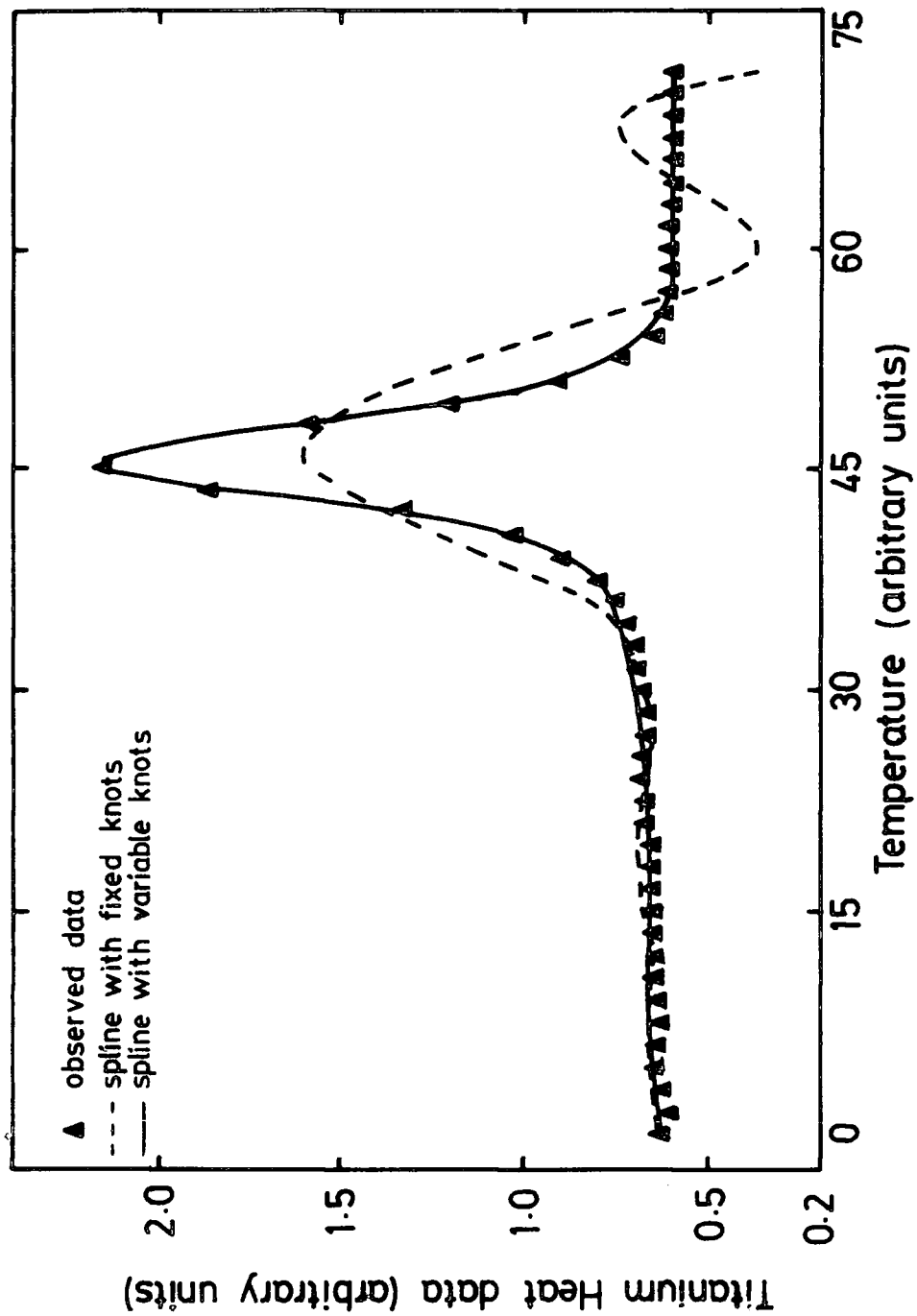
Titanium Heat data (arbitrary units)
2.0
1.5
1.0
0.5
0.2
0
15
30
45
60
75
Temperature (arbitrary units)
observed data
spline with fixed knots
spline with variable knots

use of MINUIT (James and Roos, 1975). MINUIT uses three main minimization techniques, viz. SEEK, SIMPLEX, and MIGRAD. The SEEK command is used first in a Monte Carlo searching technique to obtain an approximate minimum. This is followed by the MINIMIZE command which incorporates the SIMPLEX method of Nelder and Mead (1967) and MIGRAD, based on the algorithm of Fletcher (1970), to obtain a more refined minimum. A consecutive MINIMIZE command completes the least squares fit, and the optimal knot locations are then used for computing the spline.

4.5 Quartic Spline Fits to Computer Simulation Data.

Figure 4.9 shows a set of simulated pulses which have been spline-fitted. These are the same pulses fitted by Pearson functions, shown in Figure 4.6. The slice positions used here are for the same detector as in Figure 4.6 for easy comparison with the Pearson function fits. The pulses shown are drawn to different scales, but each pulse from the spline-fit is drawn to the same scale as the corresponding pulse from Pearson function fits. Figure 4.9 shows the close approximation of the spline to the simulation data over all pulse sizes tested and shows that the spline can cope with narrow as well as wide pulses.

The computer program has been tested to determine if spline-fitting introduces any systematic errors in the reconstruction of pulse shapes. A matrix of simulated pulses, of FWHM between 6.5 ns and 65 ns and pulse height 25 mV to 1000 mV have been spline-fitted.

Firstly, the pulses have been reconstructed with no noise on them, to determine errors due to spline-fitting alone. Secondly, these pulses have been reconstructed after the addition of random noise to account for

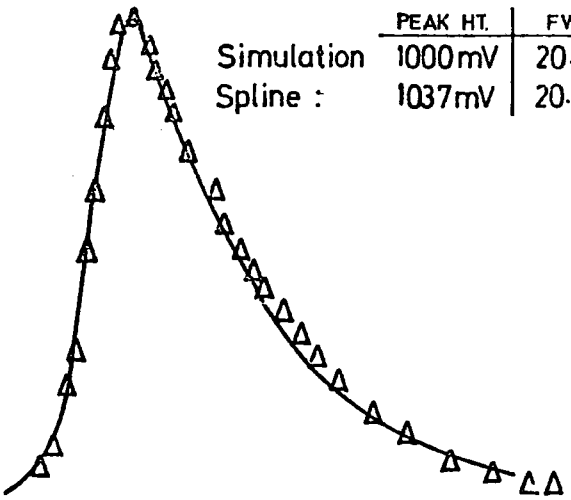

	PEAK HT.	FWHM
Simulation	1000 mV	20·4 ns
Spline :	1037 mV	20·6 ns

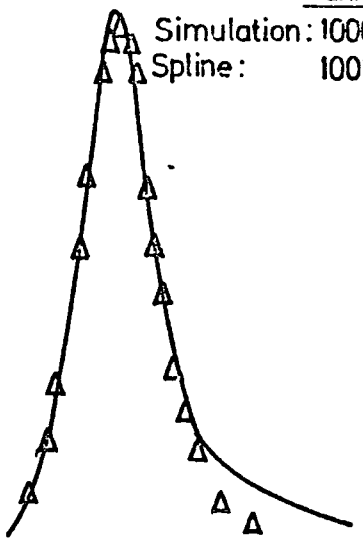

	PEAK HT.	FWHM
Simulation :	1000 mV	10·3 ns
Spline :	1007 mV	11·2 ns

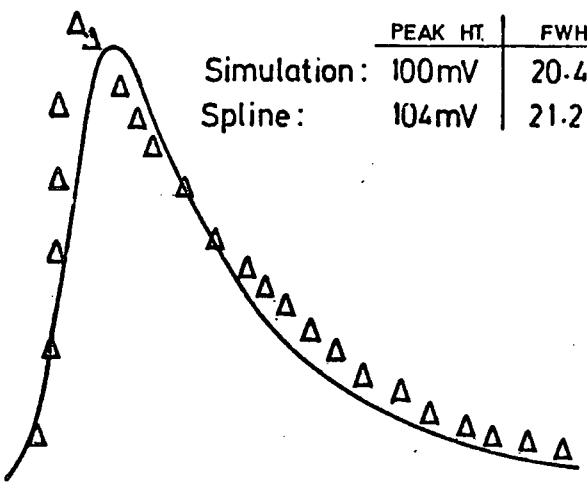

	PEAK HT.	FWHM
Simulation :	100 mV	20·4 ns
Spline :	104 mV	21·2 ns

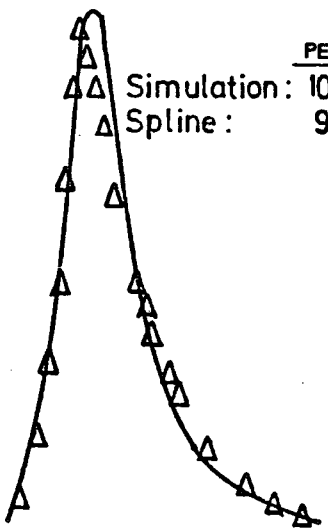

	PEAK HT.	FWHM
Simulation :	100 mV	10·3 ns
Spline :	98 mV	9·8 ns

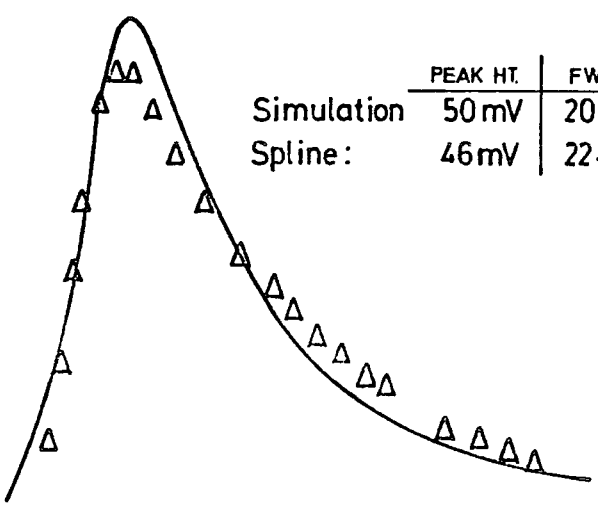

	PEAK HT.	FWHM
Simulation	50 mV	20·4 ns
Spline :	46 mV	22·5 ns

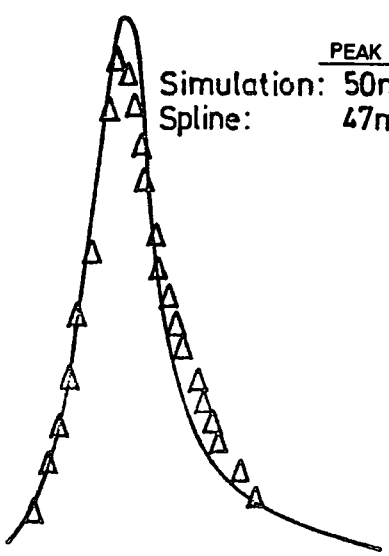

	PEAK HT.	FWHM
Simulation :	50 mV	10·3 ns
Spline :	47 mV	10·2 ns

FIGURE 4·9

QUARTIC SPLINE FITS TO SIMULATED CERENKOV LIGHT PULSES.

——— INPUT SIMULATED PULSE Δ SPLINE FITS

sky background noise on the measured Cerenkov light pulses, (See Section 4.2.2). The results of this study are summarized below.

We denote the total error between the percentage points (T10%, T50%(up), T90%(up), T100%, T90%(down), T50%(down)) of the spline-fitted pulse and the original simulated pulse by σ_{times} . Figures 4.10 and 4.11 summarize the variation of σ_{times} with simulated pulse peak height for the slice configurations of a typical outer detector and a typical inner detector. These figures show that the errors on the percentage points increase sharply if the pulse height decreases from 100 mV to 25 mV, but do not increase much above 100 mV. This indicates that the background sky noise does not affect the percentage levels significantly above 100 mV but must be allowed for for pulses smaller than 100 mV.

The effect of sky noise on the peak height of the spline-fitted pulses is summarized in Figure 4.12. The solid line represents the 5 mV error level; i.e. the percentage change in the peak height when there is an error of exactly 5 mV on the slices and discrimination level. The spread of the errors about the solid line shows the extent of background noise error on the measured pulse heights, and indicates a need for a correction to the pulse heights.

Figure 4.13 shows the comparison between FWHM of the simulated pulses and FWHM from the spline-fits for pulses of height 50 mV, 500 mV and 1000 mV. The graph shows good agreement between FWHM from the spline-fits and the simulated pulse FWHM for all the pulse sizes considered.

Detailed errors in FWHM and Rise Time due to spline-fitting alone are listed in Table 4.3 and Table 4.4. Tables 4.5 and 4.6 summarize the errors in FWHM and Rise Time for noisy simulated pulses. These errors

FIGURE 4.10

VARIATION OF RMS OF PERCENTAGE LEVELS WITH SIMULATED PULSE HEIGHT. (OUTER DETECTOR)

FIGURE 4.11

VARIATION OF RMS OF PERCENTAGE LEVELS WITH SIMULATED PULSE HEIGHT, (INNER DETECTOR)

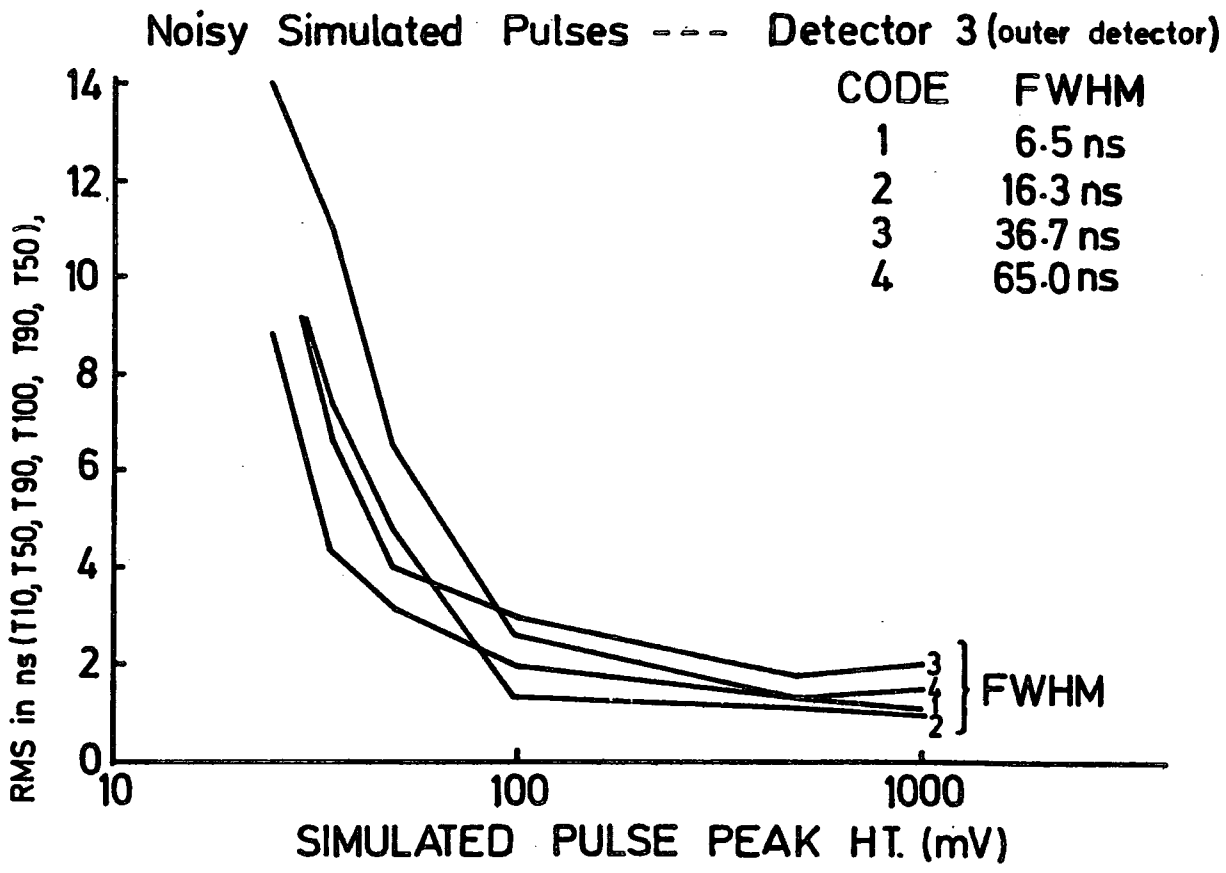
Noisy Simulated Pulses --- Detector 3 (outer detector)
CODE FWHM
1 6·5 ns
2 16·3 ns
3 36·7 ns
4 65·0 ns
RMS in ns (T10, T50, T90, T100, T90, T50),
SIMULATED PULSE PEAK HT. (mV)
FWHM

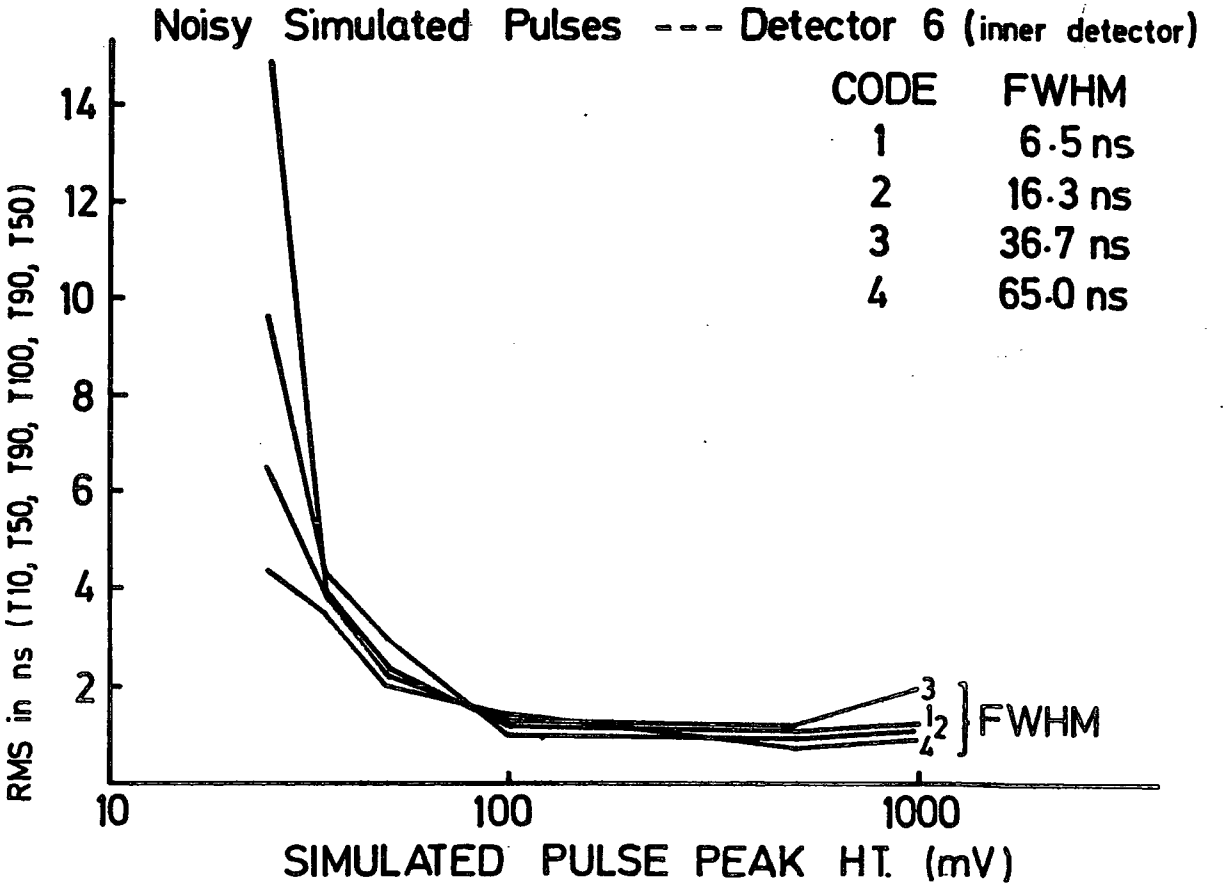
Noisy Simulated Pulses --- Detector 6 (inner detector)
CODE FWHM
1 6·5 ns
2 16·3 ns
3 36·7 ns
4 65·0 ns
RMS in ns (T10, T50, T90, T100, T90, T50)
SIMULATED PULSE PEAK HT. (mV)
FWHM

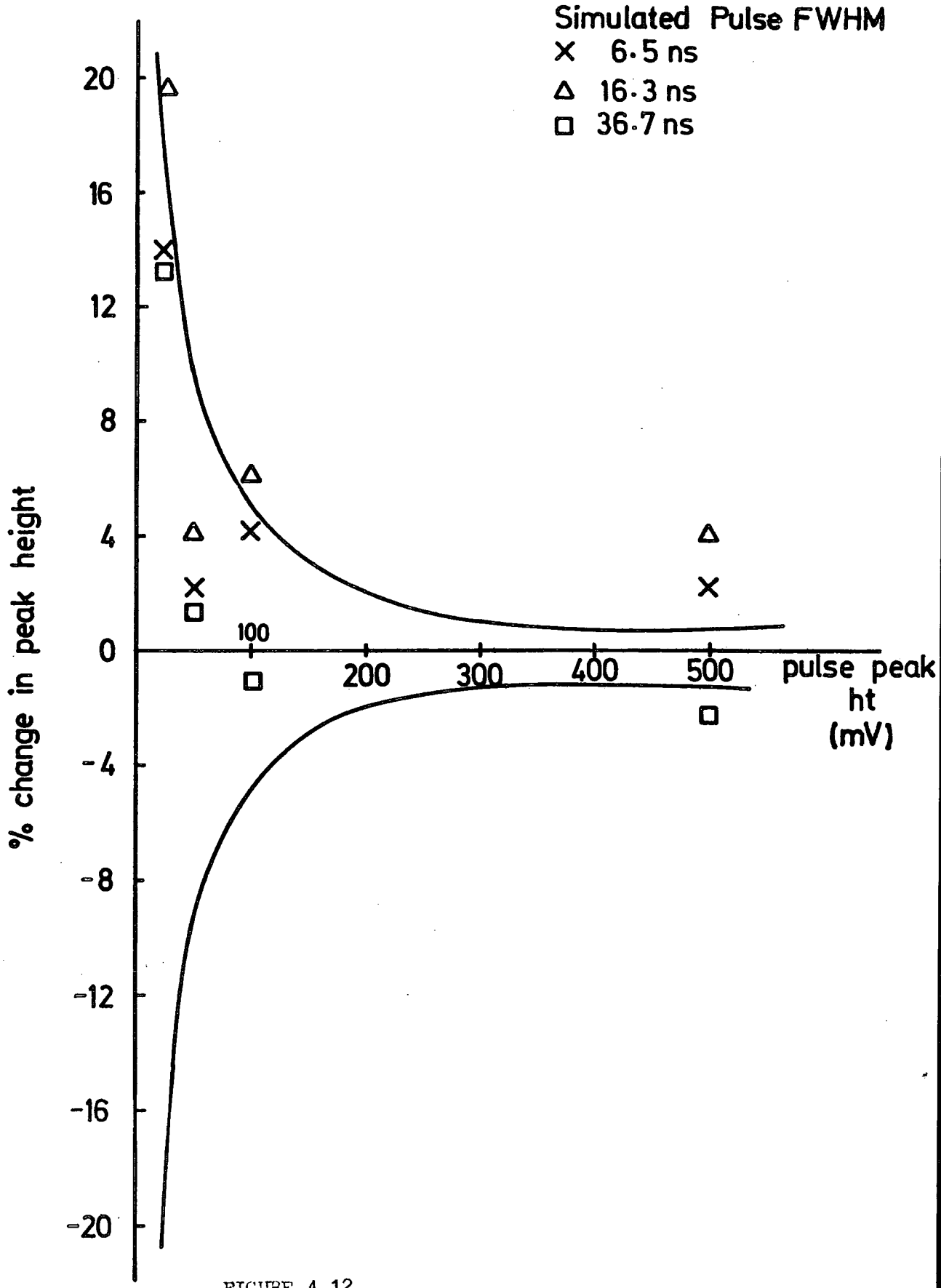

FIGURE 4.12

VARIATION OF % CHANGE IN PEAK HEIGHT WITH PEAK HEIGHT OF SPLINE-FITTED, NOISY SIMULATED PULSES.

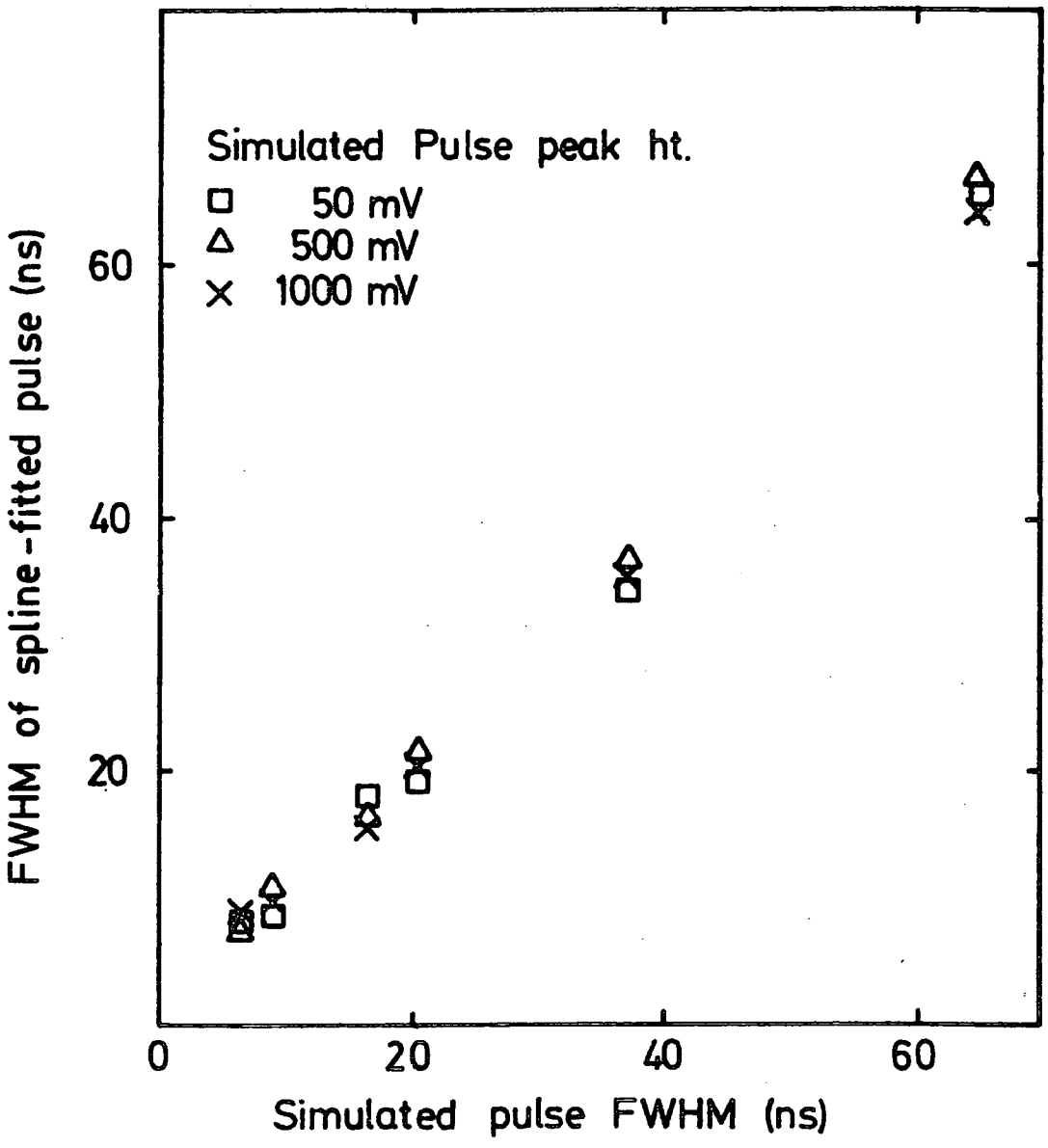

FIGURE 4.13

FWHM OF SPLINE-FITTED PULSE COMPARED WITH THE INPUT SIMULATED PULSE FWHM

TABLE 4.3

COMPARISON BETWEEN INPUT SIMULATED PULSE FWHM AND THE OUTPUT SPLINE FIT FOR NOISE-FREE PULSES. Error in FWHM = (simulation - spline fit)

Peak height of input simulated pulse (mV) \ FWHM of input simulated pulse (ns)	6.5	8.9	16.3	20.4	36.7	65.0
25	-1.0	-1.1	-1.7	-1.3	-0.3	+1.4
35	-1.5	+0.7	-1.0	+1.1	-0.8	-1.6
50	-2.0	+0.1	-1.3	+0.9	+1.2	+0.8
100	-0.5	-0.9	-1.8	-1.1	+1.8	-1.2
500	-2.1	-1.8	-0.2	-0.8	+1.1	-1.4
1000	-1.6	-1.2	+0.3	-1.0	+1.0	+1.3

TABLE 4.4

COMPARISON BETWEEN INPUT SIMULATION PULSE RISE TIME AND THE SPLINE FIT FOR NOISE-FREE PULSES. Error in Rise Time = (simulation - spline fit)

FWHM of input simulated pulse (ns)

peak height of input simulated pulse (mV)	6.5	8.9	16.3	20.4	36.7	65.0
25	+4.7	+3.8	+1.7	+3.4	-4.7	+2.8
35	+2.6	+3.4	+1.4	+1.7	-1.8	+2.4
50	+2.1	+1.8	+1.5	-1.6	+0.5	-1.0
100	-2.4	+0.9	-0.6	+1.9	-0.2	-1.3
500	+1.0	+1.1	-0.6	+0.2	-0.4	-0.9
1000	+0.4	+0.8	-0.7	+0.3	-0.4	-0.6
Rise Time of input pulse	8.3 ns	8.5 ns	6.5 ns	7.5 ns	9.7 ns	22.6 ns

TABLE 4.5

COMPARISON BETWEEN INPUT SIMULATED PULSE FWHM AND THE OUTPUT SPLINE FIT FOR NOISY PULSES. Error in FWHM = (simulation - spline fit)

peak height of input simulated pulse (mV) \ FWHM of input simulated pulse (ns)	6.5	8.9	16.3	20.4	36.7	65.0
25	-8.1	-5.1	+4.4	+5.8	+2.0	+4.6
35	-4.8	-5.0	+2.8	+3.3	+2.1	+4.1
50	-3.8	-2.9	+4.4	+2.6	+0.2	+2.8
100	-2.4	-2.2	-1.4	+2.1	+4.6	+1.6
500	+1.2	+1.9	-1.2	+1.7	+2.1	+1.2
1000	+1.1	+0.7	-1.5	+1.0	+0.9	+0.8

TABLE 4.6

COMPARISON BETWEEN INPUT SIMULATED PULSE RISE TIME AND THE OUTPUT SPLINE FIT FOR NOISY PULSES. Error in Rise Time = (simulation - spline fit)

peak height of input simulated (mV) \ FWHM of input simulated pulse (ns)	6.5	8.9	16.3	20.4	36.7	65.0
25	+5.3	+4.9	-3.8	+5.1	-4.7	+4.6
35	+2.8	+3.8	-3.5	+4.1	-4.6	+3.9
50	+2.5	+2.2	-1.4	-2.0	-6.5	+1.9
100	+0.5	+2.7	-2.8	-3.0	-2.9	+2.6
500	+3.7	+0.9	-1.6	-0.8	-0.7	+2.0
1000	+1.4	+1.3	-0.8	-0.7	-1.0	+0.8
Rise Time of input pulse	8.3 ns	8.5 ns	6.5 ns	7.5 ns	9.7 ns	22.6 ns

are the combination of random sky noise and systematic error due to spline-fitting.

The pulse shape parameter whose determination from spline-fits resulted in the biggest errors is Rise Time, as Tables 4.4 and 4.6 show. The errors in Rise Time increased systematically with a decrease in Peak Height (Figure 4.14). For small pulses, the discrimination level is near the peak. Any loss of information due to sampling at the leading edge will position the discrimination level further into the pulse. This can lead to a poor fit, as the spline is constrained to pass through the discrimination level.

Overall errors in the fit could also be due to the inability of the minimization package, MINUIT, to attain a unique minimum.

4.6 Conclusion.

These results indicate that spline-fitting is adequate for reconstruction of digitised Cerenkov light pulses. The peak height, Rise Time, and FWHM are all determined accurately from the fitting procedure. T10% is the least accurately evaluated percentage point. This is attributed to the slicing of the pulses.

The results on spline-fits of simulated pulses justify the use of quartic splines to reconstruct the Dugway data. The pulse shape characteristics determined from spline-fits are given in the following Chapters, with the necessary corrections made to them to account for reconstruction errors.

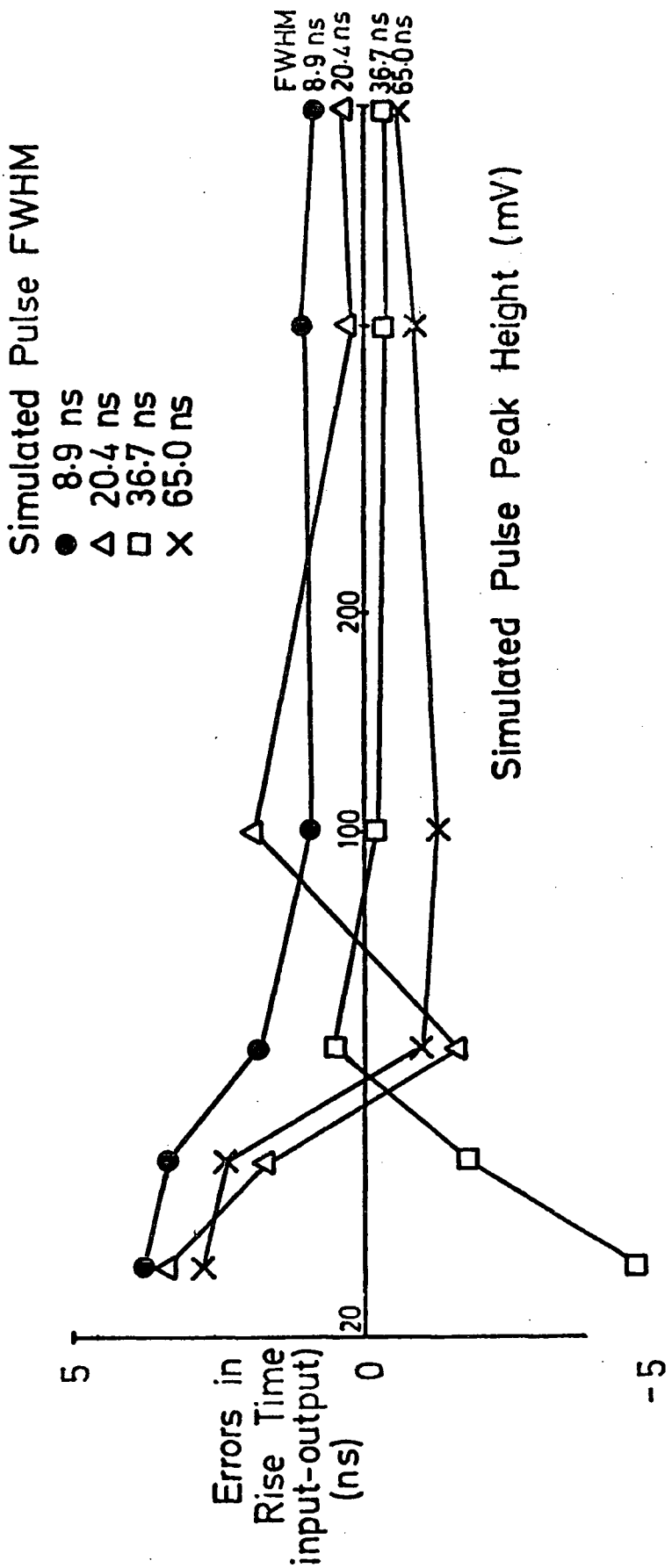

FIGURE 4.14

VARIATION OF ERRORS IN RISE TIME WITH PEAK HEIGHT.

(SPLINE FITTED SIMULATED PULSES)

CHAPTER FIVE

DATA REDUCTION AND ANALYSIS.

5.1 Overview.

This Chapter is concerned with the detailed analysis of the EAS data from Dugway, from the initial handling of the raw data to the extraction of pulse shape information using a suite of computer programs and the pulse shape reconstruction procedures outlined in Sections 4.4 and 4.5.

The observed average characteristics of the extensive air showers are outlined. The pulse shape parameters (FWHM, Rise Time, Fall Time and Top Time) are determined and their lateral distributions are shown. The lateral distribution of the Peak Height is also shown.

5.2 First Stage of the Analysis.

The first attempt to understand the data, after they were brought to Durham, involved a thorough study of the environmental conditions as outlined in Sections 3.4 and 3.5.

After the weather conditions had been quantified for the period of observation the data were divided into "data blocks", with each block consisting of at most 1 night's record and up to $\sim$ 200 events per block. Thus, whereas data from one night from the 400m array would make up not more than 2 data blocks, a typical clear night's record from the 100m array (with count rate $>$ 100 events per hour) was divided into up to 7 data blocks. This was necessary in order to concentrate resources on

the analysis of only the data from good weather nights. A total of 62 prime weather data blocks was obtained for the 400m array data, from the Winter 1978/79 and 1979/80 runs; 29 data blocks were obtained from the 200m array and the data from the 100m array were divided into 21 data blocks.

The data were then analysed by data block using a computer program to generate the following details :-

(1) the event rate per data block,

(2) the frequency of n-fold coincidences, where $3 \leq n \leq 8$,

(3) the individual detector response rates,

(4) the average pedestal values for all digitised quantities,

(5) a triggering profile to indicate the variation of the array trigger rate with changes in sky clarity,

and (6) histograms for each measured EAS parameter for each triggering detector.

Atmospheric monitoring information, which was logged at the central recording site at the time of each event, was also analysed at this stage. This included :-

(1) the pressure profile for the data block,

and (2) a graph of the night sky brightness as measured by the 2-inch photo-tube.

This additional atmospheric monitoring information and the triggering profile were valuable for cross-checking the quantitative weather records obtained from the star trail pictures.

5.3 Second Stage of the Analysis.

5.3.1 Decalibration and Overflowing.

The next stage of the analysis involved the decalibration of the data, after checking the raw data for errors in each detector's response.

The raw data were decalibrated by the use of computer programs and the calibration constants recorded from Dugway. The Cerenkov light pulse area was determined from either the area covered by the decalibrated digitised slices (which is designated here as 'Sigma Slices', ΣSL), or the pulse area recorded by the integrator. In this case, 'Sigma Slices' was not merely the total sum of all the slices. Each slice of width 10ns and given height was taken into account, and allowance was made for the overlap of slices as well as the tail end of the pulse where the slices were not as close together as at the leading edge (See Figure 3.4). The two measures of the pulse area helped to check the response of the integrator and the sequential charge digitising units.

The charge digitisers used at Dugway had an input voltage range greater than what our required resolution specified. We required the dynamic range of the slices to be 50 - 1500 mVns and for the integrator to be 250 - 100,000 mVns. The scalers used, with a dynamic range of 0 - 255 bits, could only give us a sensitivity of 60 mVns per bit if they were used to digitise the complete dynamic range of the system.

To correct this mismatch, and extend the dynamic range of the digitisers, two options were possible. One was to match the ADC maximum to PMT/amplifier maximum and have a digitised output reading of 4 mV per bit. The second option, and the one chosen in this work, was to match

the ADC maximum to half of the PMT/amplifier maximum. This resulted in a digitised output reading of 2 mV per bit and therefore some pulses (especially large pulses near the shower core) would register extra bits and 'overflow' the bit counter in the ADC. These 'overflows' were evident in the decalibrated data as a difference between the integrator reading and the summation of slices, and were allowed for in the following way.

The integrator response was compared with the summation of slices for each detector. If the integrator record was greater than Sigma Slices by more than 4000 mVns, slices 1, 2, or 3 was 'overflowed' by adding 4000 - 5000 mVns to the areas (and distributing the addition evenly on the slices) to make the two measures of pulse area nearly equal. To maintain a uniform pattern of overflows for all detectors, the total number of overflows was restricted to less than 4. Any detector that required more than 3 overflows was flagged and thrown out of the analysis.

In the final data selection for pulse shape analysis, 'overflowed' pulses were left out. This point is taken up further in Section 5.6. The design of the experiment allowed for the slices to overflow long before the integrator. This ensured that the pulse area was well measured.

5.3.2 Estimation of the Shower Core Position and Arrival Direction.

After decalibration, each event was analysed to establish the arrival direction and core location. Shearer (1980) has developed computer programs for this purpose using the non-linear least squares optimisation package, MINUIT, by James and Roos (1975).

Firstly, the computer program fitted a sphere through the detector triggering times, i.e. the time at which a threshold voltage of 20mV was registered by each detector. The line joining the array centre to the centre of this sphere gave the arrival direction for the shower. The choice of a spherical front fit rested in the work of Orford and Turver (1976) who showed that the fronts defined by various percentage levels through a Cerenkov light pulse were closely spherical. These authors quoted an RMS error of 3ns for a non-linear least squares fit to spherical fronts of radius $\sim 2 \times 10^4$ ns (or ~ 7 km) at the 10% points of the pulses observed by the Haverah Park array of eight detectors.

The location of the centre of the sphere defined by the least squares fit to the detector triggering times was used to estimate the depth into the atmosphere at which the shower reached the 20 mV level. Typically, the RMS deviation on the least squares fit to a sphere at the 20mV level was 1.61 ns for a radius of 3 km for a 5-fold coincidence.

Secondly, the shower core was determined by establishing the centre of symmetry of the Cerenkov light at ground level in the plane of the shower. Here, the availability of the two separate measures of the pulse area proved useful. Sigma Slices was used for small pulses (< 5000 mVns) when this summation was the more accurate measure, and the integrator record was used for bigger pulses.

With the shower core and arrival direction established, initial studies could be made of the extensive air shower parameters which show variations with core distance and zenith angle.

To determine the variation of optical photon density with core distance, a function of the form :

$$\phi(r) = A(r + r_0)^{-\eta} \qquad 5.1$$

was used, where :-

$\phi(r)$ is the photon density at core distance, r ;

A is a constant unique to each shower ;

and r_0 was fixed at 50 metres.

Thus, at this stage in the analysis, each shower had a value of η which indicated the distribution of the Cerenkov light with radial distance and zenith angle.

5.4 Criteria for Final Analysis.

At the end of the day, an event that was acceptable for final analysis had to satisfy the following criteria :

(1) The weather code must indicate prime weather conditions ;

(2) All overflows should be implemented or pulses which could not be overflowed should be flagged ;

(3) All decalibration parameters must be given a final check;

and (4) The RMS deviation on the arrival direction must be < 10ns and on the core location < 1500 mVns.

All events satisfying these criteria were stored on disc or magnetic tape in a particular format to allow for easy access during the next stage of the analysis which involved a great deal of computation, including :-

(1) The reconstruction of the Cerenkov light pulse shape from the decalibrated slices ;

(2) A refinement of the lateral distribution of the optical photon density ;

(3) A refinement of the time of arrival and shower imaging ;

(4) The arrival directions of the extensive air showers ;

and (5) The separation between the light front and particle front of the Cerenkov radiation.

5.5 Primary Energy Estimators at Dugway.

Computer simulations of air showers have been used to predict primary energy estimators for the Dugway array. Any primary energy estimator must be a parameter measurable at all energies and shower sizes and showing little or no variation with energy, zenith angle and photon flux over the range of shower energies and zenith angles for the array. This quantity can be either the optical photon density at a given core distance, $\phi(r)$, or some other measure of the shower characteristics.

Initially, two measures of the primary energy were evaluated for the 400m array, viz :

(1) the optical photon density at 200m from the shower core, $\phi(200m)$;

and (2) the integral of the lateral distribution between 50m and 250m, C_{50}^{250}.

$\phi(200m)$ and C_{50}^{250} were proposed as primary energy estimators on the basis of the array boundary requirements and the results of computer simulations available at that time. Initial samples of the Dugway EAS data have been analysed and interpreted on the basis of these two primary energy estimators by Andam et al (1979), Chantler et al (1979), and Shearer (1980). However, further computer simulation results have been

obtained, providing better primary energy estimators for all three arrays operated at Dugway.

McComb and Turver (1981) have observed that the simulation optical photon density depends not only on primary energy, but also to some extent on the depth of electron cascade maximum, at all core distances (Figure 5.1). However, for a fixed energy shower at $< 45^{o}$, with depth of maximum 550 - 850 gcm^{-2}, their results show that the photon density at 150m from the core, $\phi(150m)$, varies only slightly with depth of maximum (< 10% change for 100 gcm^{-2} change). The optical photon density which changes least with depth of maximum for low energy showers (10^{15} - 10^{16} eV) maximising at $< 500\ gcm^{-2}$, was found to be $\phi(500m)$.

The two Dugway EAS arrays for observation of large showers (10^{16} - 10^{18} eV) were of radius 200m and 400m, and for these arrays $\phi(150m)$ was readily measurable as an energy estimator. For low energy showers, (10^{15} - 10^{16} eV), the maximum array dimension was 100m radius. Hence, $\phi(500m)$ could not be measured with such an array, and $\phi(100m)$ was chosen as a compromise.

5.6 The Data Set for this Work.

A sample of showers from the Dugway data was selected according to the primary energy estimator, $\phi(150m)$, for detailed analysis for this work. These consisted of 275 showers from the 200m array, incident at zenith angle 0^{o} - 60^{o} and 104 showers from the 400m array, incident at zenith angle 0^{o} - 45^{o}. The energy range for the 400m array data sample was $3.50 \leqslant \log(\phi(150m)) \leqslant 4.50$, a decade of energy which corresponded to 6.75×10^{16} eV $\lesssim E_p \lesssim 6.75 \times 10^{17}$ eV. The data from

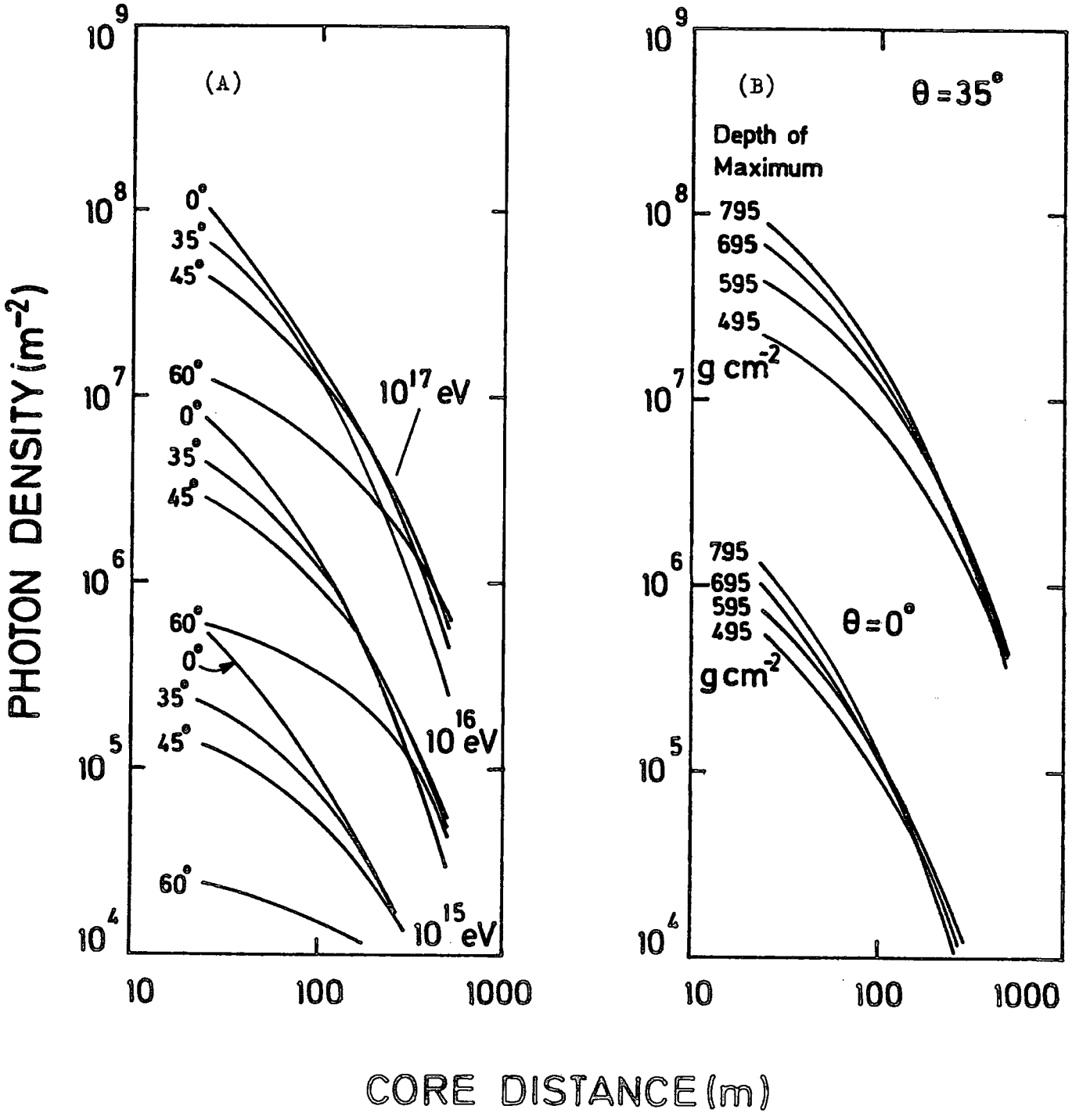

FIGURE 5.1

THE LATERAL DISTRIBUTION OF CERENKOV LIGHT AT (A) DIFFERENT ZENITH ANGLES, (B) DIFFERENT DEPTHS OF ELECTRON CASCADE MAXIMA.

(McComb and Turver, 1981)

the 200m array were for showers in the primary energy range $2.90 \leq \log(\emptyset(150m)) \leq 3.90$ or 1.80×10^{16} eV $\lesssim E_p \lesssim 1.80 \times 10^{17}$ eV.

Figures 5.2 and 5.3 show the zenith angle and energy distribution for the two data sets. Only events which registered 5-fold or more coincidences from nights of prime weather conditions were selected. The overlap in the energy range of the two data sets made it possible to cross-check any air shower parameters measured in the overlap, ($1.80 \times 10^{16} \lesssim E_p \lesssim 6.75 \times 10^{16}$ eV).

For the work presented in this Thesis, the five or more pulses in each shower were reconstructed by quartic spline fitting, as described in Chapter 4. Only pulses whose height was greater than the discrimination level for each detector were used for the pulse shape analysis. For very small pulses (< 40mV) most of the front edge would be lost to the digitising system, since sequential pulse digitisation started only after the detector discrimination level was reached.

A further criterion relating to pulse overflows (Section 5.3.1) was incorporated in the selection. Pulses with overflows were reconstructed merely to determine whether the integrator had also, itself, overflowed ; i.e. whether a pulse with overflowed slices became consistent after overflow, by checking that Sigma Slices was equal to the integrator record.

The special problems relating to quartic spline reconstruction of real pulses from our data, as opposed to simulated pulses used for testing the computer program, are explained below.

FIGURE 5.2(a)

DISTRIBUTION OF $\log(\phi(150m))$ FOR THE 400metre ARRAY DATA SAMPLE, 6.75×10^{16} eV $\lessapprox$ E_p $\lessapprox$ 6.75×10^{17} eV

FIGURE 5.2(b)

DISTRIBUTION OF $\log(\phi(150m))$ FOR THE 200metre ARRAY DATA SAMPLE, 1.80×10^{16} eV $\lessapprox$ E_p $\lessapprox$ 1.80×10^{17} eV

Fig. 5.2(a)

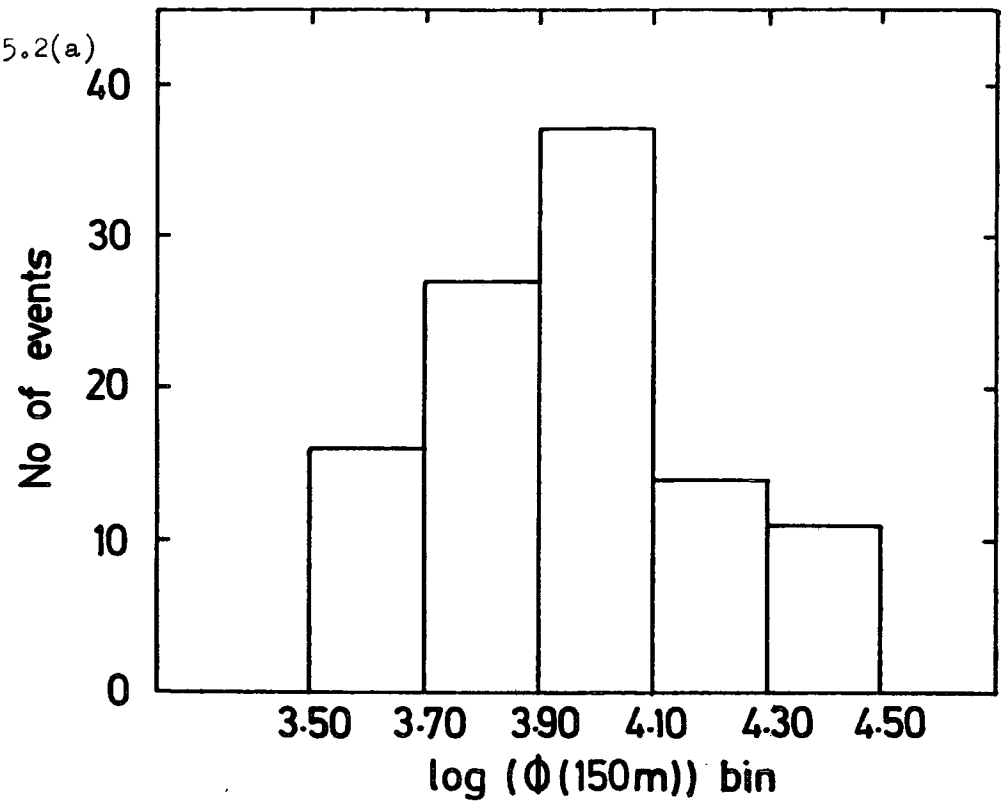

Fig. 5.2(b)

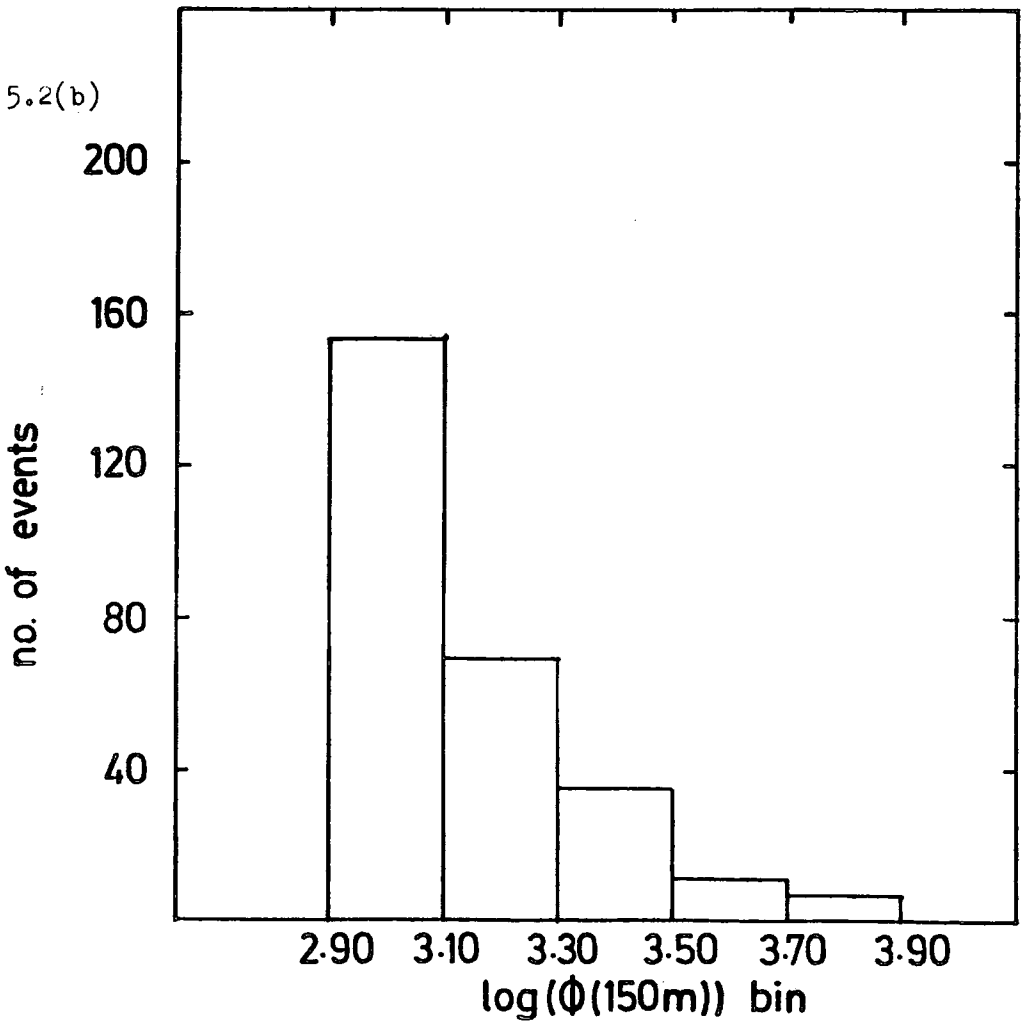

FIGURE 5.3(a)

DISTRIBUTION OF ZENITH ANGLE FOR THE 400metre ARRAY DATA SAMPLE, 6.75×10^{16} eV $\lesssim E_p \lesssim 6.75 \times 10^{17}$ eV

FIGURE 5.3(b)

DISTRIBUTION OF ZENITH ANGLE FOR THE 200metre ARRAY DATA SAMPLE, 1.80×10^{16} eV $\lesssim E_p \lesssim 1.80 \times 10^{17}$ eV

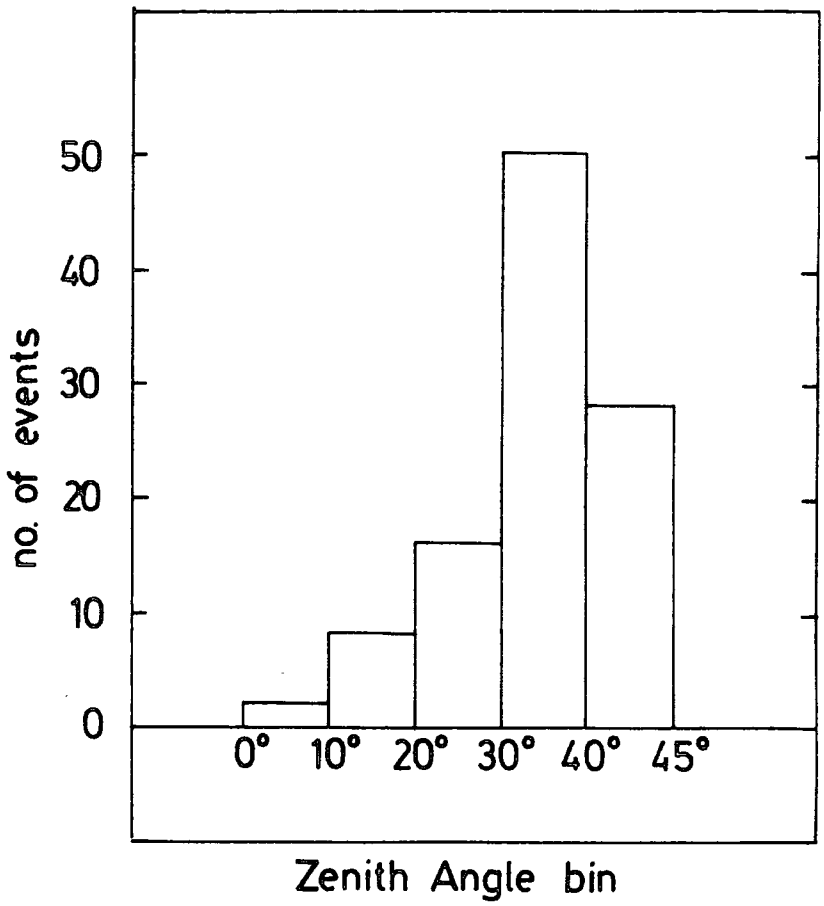
50
40
30
20
10
0
no. of events
0°
10°
20°
30°
40°
45°
Zenith Angle bin

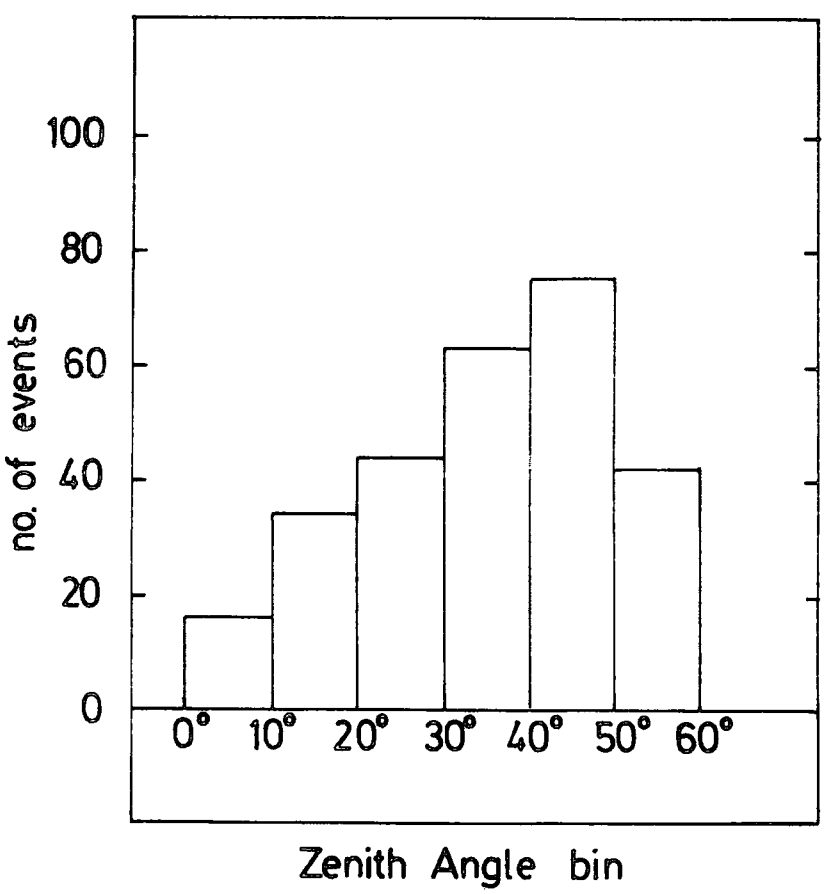
100
80
60
40
20
0
no. of events
0°
10°
20°
30°
40°
50°
60°
Zenith Angle bin

5.6.1 The Effect of System Bandwidth on Pulse Shape Reconstruction.

The response of all detectors were determined from radioactive pulser measurements at Dugway, (Shearer, 1980). Figures 5.4(a-h) illustrate the system response for the eight detectors. These show considerable variation in the shape and size of the undershoot on the individual detector output pulses.

The presence of undershoot on the data has some implications for pulse shape fitting which should not be overlooked. The unimodal quartic spline will tend to either make up for the undershoot, giving a reconstructed pulse that is too wide, or ignore the undershoot and result in a loss of the back edge of the pulse.

Most of the fits for bandwidth limited pulses (close to the shower core) were broader than expected. This could be a direct result of 'slicing' and was more evident for the 400m array data, since for these pulses the slices at the back edge were further apart than those at the leading edge, (See Figure 3.4).

In addition to system bandwidth effects, the position of the discrimination level was found to affect the fit. The quartic spline was constrained to fit through the discrimination level. Therefore, an accurate determination of the gain of each detector, which was used to estimate the discrimination level, was necessary.

With these special problems of pulse reconstruction in mind, the pulse shape parameters: FWHM, Rise Time, Top Time, and Fall Time have been computed and their average characteristics are listed in the following Sections.

FIGURE 5.4 (a-h)

SYSTEM RESPONSE FOR THE DETECTORS USED AT DUGWAY.

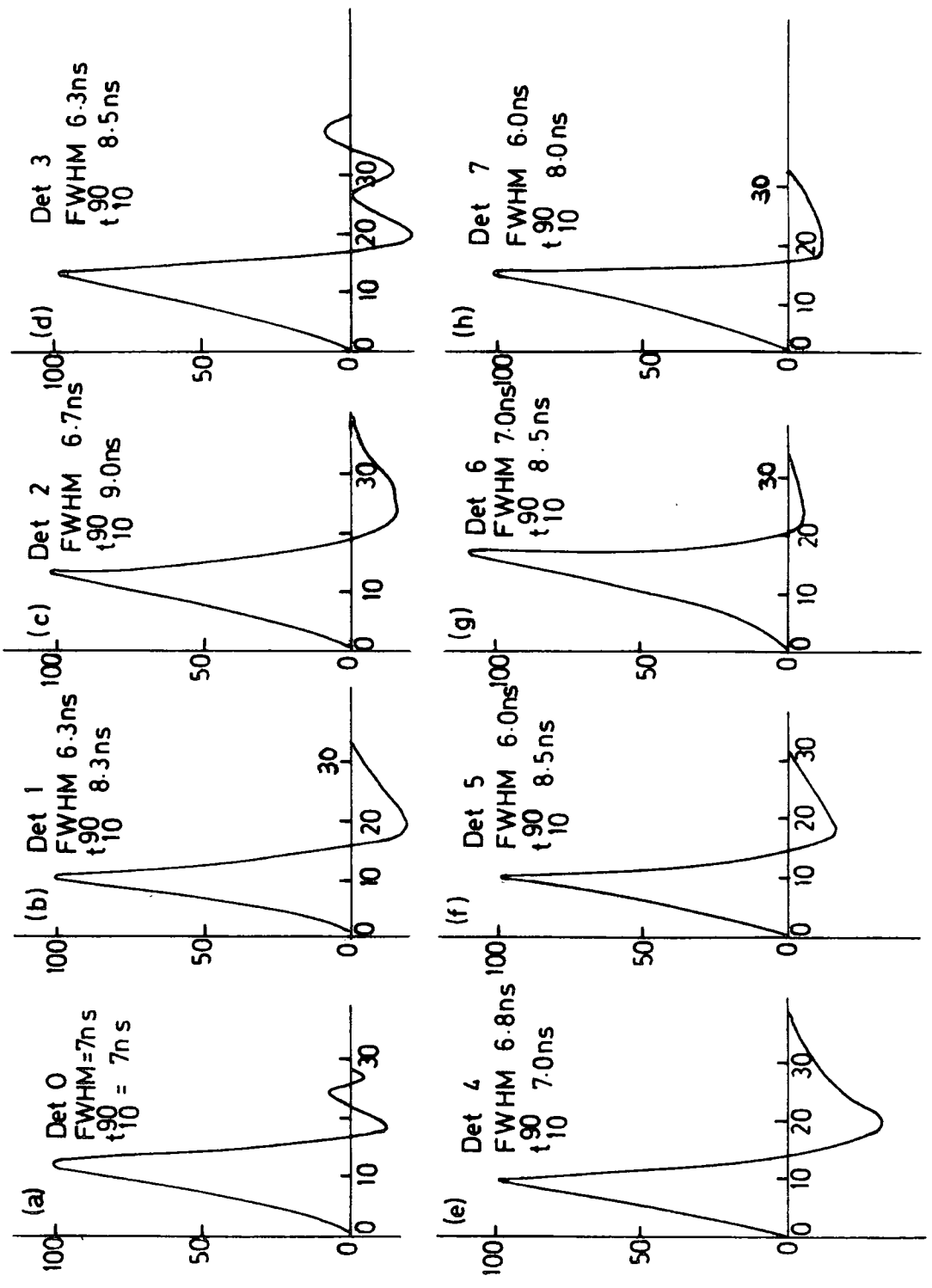
(a)
Det 0
FWHM=7ns
t90 = 7ns
10
(b)
Det 1
FWHM 6.3ns
t90 8.3ns
10
(c)
Det 2
FWHM 6.7ns
t90 9.0ns
10
(d)
Det 3
FWHM 6.3ns
t90 8.5ns
10
(e)
Det 4
FWHM 6.8ns
t90 7.0ns
10
(f)
Det 5
FWHM 6.0ns
t90 8.5ns
10
(g)
Det 6
FWHM 7.0ns
t90 8.5ns
10
(h)
Det 7
FWHM 6.0ns
t90 8.0ns
10
Pulse height (mV)
Time (ns)

5.7 Average Pulse Shape Characteristics from Dugway.

The average pulse shape characteristics measured at Dugway are given below for the two data sets analysed for this work.

The FWHM, Rise Time, Top Time and Fall Time are listed for the data from the 400m array ($\bar{E} = 1.7 \times 10^{17}$ eV), and their dependence on core distance and zenith angle are shown. The variation of FWHM with core distance and zenith angle for the 200m array data ($\bar{E} = 3 \times 10^{16}$ eV) is also given. Figures 5.5 - 5.10 illustrate the variation of the average pulse shape parameters with core distance and zenith angle, and indicate that the pulse shape parameters relate to core distance through a power law of the form :

$$\text{Parameter}(r) = a + br^n \qquad 5.2$$

where a and b are constants.

System bandwidth effects have been removed from the Rise Times and FWHM. This has been done by comparing the observed parameters with computer simulations especially tailored to the arrays and Dugway atmosphere, from the work of McComb and Turver (1981). Corrections have also been made for pulse shape reconstruction errors, using the results of quartic spline reconstruction of simulated pulses.

No attempt has been made to remove the system response from Top Time and Fall Time at this stage of the analysis. Further systematic theoretical studies will be required before any useful attempt at deconvolution may be made to these two pulse shape parameters.

5.7.1 The Full-Width-at-Half-Maximum.

The FWHM, shown in Figure 5.5 for the 400m array data and Figure 5.6 for the 200m array data, has been fitted with a power law (Equation 5.2) with $n = 2$, to quantify FWHM dependence on core distance. The values of a and b are listed in Table 5.1. The different values of a and b, obtained for different zenith angle bins, imply a FWHM dependence on zenith angle. There is an observed flattening of the FWHM curves with increase in zenith angle. This is more evident with low energy showers (200m array data, $\bar{E} = 3 \times 10^{16}$ eV) than with high energy showers (400m array data, $\bar{E} = 1.7 \times 10^{17}$ eV).

For the 200m array data, the FWHM was found to decrease between 50m and 100m and increase again from 100m to 200m. This broadening of pulses close to the shower core was more noticeable with highly inclined showers (45° - 60°, shown in Figure 5.6(e)) than with vertical showers.

5.7.2 Correlation of FWHM(300m) with Zenith Angle.

From the relationship :

$$FWHM(r) = a + br^2 \qquad 5.3$$

the FWHM at 300m from the core, FWHM(300m), has been derived. FWHM(300m) was calculated for 90 showers with mean energy $\sim 1.7 \times 10^{17}$ eV. Each shower selected had at least one pulse at core distance $\geq$ 300m. This criterion ensured that the value of FWHM(300m) was obtained through interpolation.

FIGURE 5.5

VARIATION OF FWHM WITH CORE DISTANCE FOR THE 400m ARRAY DATA SAMPLE, (mean energy = 1.7×10^{17} eV)

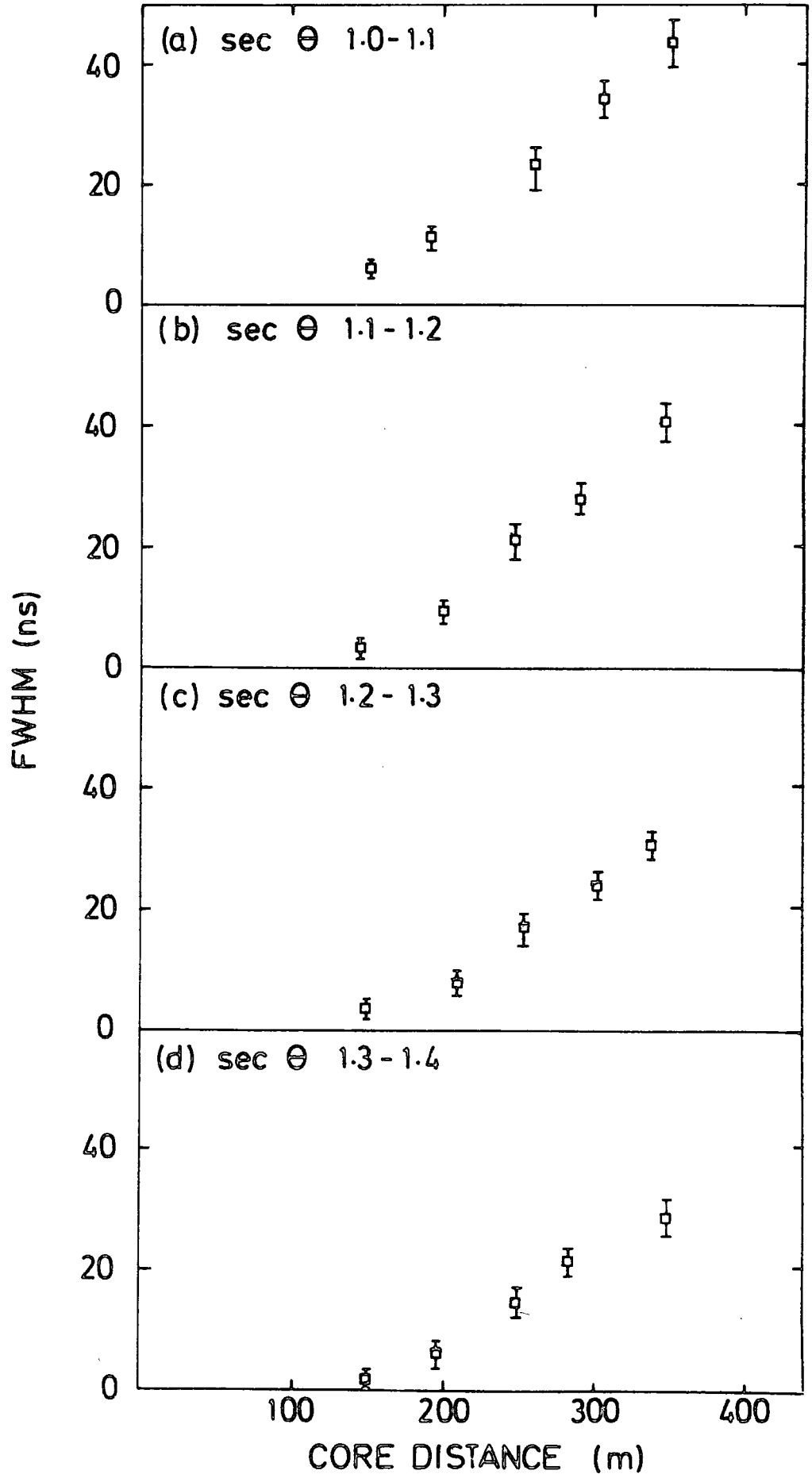
(a) sec θ 1·0-1·1
(b) sec θ 1·1-1·2
(c) sec θ 1·2-1·3
(d) sec θ 1·3-1·4
FWHM (ns)
0
20
40
100
200
300
400
CORE DISTANCE (m)

FIGURE 5.6

VARIATION OF FWHM WITH CORE DISTANCE FOR THE

200m ARRAY DATA SAMPLE (mean energy = 3×10^{16} eV)

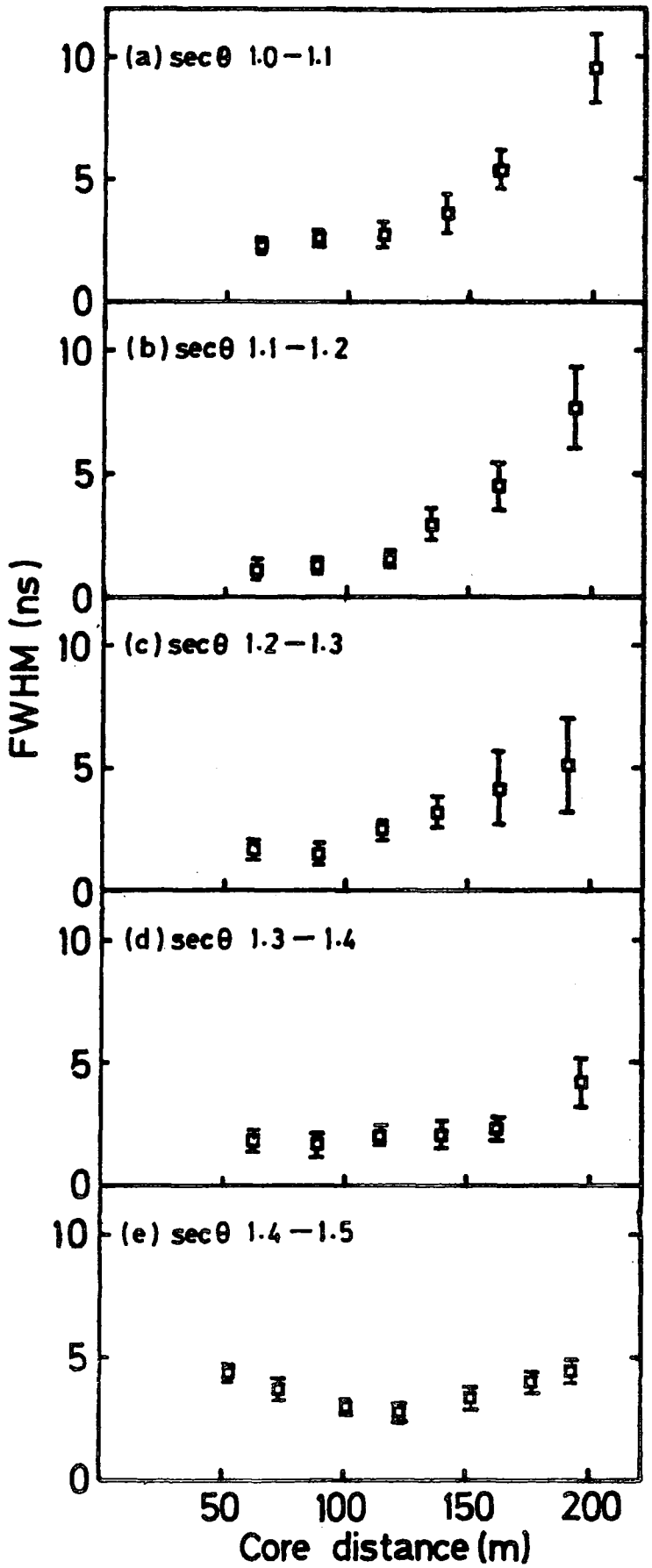
(a) sec θ 1.0 – 1.1
(b) sec θ 1.1 – 1.2
(c) sec θ 1.2 – 1.3
(d) sec θ 1.3 – 1.4
(e) sec θ 1.4 – 1.5
FWHM (ns)
0
5
10
50
100
150
200
Core distance (m)

TABLE 5.1

THE COEFFICIENTS OF THE EQUATION : FWHM(r) = a + br^2 fitted to

(i) the 400m array data sample ($\overline{E}$ = 1.7 x 10^{17} eV)

(ii) the 200m array data sample ($\overline{E}$ = 3 x 10^{16} eV)

(i)

secant θ bin	a	b
1.0 - 1.1	-2.709	0.00038
1.1 - 1.2	-4.845	0.00038
1.2 - 1.3	-4.446	0.00031
1.3 - 1.4	-3.318	0.00027

(ii)

secant θ bin	a	b
1.0 - 1.1	0.645	0.0002
1.1 - 1.2	1.013	0.00016
1.2 - 1.3	1.579	0.00008
1.3 - 1.4	1.377	0.00006

The 90 showers were divided into 4 energy bins :

(a) $3.50 < \log(\phi(150m)) \leq 3.75$

(b) $3.75 < \log(\phi(150m)) \leq 4.00$

(c) $4.00 < \log(\phi(150m)) \leq 4.25$

(d) $4.25 < \log(\phi(150m)) \leq 4.50$

The average FWHM(300m) variation with zenith angle is shown in Figure 5.7.

For all energy bins, FWHM(300m) is noted to decrease with increase in zenith angle, suggesting that the pulses become narrower with greater shower inclination. However, it should be noted from the curves for the 4 energy bins, and from the FWHM variation with core distance (Figure 5.5), that the FWHM does not depend on zenith angle alone. The FWHM dependence on zenith angle, core distance and primary energy are all inter-related.

5.7.3 Rise Time Measurements.

The Rise Times for the 400m array data ($\bar{E} = 1.7 \times 10^{17}$ eV) are shown in Figure 5.8 for the core distance range 200m - 400m. System bandwidth effect on Rise Time is more severe than on FWHM, particularly at core distances $\lesssim$ 250m. Hence, very careful deconvolution of the observed Rise Times is required.

Table 5.2 gives a list of the values of a and b obtained by fitting the Rise Times to Equation 5.2 with $n = 1.5$. The value of 1.5 was estimated from least squares fits to the data points. A dependence of Rise Time on zenith angle is shown from the values of a and b, although this dependence may be more complicated than the FWHM variation with zenith angle.

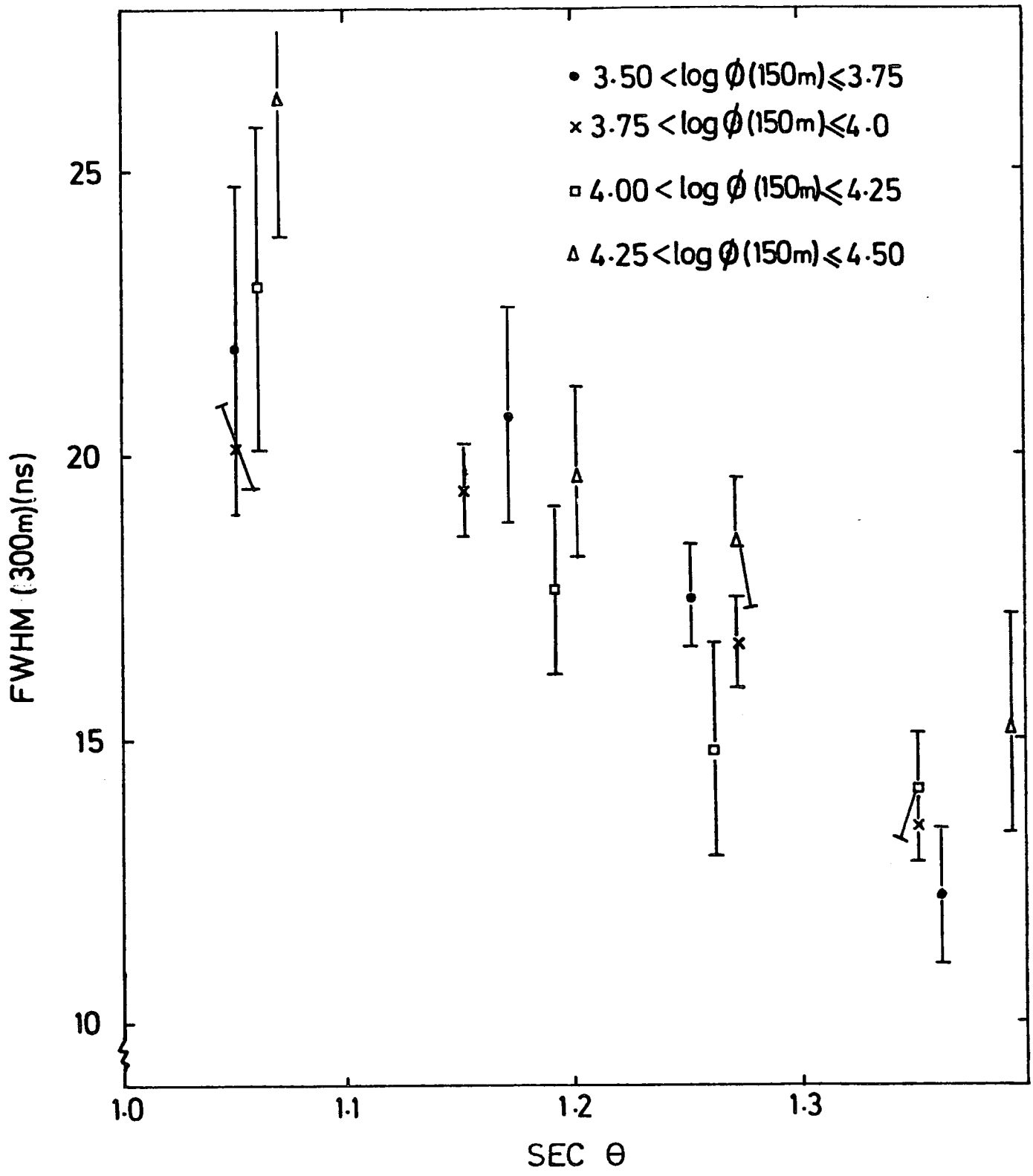

FIGURE 5.7

FWHM(300m) DEPENDENCE ON ZENITH ANGLE FOR 4 ENERGY BINS.

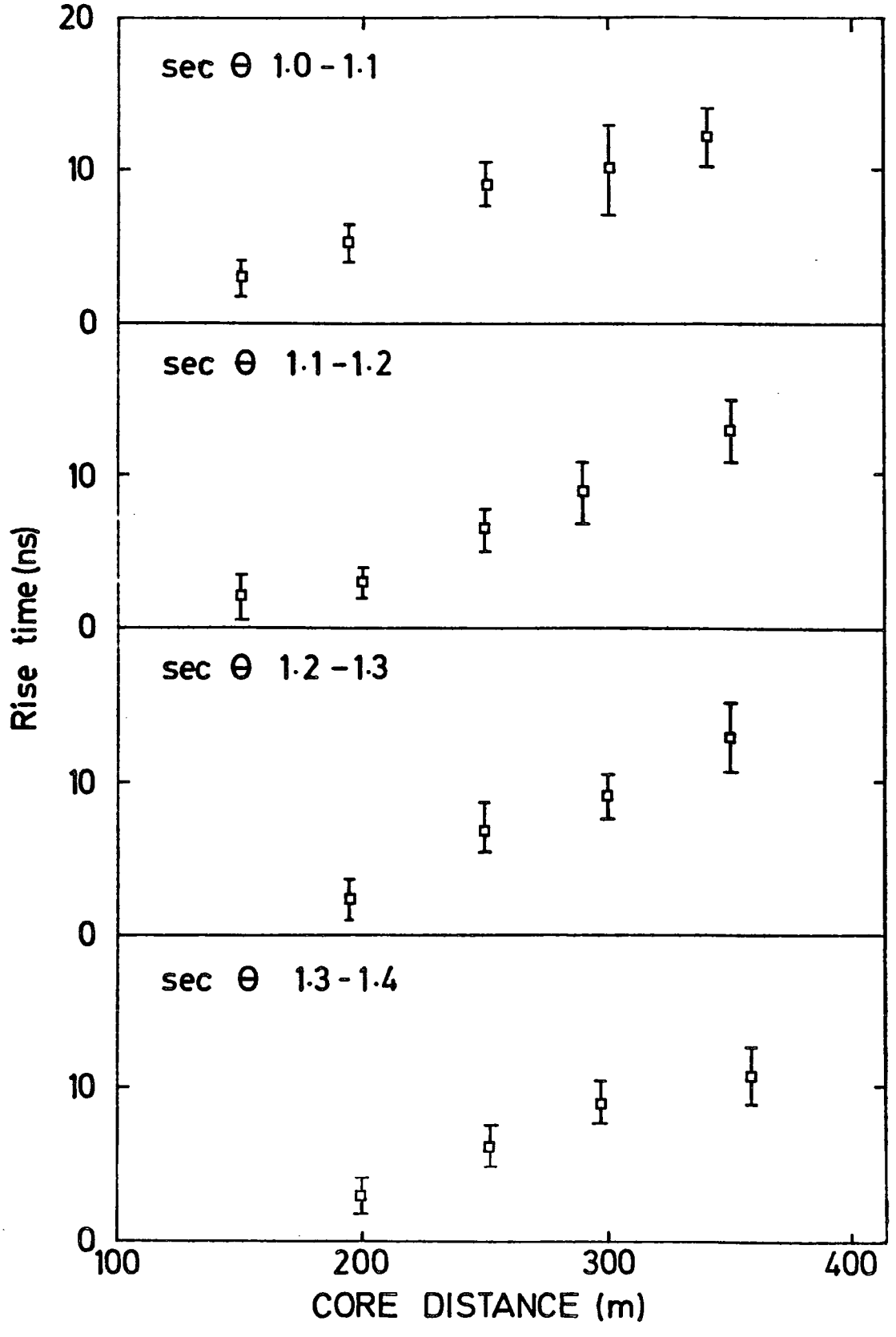

FIGURE 5.8

VARIATION OF RISE TIME WITH CORE DISTANCE FOR THE 400m ARRAY DATA,

(mean energy = 1.7×10^{17} eV)

TABLE 5.2

THE COEFFICIENTS OF THE EQUATION : Rise Time(r) = $a + br^{1.5}$

FITTED TO THE 400m ARRAY DATA SAMPLE, (mean energy = 1.7×10^{17} eV)

secant θ bin	a	b
1.0 - 1.1	0.605	0.002
1.1 - 1.2	-2.707	0.0024
1.2 - 1.3	-3.151	0.0025
1.3 - 1.4	-2.256	0.0019

5.7.4 Top Time and Fall Time Measurements.

The average Top Time and Fall Time for the 400m array data ($\bar{E}$ = 1.7 x 10^{17} eV) are shown in Figure 5.9 and 5.10. From least squares fits to the data points, the value of n in Equation 5.2 was found to be 1.5 for Top Time and Fall Time. The values of a and b from the power law dependence of Top Time on core distance are listed in Table 5.3. Similar values of a and b for Fall Time are listed in Table 5.4. The lateral distributions of both Top Time and Fall Time were observed to flatten with increase in zenith angle.

5.8 The Peak Height of Cerenkov Light Observed at Dugway.

The lateral distributions of peak height are shown in Figure 5.11 for 4 zenith angle bins. The data are from a sample of showers with mean energy 1.7 x 10^{17} eV. The lateral distributions indicate a variation of peak height with core distance, r , of the form :

$$\text{Height}(r) = A(r + r_o)^{\delta} \qquad 5.4$$

where A is a constant, and r_o is fixed at a given core distance.

5.9 Other Cerenkov Light Characteristics Measured at Dugway.

The Dugway experiment was performed to measure not only pulse shape characteristics, but also the optical photon density, the arrival direction of the shower and the time delay between the Cerenkov light and the particles.

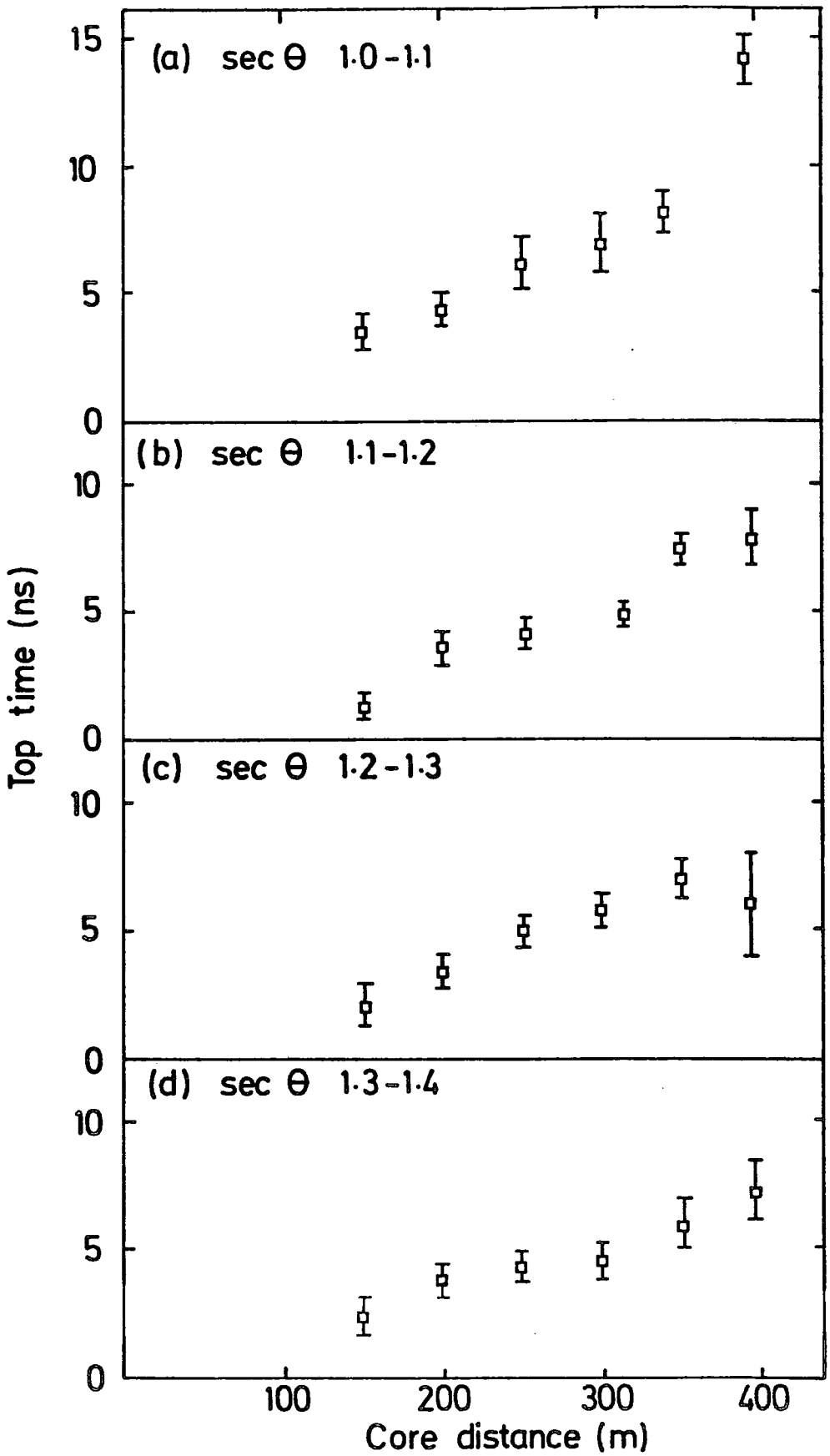

FIGURE 5.9

VARIATION OF TOP TIME WITH CORE DISTANCE FOR THE 400m ARRAY DATA SAMPLE (mean energy = 1.7×10^{17} eV)

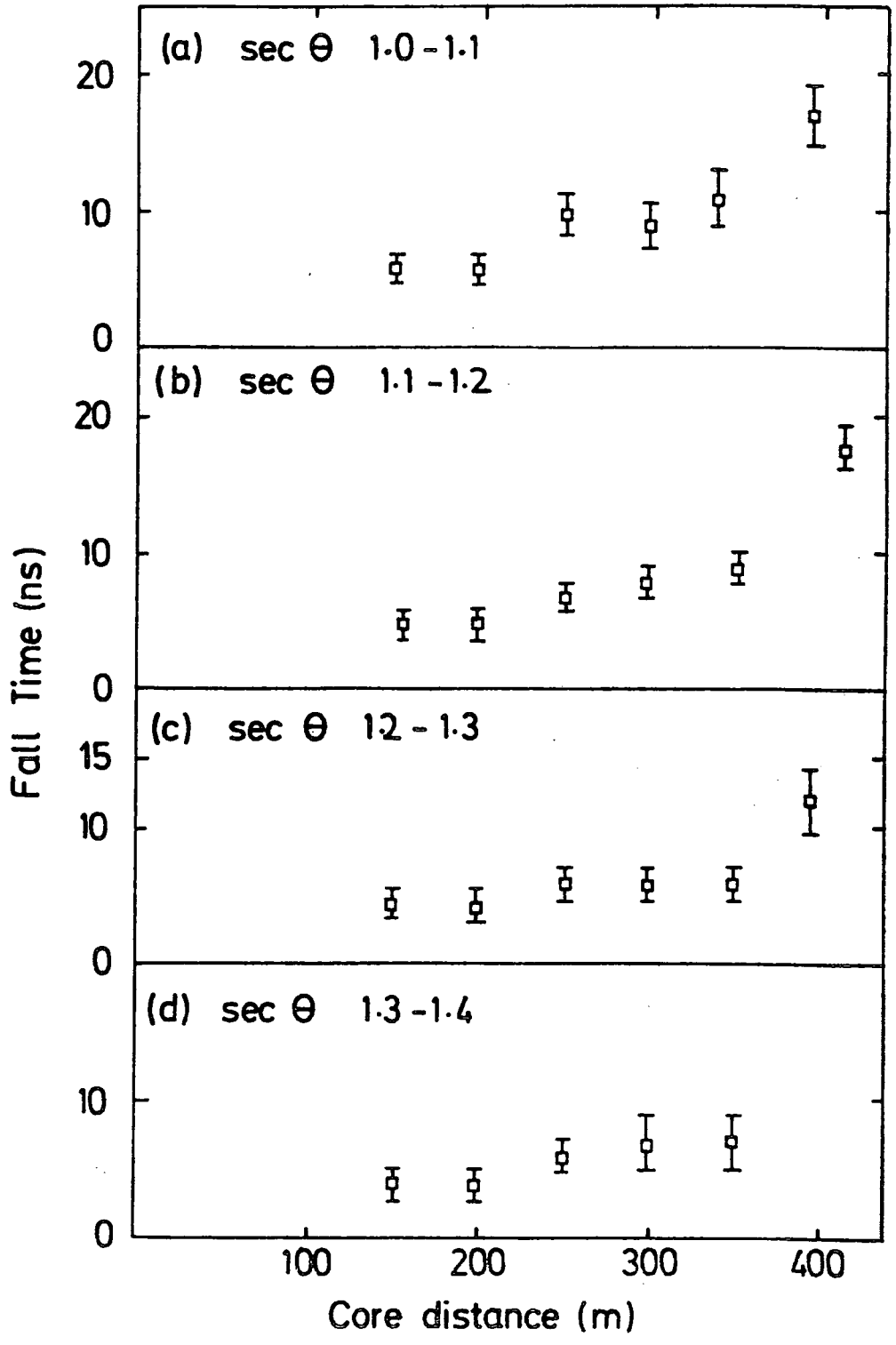

FIGURE 5.10

VARIATION OF FALL TIME WITH CORE DISTANCE FOR THE 400m ARRAY DATA SAMPLE (mean energy = 1.7×10^{17} eV)

TABLE 5.3

THE COEFFICIENTS OF THE EQUATION : Top Time(r) = a + $br^{1.5}$

FITTED TO THE 400m ARRAY DATA (mean energy = 1.7 x 10^{17} eV)

TABLE 5.4

THE COEFFICIENTS OF THE EQUATION : Fall Time(r) = a + $br^{1.5}$

FITTED TO THE 400m ARRAY DATA SAMPLE,

(mean energy = 1.7 x 10^{17} eV)

TOP TIME

secant θ bin	a	b
1.0 - 1.1	-1.297	0.0017
1.1 - 1.2	-0.27	0.0011
1.2 - 1.3	0.77	0.0008
1.3 - 1.4	1.36	0.0009

FALL TIME

secant θ bin	a	b
1.0 - 1.1	1.120	0.0021
1.1 - 1.2	-0.417	0.0019
1.2 - 1.3	1.110	0.0012
1.3 - 1.4	-2.765	0.0025

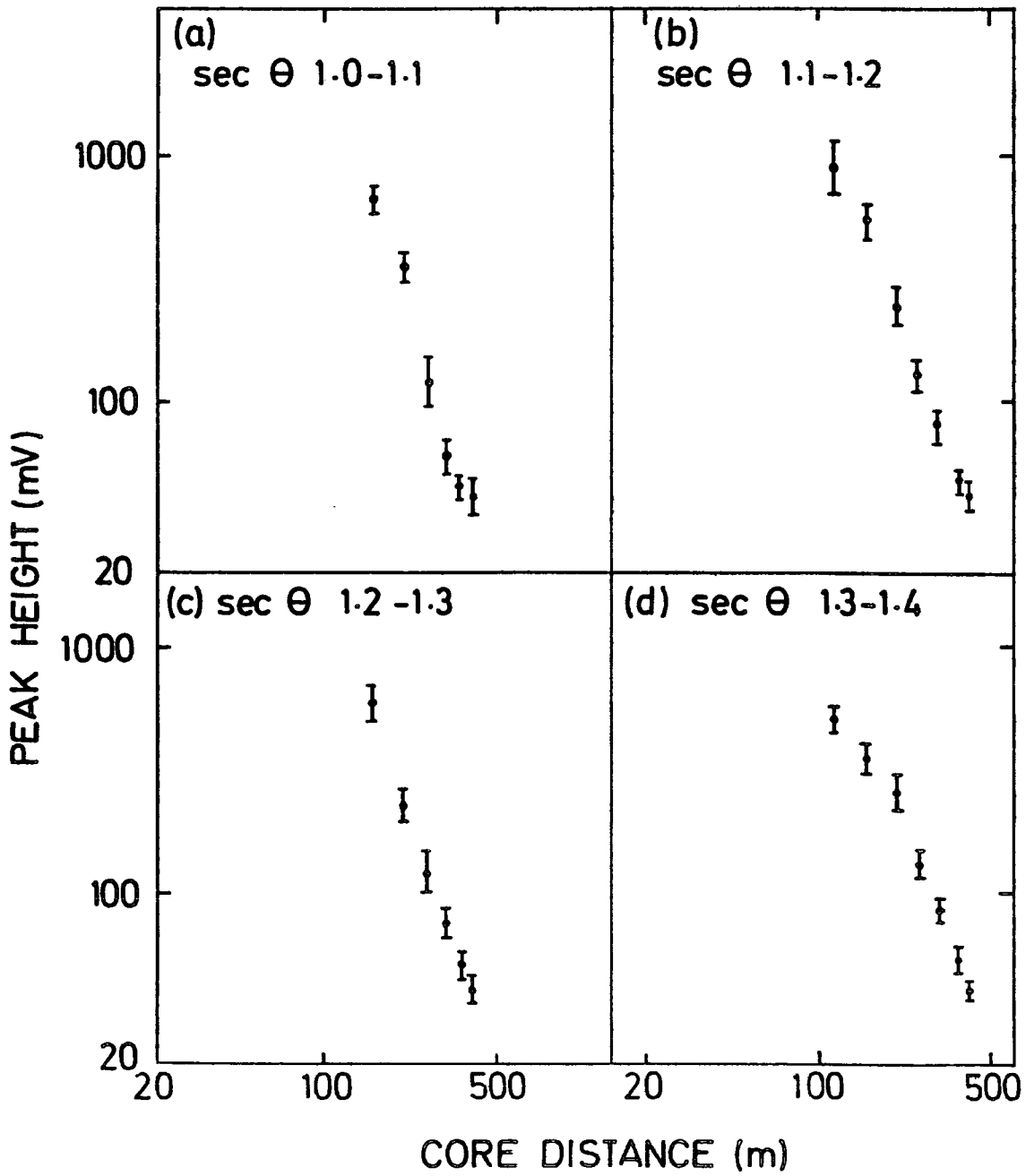

FIGURE 5.11

VARIATION OF PEAK HEIGHT WITH CORE DISTANCE - DUGWAY DATA

(mean energy = 1.7×10^{17} eV)

Since the Cerenkov light measurements were made with an array of several detectors, accurate shower cores could be determined for each shower. This has led to the calculation of shower arrival directions, (Craig et al, 1981).

Measurements of the curvature of the light front have been carried out in parallel with the determination of pulse shape characteristics, (Andam et al, 1981) and will be reported by Chantler in detail (Ph.D. Thesis, in preparation).

The analysis on the Cerenkov light front curvature was based on the philosophy of the pioneer work of Orford and Turver (1976). The percentage levels of the light pulse, calculated after quartic spline reconstruction, have been used to compute the front curvature of the light. Such computation leads to the derivation of depths of electron cascade maxima for the extensive air showers.

The lateral distribution of the Cerenkov light has been investigated in detail at Durham. A preliminary report by Andam et al (1979) has been followed by further results from the work of Chantler et al (1981). The choice of primary energy estimator for these two reports was influenced, each time, by prevailing computer simulations. Andam et al (1979) used $\phi(200m)$ as a primary energy estimator for their sample of showers from the 400m array. Chantler et al (1981) have used three sets of data samples from the 400m, 200m and 100m arrays, with the primary energy estimator $\phi(150m)$ used for the 400m and 200m arrays and $\phi(100m)$ for the 100m array.

The shape of the Cerenkov light lateral distribution has been represented by a function of the form :

$$\phi(r) = A(r + r_o)^{-\eta} \qquad 5.5$$

with r_o fixed at 50m.

The results presented by Andam et al (1979) were based on the values of the structure function exponent, η, over the core distance range covered by their sample. In attempting to interprete the data from all three arrays, Chantler et al (1981) observed that the fitted value of η exhibited systematic changes as a result of the varying core distance distributions of the responding detectors. Therefore, these authors have adopted a new Cerenkov light lateral distribution parameter defined as the ratio :

$$R(r_1, r_2) = \frac{\phi(r_1)}{\phi(r_2)} \qquad 5.6$$

where $\phi(r_1)$ and $\phi(r_2)$ are the optical photon densities at core distances r_1 and r_2 which are defined by the particular array geometry under study. The different values of r_1 and r_2 for the three arrays are listed in Table 5.5.

The calculated values of $R(r_1, r_2)$ have been used to derive depths of electron cascade maxima for samples of showers from Dugway. In Chapter 6, these derived depths of maxima from lateral distribution will be compared with the depths of maxima derived in this work from pulse shape parameters.

The time delay between the Cerenkov light and the particle front has also been studied systematically by the Durham Group. A preliminary report was made by Chantler et al (1979) and further measurements have

TABLE 5.5

CORE DISTANCE RANGE FOR THE EVALUATION OF THE STRUCTURE FUNCTION RATIO, $R(r_1, r_2)$

(Chantler et al, 1981)

Array size	energy range	r_1	r_2
100m	3×10^{15} eV - 6×10^{15} eV	50m	100m
200m	6×10^{15} eV - 2×10^{16} eV	75m	150m
400m	3×10^{16} eV - 10^{18} eV	150m	300m

been made more recently by Orford et al (1981) on $\sim 10^{16}$ eV showers from the 200m array and $\sim 10^{17}$ eV showers from the 400m array.

These results have established the time delay, TD, as a well-behaved function of core distance and have shown a correlation between TD and the Cerenkov light structure function ratio, $R(r_1, r_2)$. The indications are that TD, the time delay between the Cerenkov light and the particle front, promises to be a useful measure of electron cascade development giving complementary information to shower development characteristics from pulse shape and optical photon lateral distribution studies.

It must be emphasised here that the pulse shape data analysis, as well as the analysis on other Cerenkov light characteristics, is still being carried out by the University of Durham Extensive Air Showers Group. There is optimism that fresh results will emerge from these analyses.

CHAPTER SIX

INTERPRETATION OF THE DUGWAY PULSE SHAPE DATA.

6.1 Introduction.

In this Chapter comparisons will be made between the observed Cerenkov light pulse shape characteristics measured at Dugway and pulse shape data from other recent experiments. The data will also be compared with up to date computer simulation results from the Durham group.

A consistent set of computer simulation data is now available for the primary energy range 10^{15} eV - 10^{18} eV, and for vertical as well as inclined showers, from the latest theoretical studies by McComb and Turver (1981). These data enable us to compare the experimental results from Dugway with theoretical predictions, and also to interprete the observed pulse shape characteristics, particularly in understanding electron cascade development. The computer simulations are based on the Feynman scaling model for an iron nucleus primary.

Direct comparison between the Dugway data and results from other experiments must be attempted with caution because of the varying atmospheric depths of extensive air shower arrays around the World, and the detector bandwidth at each installation. Reasonable comparison can only be made after removal of system bandwidth from the measured pulse shape parameters, and the resultant values must be normalised to account for the atmospheric depth variation.

6.2 Dugway Pulse Shape Measurements Compared with Simulated Pulses.

6.2.1 Comparison of Observed FWHM with Computer Simulations.

In Figures 6.1 and 6.2 the FWHM from the Dugway data are compared with computer simulation results from McComb and Turver (1981). Figure 6.1 shows the predicted FWHM for showers of energy 10^{16} eV (appropriate to the mean energy of the 200m array data) and zenith angles 0° , 35° , and 45° . Figure 6.2 shows simulations for the same set of zenith angles for 10^{17} eV primary energy, which is close to the mean energy of the 400m array data.

Also shown on Figures 6.1 and 6.2 are the average FWHM (without any system bandwidth) for given zenith angle and primary energy bins from the data analysed in this work. The error bars represent the standard errors for each data point. The data show general agreement with the predictions from computer simulations.

6.2.2 Comparison of Observed Rise Time with Computer Simulations.

The observed Rise Times from the 400m array data are compared with computer simulation results in Figure 6.3 (a-c). All system bandwidth effects have been removed from the data.

At core distances less than 250m, the Cerenkov light pulses appear to have slower rise times than predicted by simulations. This may be due to an instrumental broadening that has not been accounted for yet by the current theoretical studies. Further investigation may be required on the deconvolution before this can be confirmed. Another reason might be that the quartic spline is not flexible enough to cope adequately with

FIGURE 6.1

COMPARISON OF FWHM FROM THE DUGWAY DATA,  ,

(mean energy = 3 x 10^{16} eV) WITH COMPUTER

SIMULATIONS, ——— , (iron-initiated primary, E = 10^{16} eV)

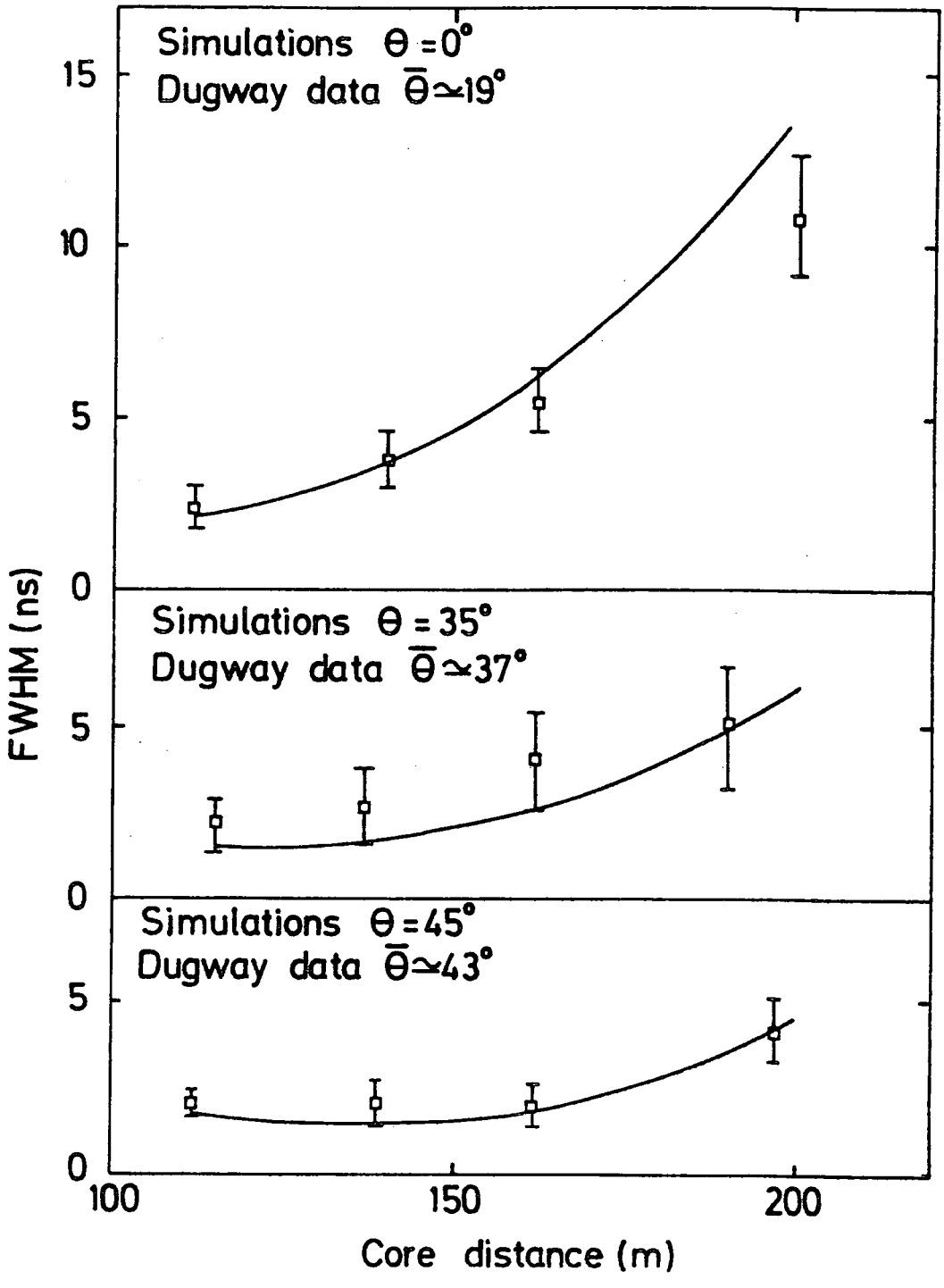
Simulations θ = 0°
Dugway data θ̄ ≃ 19°
Simulations θ = 35°
Dugway data θ̄ ≃ 37°
Simulations θ = 45°
Dugway data θ̄ ≃ 43°
FWHM (ns)
15
10
5
0
5
0
5
0
100
150
200
Core distance (m)

FIGURE 6.2

COMPARISON OF FWHM FROM THE DUGWAY DATA,  ,

(mean energy = 1.7 x 10^{17} eV) WITH COMPUTER

SIMULATIONS, ——— , (Iron nucleus, E = 10^{17} eV)

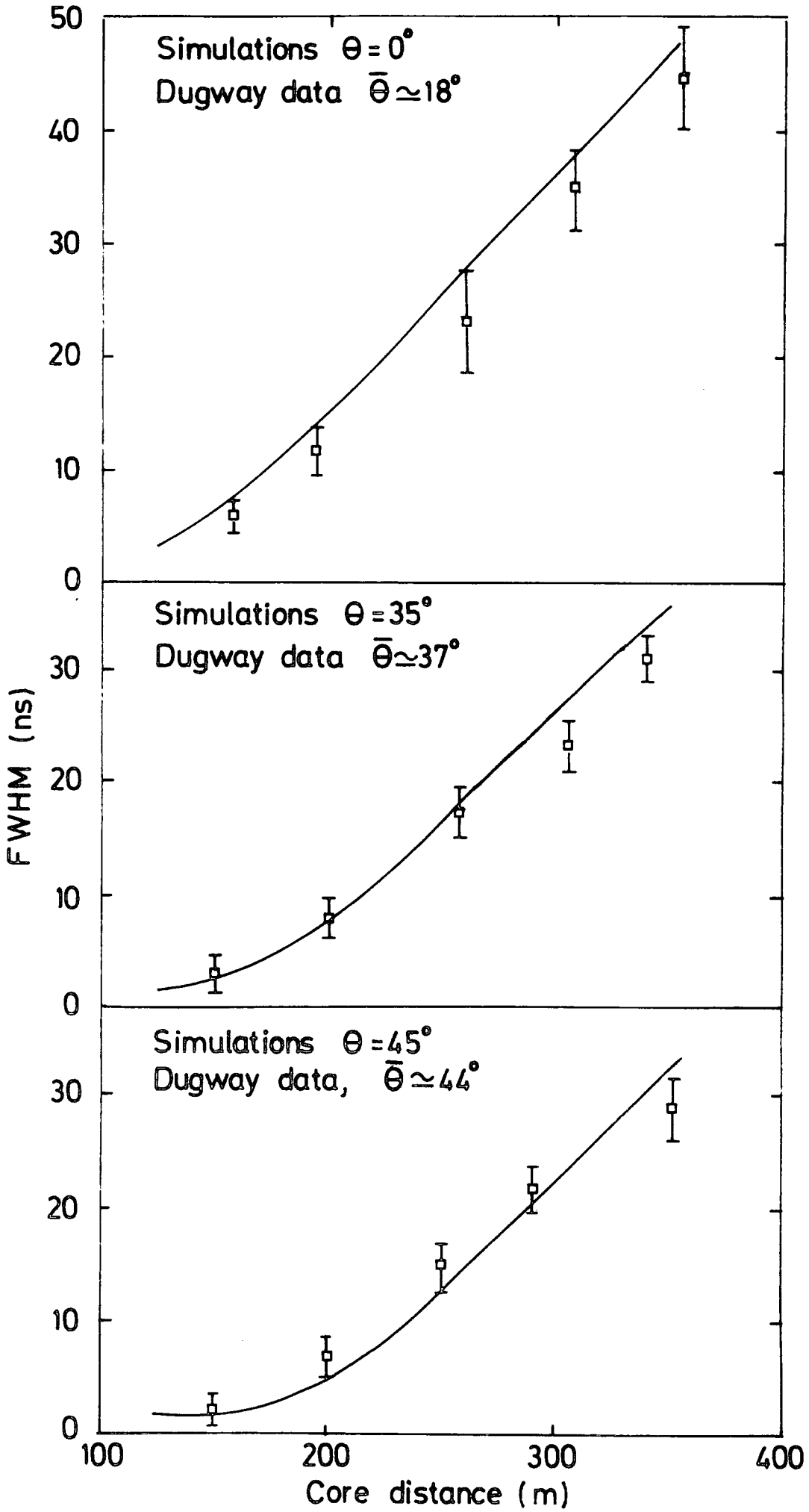
Simulations Θ = 0°
Dugway data Θ̄ ≃ 18°
Simulations Θ = 35°
Dugway data Θ̄ ≃ 37°
Simulations Θ = 45°
Dugway data, Θ̄ ≃ 44°
FWHM (ns)
Core distance (m)
0
10
20
30
40
50
100
200
300
400

FIGURE 6.3

COMPARISON OF RISE TIMES FROM THE DUGWAY DATA,  ,
(mean energy = 1.7 x 10^{17} eV) WITH COMPUTER
SIMULATIONS, ——, (Iron nucleus, E = 10^{17} eV)

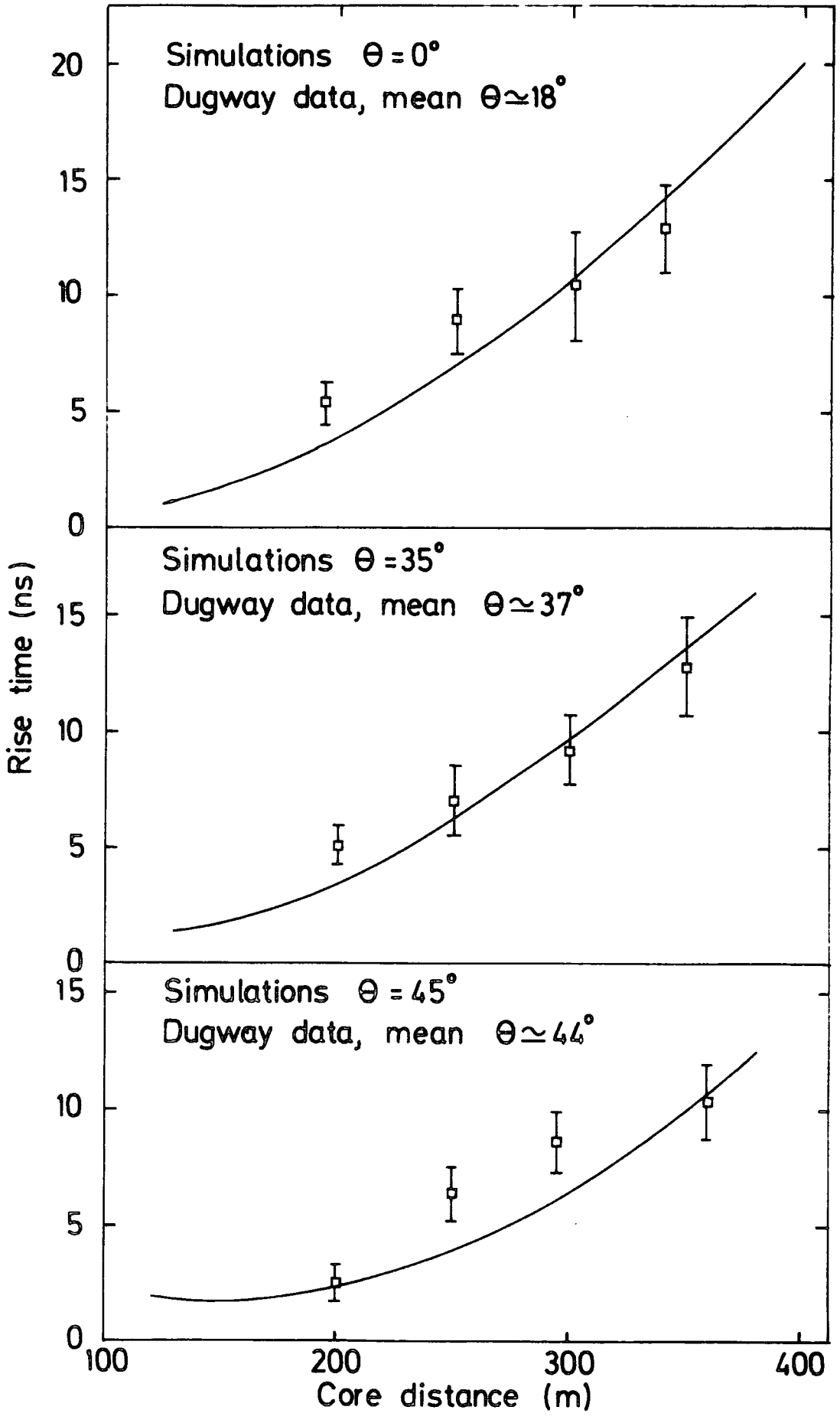
Simulations Θ = 0°
Dugway data, mean Θ≃18°
Simulations Θ = 35°
Dugway data, mean Θ≃37°
Simulations Θ = 45°
Dugway data, mean Θ≃44°
Rise time (ns)
Core distance (m)
0
5
10
15
20
100
200
300
400

pulses in this region.

6.2.3 Observed Top Time and Fall Time Compared with Computer Simulations.

Figure 6.4 shows a comparison between the observed Top Time from the data sample presented in this work and computer simulation results from McComb and Turver (1981). In Figure 6.5 the Fall Times of Cerenkov light pulses measured at Dugway are compared with simulation data from the same authors. The Dugway data are from the 400m array and have a mean energy of $\sim 1.65 \times 10^{17}$ eV. The computer simulations are for 10^{17} eV primary nucleus.

For both Top Time and Fall Time, there is an apparent discrepancy between the Dugway data and theoretical predictions. This may be due partly to instrumental broadening. No attempt has been made here to remove the system bandwidth effects from Top Time and Fall Time because of a lack of adequate deconvolution data from computer simulations at this time.

Moreover, the Top Time and Fall Time depend critically on the actual shape of the pulse. Unlike the FWHM, which approximates to the Second Moment and is therefore a first order estimate, Top Time and Fall Time depend upon higher order Moments. Their computation therefore depend on more accurate reconstruction of the pulse shape which the quartic spline may not be flexible enough for. Also, the Fall Time depends more critically on the angular distribution of the Cerenkov light and consequently on the linear distance between the observation plane and the depth of electron cascade maximum.

FIGURE 6.4

COMPARISON OF TOP TIME FROM THE DUGWAY DATA,  ,

(mean energy = 1.7 x 10^{17} eV) WITH COMPUTER

SIMULATIONS, ——, (Iron nucleus, E = 10^{17}eV)

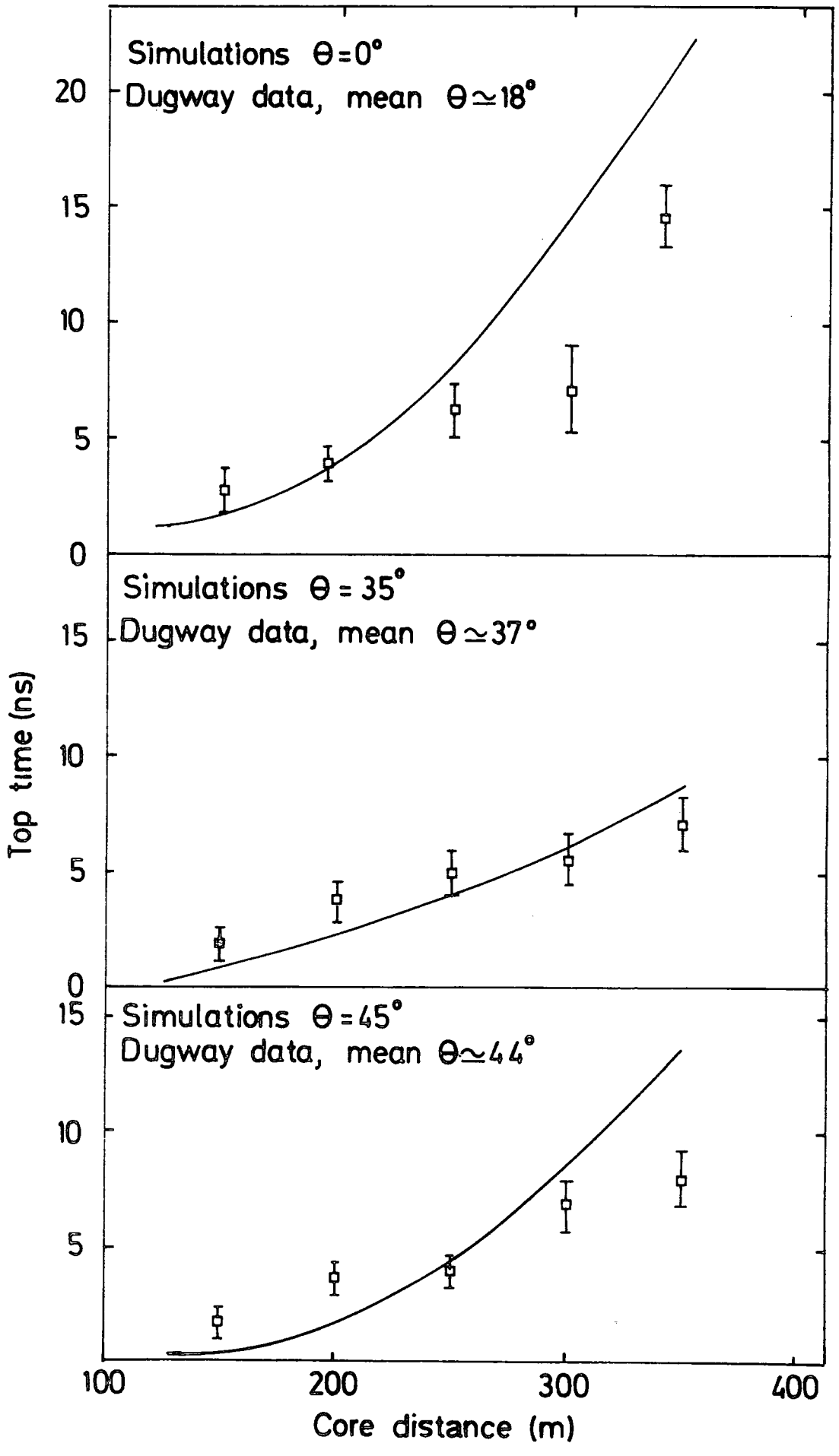
Simulations Θ=0°
Dugway data, mean Θ≃18°
Simulations Θ=35°
Dugway data, mean Θ≃37°
Simulations Θ=45°
Dugway data, mean Θ≃44°
Top time (ns)
Core distance (m)
0
5
10
15
20
100
200
300
400

FIGURE 6.5

COMPARISON OF OBSERVED FALL TIME FROM THE DUGWAY 400m ARRAY,  , (mean energy = 1.7×10^{17} eV) WITH COMPUTER SIMULATIONS, ——— , (Iron nucleus, E = 10^{17}eV)

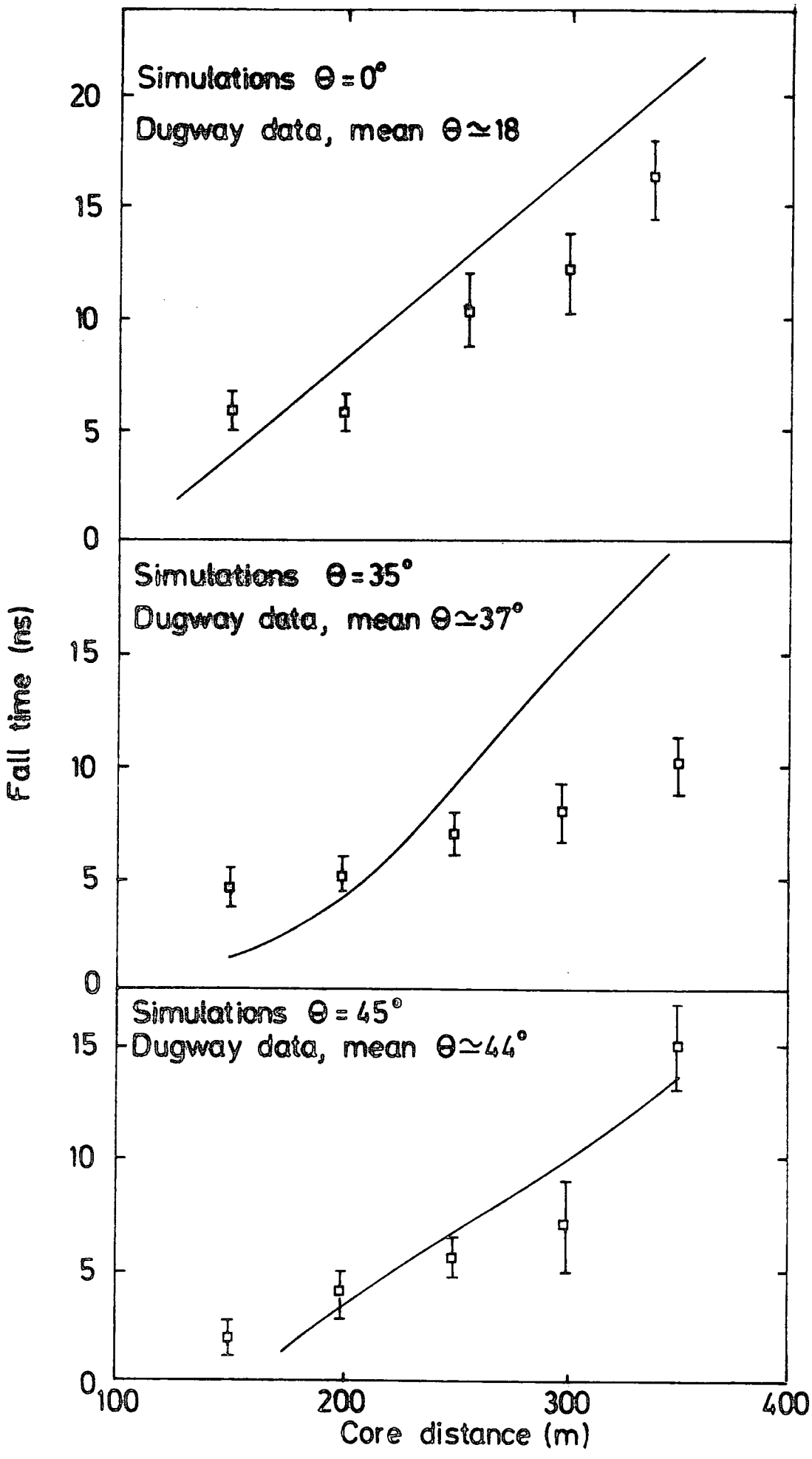
Simulations Θ = 0°
Dugway data, mean Θ ≃ 18
Simulations Θ = 35°
Dugway data, mean Θ ≃ 37°
Simulations Θ = 45°
Dugway data, mean Θ ≃ 44°
Fall time (ns)
Core distance (m)
0
5
10
15
20
100
200
300
400

6.2.4 Comparison Between Predicted and Observed FWHM Close to the Core.

The observed Cerenkov light FWHM at radial distances very close to the core was given a special mention in Chapter 5 because of its strange behaviour with core distance changes. The FWHM increases with decreasing core distance at core distances 100m, according to computer simulations, and the broadening of pulses close to the shower core is predicted to be more evident for low energy showers at highly inclined angles of incidence.

This prediction is borne out by the data from the 200 metre array (mean energy, 3×10^{16} eV) at zenith angles 45° - 60°. The data are compared with computer simulation results from McComb and Turver (1981), and agree well with simulations as Figure 6.6 shows. System bandwidth effects have been removed from the Dugway data, and corrections have been made for pulse shape reconstruction errors.

6.3 Dugway Pulse Shape Data Compared with Results from other Experiments.

Hammond et al (1978) have reported recent measurements of Cerenkov light pulses at sea level, using an array of 8 detectors at Haverah Park. Their results will be compared with the Dugway pulse shape data presented in this Thesis.

The system bandwidths quoted for the Haverah Park array by Hammond et al (1978) are 19 ns for FWHM and 9 ns for Rise Time. Cerenkov light measurements were made at core distances up to 600m. At Dugway (altitude 862 g cm^{-2}) measurements were made in the core distance range 50m - 400m with an array of 8 detectors which responded to a delta function of light with a bandwidth of 6.7 ns for FWHM and 6.5 ns for Rise Time.

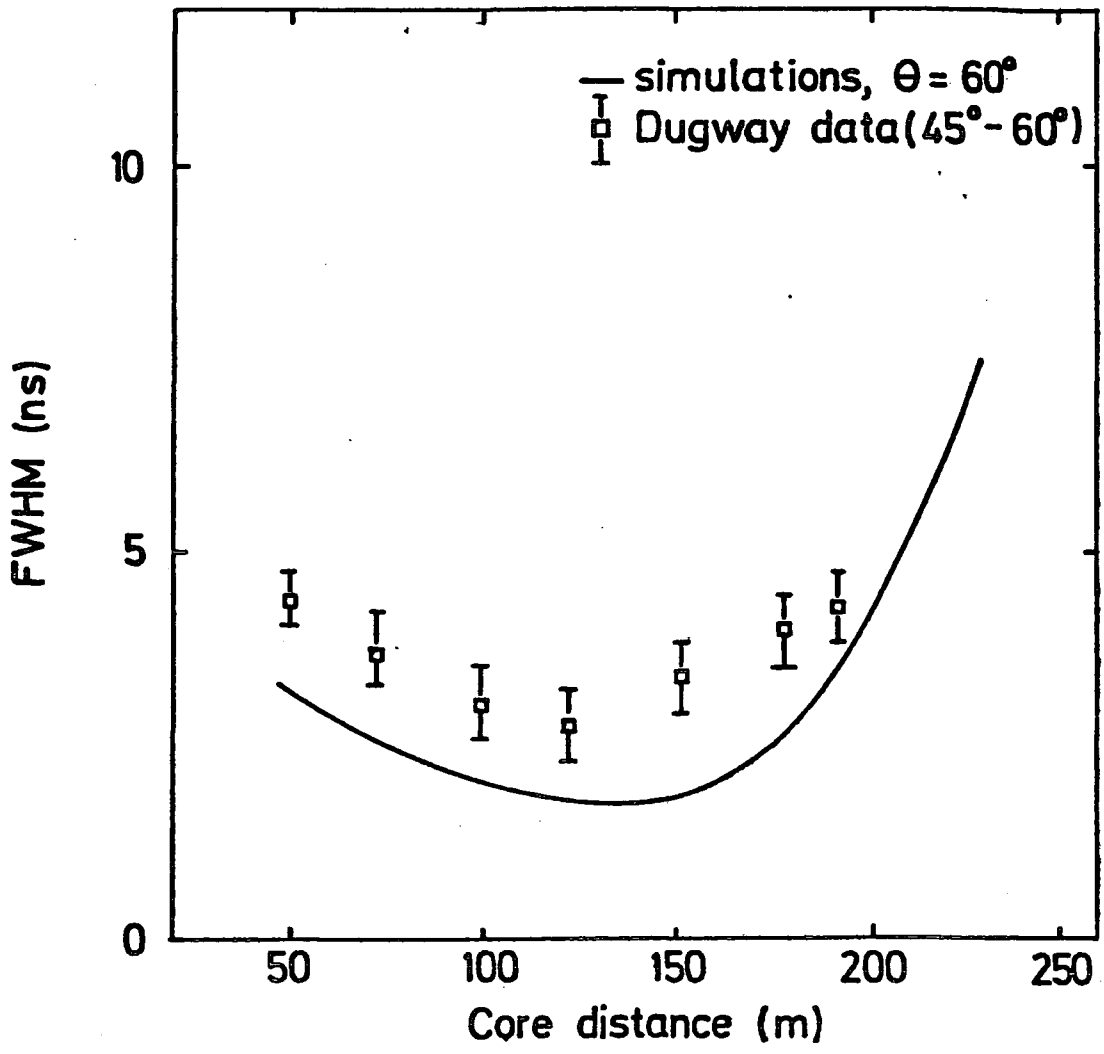

FIGURE 6.6

VARIATION OF FWHM WITH CORE DISTANCE FOR SMALL ($\bar{E}_p$ = 3 x 10^{16} eV), HIGHLY INCLINED ($45^\circ < \theta \leq 60^\circ$) SHOWERS CLOSE TO THE CORE, COMPARED WITH COMPUTER SIMULATIONS (iron nucleus, θ = 60°, E = 10^{16} eV)

The Haverah Park pulse shape data quoted by Hammond et al (1978) include their system bandwidth. The Dugway data reported in this Thesis have been corrected for system bandwidth effects, and pulse shape reconstruction errors (See Chapter 5). Figure 6.7 shows a comparison between the Rise Times of the Haverah Park data (Hammond et al, 1978) and the Dugway data. For this comparison, the Haverah Park measurements have been corrected for bandwidth effects by this author by assuming that the system response adds in quadrature with the measured pulse shape data. This assumption may only be approximate but, in the view of this author, will suffice in the absence of any other method of deconvolution.

The FWHM is the only pulse shape parameter available from Cerenkov light measurements at Adelaide, Australia, (See e.g. Thornton and Clay, 1978; Thornton et al, 1979; Kuhlmann et al, 1981). Thornton and Clay (1978) have reported measurements of extensive air showers of particle size $\sim 5 \times 10^5$ (primary energy $\sim 10^{16}$ eV), at sea level, over core distances up to 250m. The system bandwidth for their detectors has been quoted as 5.3 ns and 4.5 ns by Thornton et al (1979), and is removed from their measured signal on an assumption that the detector response and observed parameters add in quadrature (Thornton and Clay, 1978). The FWHM(300m) obtained by these authors from a regression of their data on the relation :

$$FWHM(r) = a + br^2 \qquad 6.1$$

is 20 +/- 1 ns, for shower size $\sim 5.5 \times 10^5$ (N_e). This is compared with the mean value of FWHM(300m) which is 20.2 +/- 0.3 ns for showers of mean energy 1.65×10^{17} eV analysed in this work. These showers were

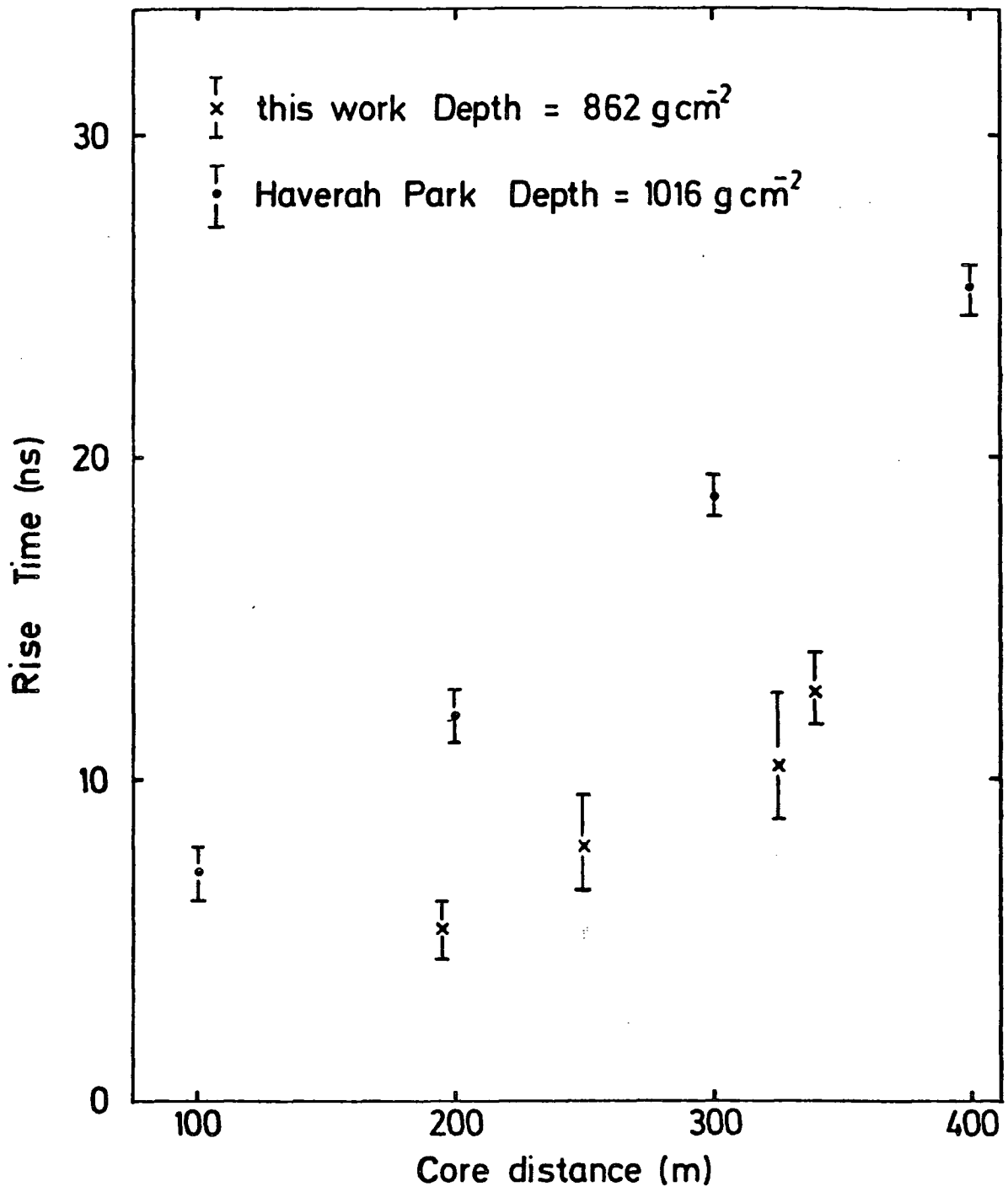

FIGURE 6.7

COMPARISON OF RISE TIMES FROM DUGWAY DATA ($\bar{\theta} \simeq 18^{\circ}$, $\bar{E} = 1.7 \times 10^{17}$eV, without system bandwidth) WITH QUOTED DATA FROM HAVERAH PARK, $\bar{E} \simeq 10^{17}$eV (Hammond et al, 1978), CORRECTED FOR SYSTEM RESPONSE AND VERTICAL INCIDENCE.

selected from the 400m array data in the zenith angle range 0^{o} - 45^{o}.

Measurements of the pulse shapes of Cerenkov light from extensive air showers of energy $\sim 10^{17}$ eV made at Yakutsk, USSR, have been reported by Efimov et al (1973), Kalmykov et al (1979, 1981), and Grigoriev et al (1978). Grigoriev et al (1978) quoted the system bandwidth at Yakutsk as 10 ns for Rise Time and 14 ns for FWHM. Kalmykov et al (1979) have fitted their data, measured over a core distance range of 300m - 600m, to the functional form :

$$\text{FWHM}(r) \propto r^{n} \qquad 6.2$$

with $n \simeq 2.0$, to obtain a value for FWHM(300m) which was used in a regression to obtain the depth of electron cascade maximum. Like the Adelaide group, the Russian group correct for their system bandwidth by assuming that the observed FWHM and the system bandwidth add in quadrature, (See Kalmykov et al, 1979).

In Figure 6.8(a,b) the Dugway Cerenkov light pulse FWHM are compared with the FWHM quoted by Hammond et al (1978) from Haverah Park, the FWHM data from Yakutsk (Grigoriev et al, 1978), and the FWHM data from the Adelaide array (Thornton and Clay, 1978)

The Dugway data used for this comparison are for near-vertical showers, mean zenith angle $\simeq 18^{o}$. Data from Hammond et al (1978), Grigoriev et al (1978) and Thornton and Clay (1978) have been corrected by the authors to vertical incidence. Thornton and Clay (1978) and Grigoriev et al (1978) have corrected their data for bandwidth effects. This author has removed the system response from the data of Hammond et al (1978).

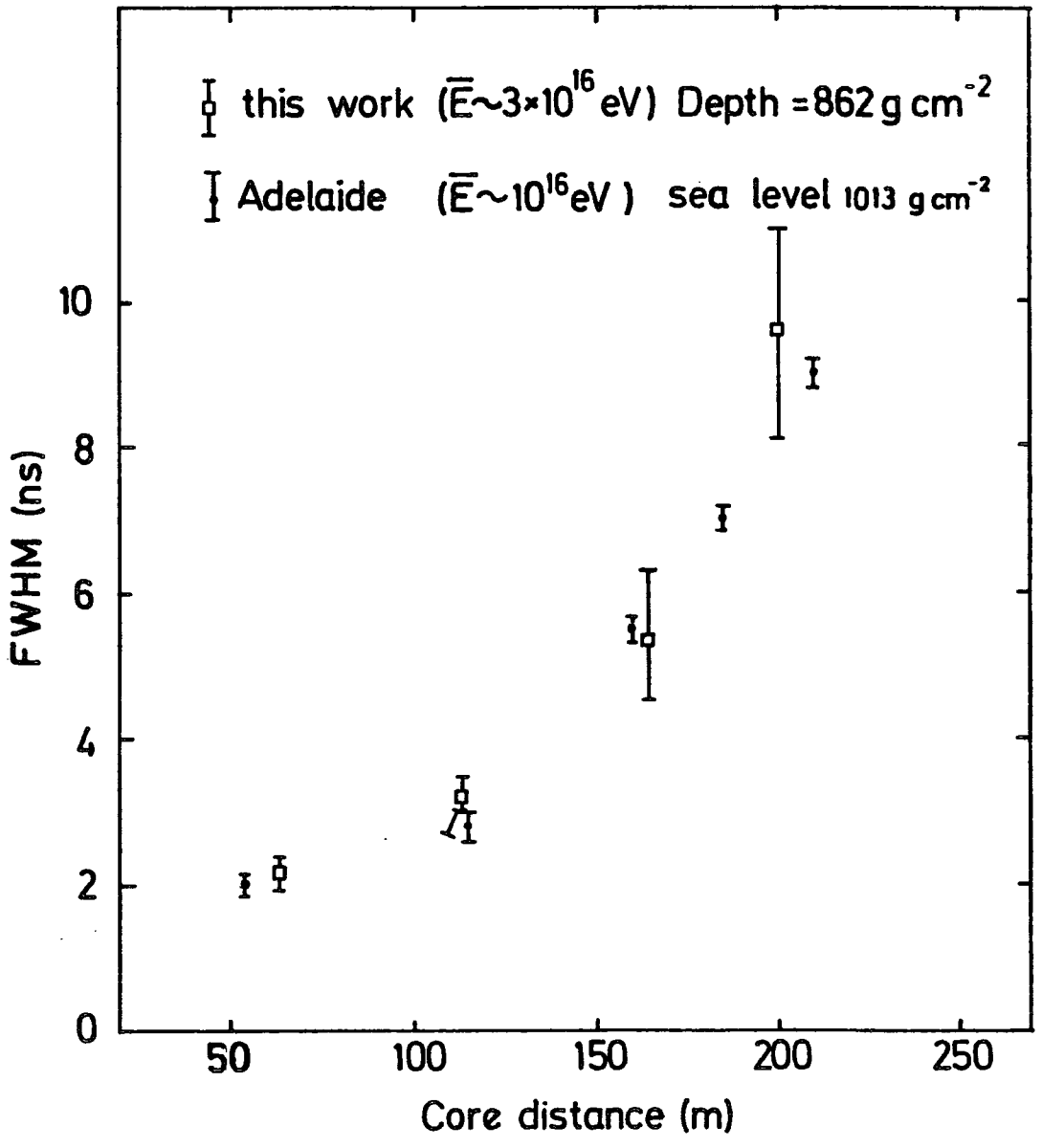

FIGURE 6.8(A)

COMPARISON OF DUGWAY FWHM FOR SHOWERS OF MEAN ZENITH ANGLE $\simeq 18^{\circ}$ WITH DATA FROM ADELAIDE (Thornton and Clay, 1978) CORRECTED TO VERTICAL INCIDENCE. System bandwidth has been removed from both sets of data.

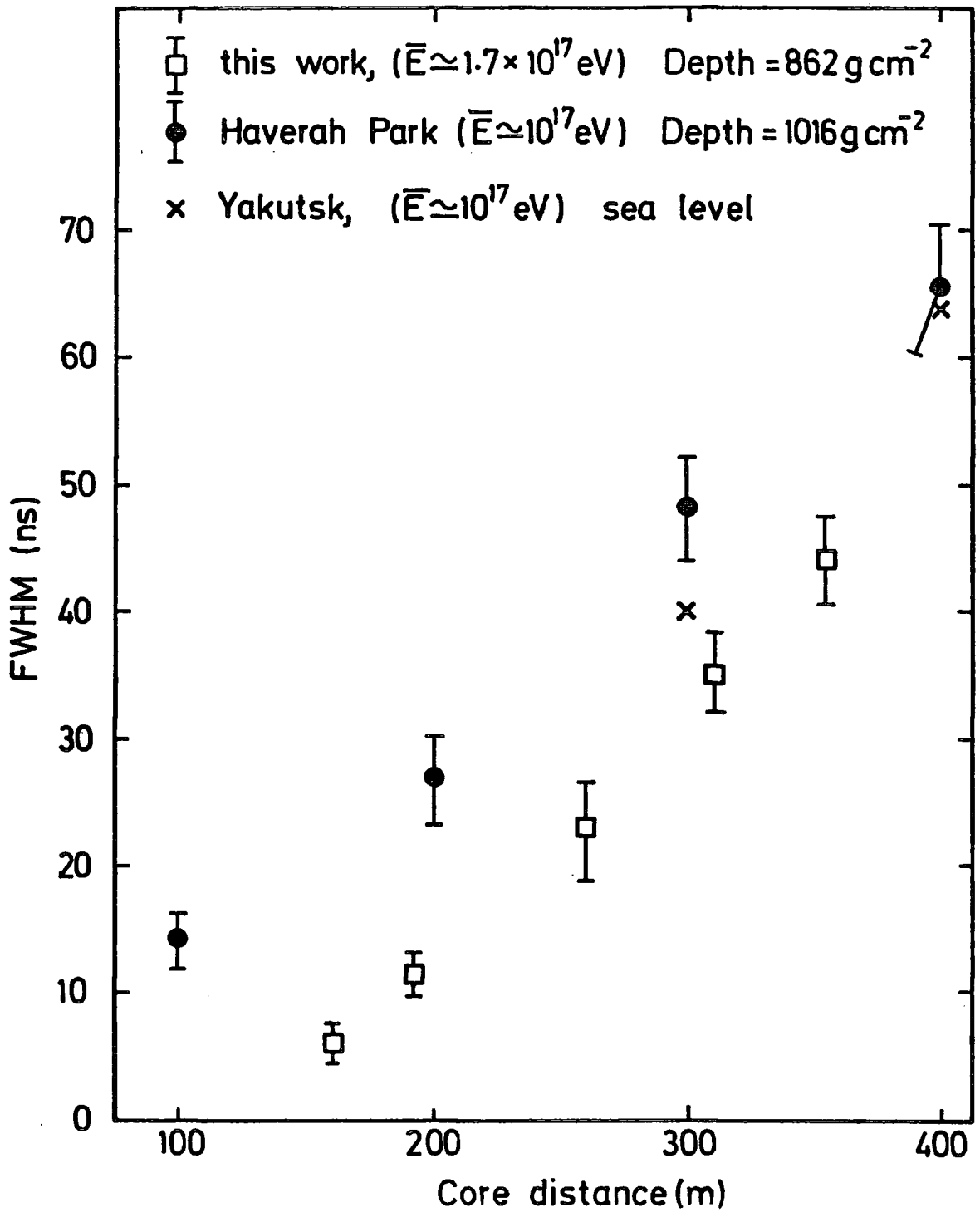

FIGURE 6.8(B)

COMPARISON OF DUGWAY FWHM FOR SHOWERS OF MEAN ZENITH ANGLE $\simeq 18^{\circ}$ WITH DATA FROM HAVERAH PARK (Hammond et al, 1978) AND YAKUTSK (Grigoriev et al, 1978) CORRECTED TO VERTICAL INCIDENCE. System bandwidths have been removed from all the data.

6.4 Pulse Shape as a Measure of Electron Cascade Development.

The FWHM and Rise Time measured at Dugway have been interpreted to give the depths of electron cascade maxima for the extensive air showers. This procedure is now explained in the following Sections.

6.4.1 Determination of Depth of Electron Cascade Maximum from FWHM.

The depths of electron cascade maxima have been derived from FWHM by first removing the system response from the observed parameters. The FWHM from each pulse in a given shower was deconvoluted to 'true' FWHM (i.e. without system response) by comparing the observed parameter with the FWHM from computer simulations appropriate to each detector and the Dugway atmosphere. Corrections were made for pulse shape reconstruction errors.

The data were sub-divided into secant theta bins of 0.1 width and core distance bins of 25m for the 200m array data and 50m for the 400m array data. The mean FWHM for each zenith angle/core distance bin (with standard error) was then related to computer simulations as shown in Figures 6.9(a-f). Each diagram shows the simulated pulse FWHM at given zenith angle for extensive air showers maximising at different depths in the atmosphere.

From these diagrams, the depth of electron cascade maximum for the average energy of the showers in each zenith angle/core distance bin was derived. These depths of maxima are listed in Table 6.1. The weighted average obtained from the 16 measurements from the 400m array is 682 +/- 13 g cm^{-2} for a mean energy of 1.65 x 10^{17}eV. Bandwidth effects restricted the core distance range of the 200m array data to 8 data points

with adequate sensitivity. These are listed in Table 6.2 and give a weighted mean of 583 +/- 26 g cm^{-2} for the mean energy of 3 x 10^{16} eV. The 20 high energy showers from the 200m array have been treated separately to give a depth of maximum of 646 +/- 32 g cm^{-2} for the mean energy 6.5 x 10^{16} eV, (See Figure 6.9(c) and Table 6.2).

6.4.2 Determination of Depth of Electron Cascade Maximum from Rise Time.

The Rise Times of Cerenkov light pulses have been used in this work to derive depths of electron cascade maxima for extensive air showers. The procedure followed was the same as that used for the FWHM interpretation in Section 6.4.1. The observed Rise Times were corrected for pulse shape reconstruction errors.

Because of the effect of system bandwidth on Rise Time, which is more prominent than on FWHM, the Rise Time-derived depths of maxima have been restricted to core distances of 300m and 350m. Eight values of depths of electron cascade maxima have been derived from Rise Times from the 400m array data (See Figure 6.10). These values are listed in Table 6.3 and give a weighted average of 696 +/- 27 g cm^{-2} for a mean energy of 1.7 x 10^{17} eV, which agrees with the results obtained from FWHM.

6.4.3 Derived Depths of Maxima from this Work Compared with other Results.

The variation of depth of maximum with primary energy is shown in Figure 6.11, comparing the results from this work with the depths of electron cascade maxima derived from optical photon lateral distribution from Dugway measurements, (See Andam et al, 1981). In Figure 6.12 the

FIGURE 6.9(A - F)

DERIVATION OF DEPTH OF ELECTRON CASCADE MAXIMUM

FROM FWHM

— SIMULATIONS

⋇ This work, $\bar{E} \simeq 3 \times 10^{16}$ eV

⋔ This work, $\bar{E} \simeq 1.65 \times 10^{17}$ eV

⋔ This work, $\bar{E} \simeq 6.5 \times 10^{16}$ eV

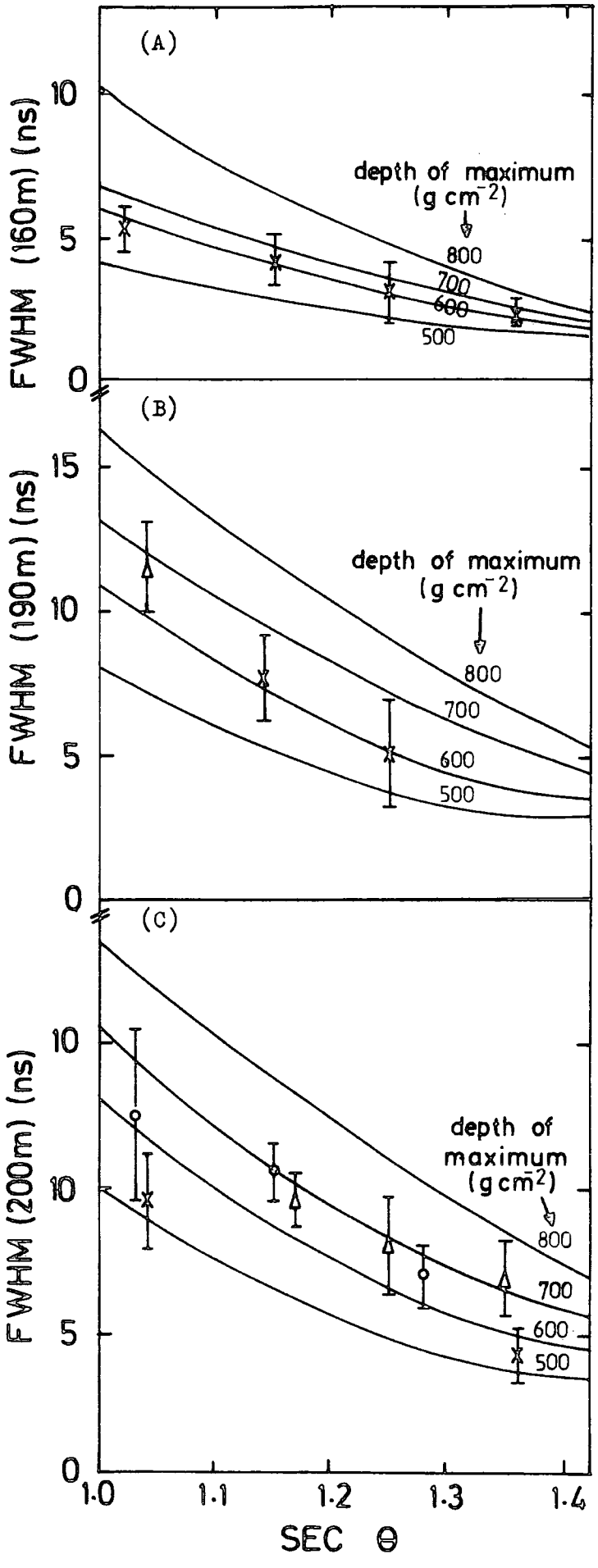
(A)
FWHM (160m) (ns)
depth of maximum
(g cm⁻²)
800
700
600
500
(B)
FWHM (190m) (ns)
depth of maximum
(g cm⁻²)
800
700
600
500
(C)
FWHM (200m) (ns)
depth of
maximum
(g cm⁻²)
800
700
600
500
SEC θ

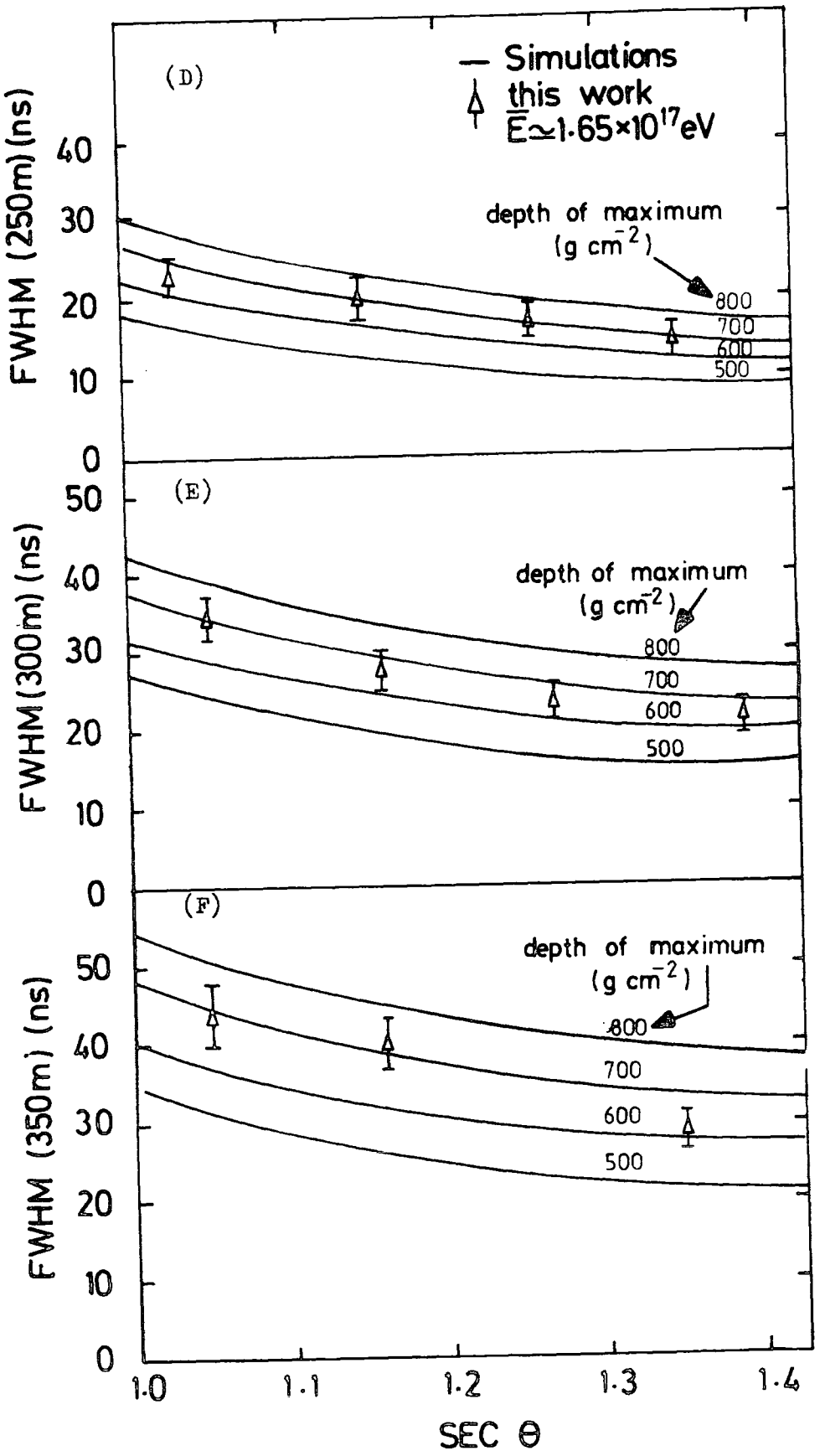
(D)
— Simulations
this work
Ē≃1·65×10¹⁷eV
depth of maximum
(g cm⁻²)
800
700
600
500
FWHM (250m) (ns)
40
30
20
10
0
(E)
depth of maximum
(g cm⁻²)
800
700
600
500
FWHM (300m) (ns)
50
40
30
20
10
0
(F)
depth of maximum
(g cm⁻²)
800
700
600
500
FWHM (350m) (ns)
50
40
30
20
10
0
1·0
1·1
1·2
1·3
1·4
SEC θ

TABLE 6.1

DERIVED DEPTHS OF ELECTRON CASCADE MAXIMA FROM FWHM,

400m ARRAY DATA.

secant θ bin	mean energy (eV)	mean sec θ	mean core distance (m)	mean FWHM (ns)	derived depth of maximum ($g\ cm^{-2}$)
1.0 - 1.1	2.3×10^{17}	1.04	193 ± 3	11.5± 1.6	680 ± 90
	1.7×10^{17}	1.03	259 ± 7	23.1± 3.8	650 ± 50
	2.3×10^{17}	1.05	308 ± 5	34.8± 2.9	700 ± 40
	2.0×10^{17}	1.05	354 ± 16	43.6± 3.8	690 ± 40
1.1 - 1.2	1.5×10^{17}	1.17	202 ± 4	9.6± 0.9	680 ± 50
	1.6×10^{17}	1.15	248 ± 5	20.1± 2.7	700 ± 60
	1.6×10^{17}	1.16	293 ± 5	28.4± 2.1	670 ± 70
	1.9×10^{17}	1.16	347 ± 7	40.5± 2.9	720 ±60
1.2 -1.3	1.2×10^{17}	1.25	213 ± 5	7.8± 1.7	690 ± 60
	1.5×10^{17}	1.26	257 ± 3	17.5± 2.0	710 ± 50
	1.4×10^{17}	1.27	305 ± 4	23.4± 1.9	670 ± 70
	1.6×10^{17}	1.27	339 ± 7	30.8± 1.9	690 ± 60
1.3 -1.4	1.9×10^{17}	1.35	201 ± 6	6.8± 1.4	710 ± 40
	1.2×10^{17}	1.35	251 ± 4	14.8± 1.9	710 ± 50
	1.4×10^{17}	1.39	288 ± 4	21.8± 2.0	650 ± 50
	1.6×10^{17}	1.35	351 ± 9	28.6± 2.5	630 ± 80

TABLE 6.2

DERIVED DEPTHS OF ELECTRON CASCADE MAXIMA FROM FWHM,

200m ARRAY DATA.

secant θ bin	mean energy (eV)	mean sec θ	mean core distance (m)	mean FWHM (ns)	derived depth of maximum ($g\ cm^{-2}$)
1.0 - 1.1	3.5×10^{16}	1.02	162 ± 2	5.4±0.8	570 ± 40
	2.4×10^{16}	1.04	200 ± 4	9.6±1.6	530 ± 80
	5.9×10^{16}	1.03	201 ± 7	12.5±3.0	620 ± 100
1.1 - 1.2	2.6×10^{16}	1.15	161 ± 2	4.5±0.9	610 ± 70
	3.6×10^{16}	1.14	193 ± 3	7.7±1.5	580 ± 70
	6.8×10^{16}	1.15	205 ± 5	10.6±0.9	690 ± 40
1.2 - 1.3	2.6×10^{16}	1.25	162 ± 3	3.1±1.2	600 ± 120
	2.4×10^{16}	1.26	190 ± 2	5.1±1.9	580 ± 120
	6.5×10^{16}	1.28	202 ± 6	7.0±1.0	660 ± 60
1.3 - 1.4	2.5×10^{16}	1.36	162 ± 2	2.3±0.4	610 ± 100
	2.5×10^{16}	1.37	196 ± 6	4.2±1.0	570 ± 100

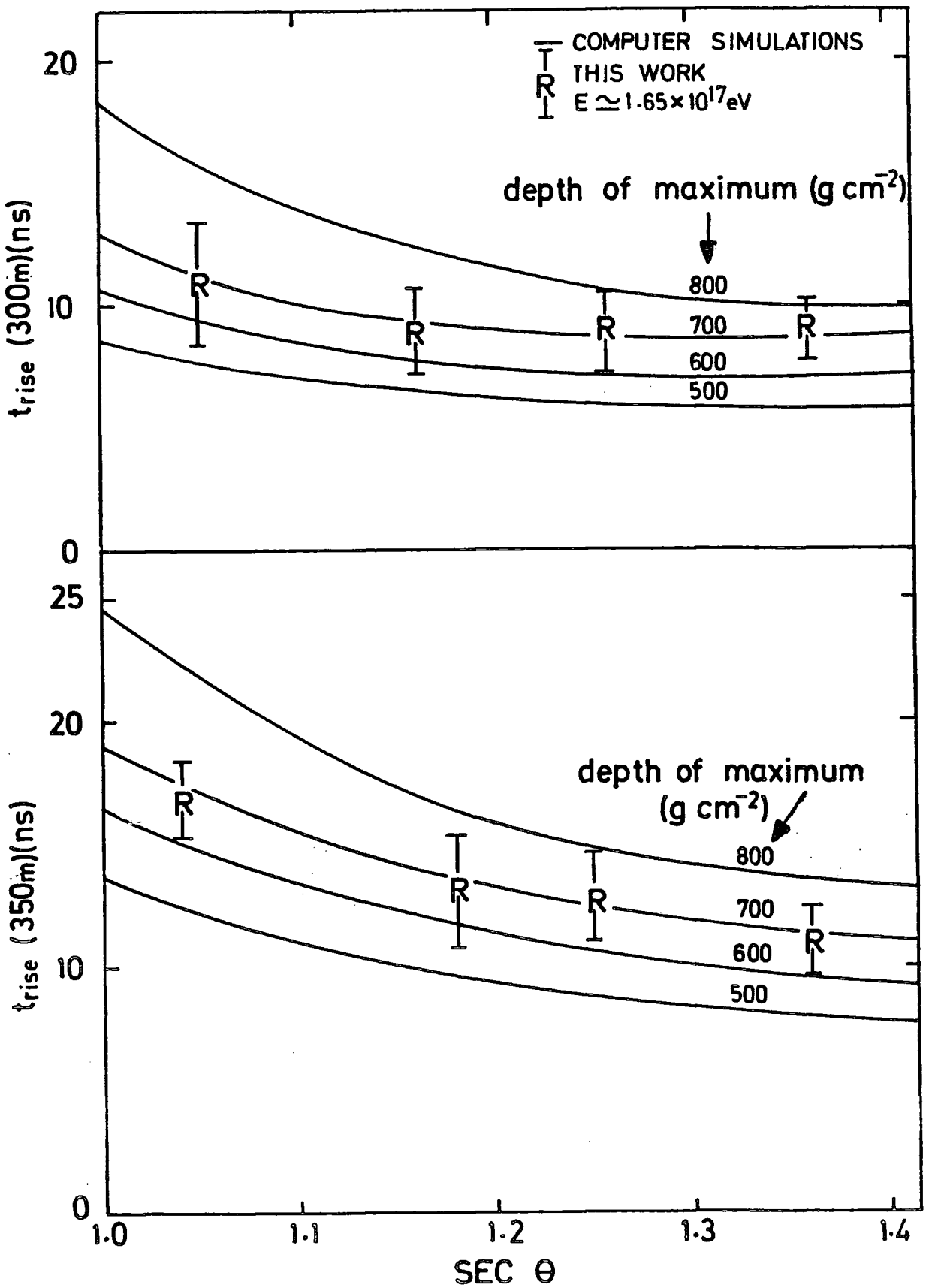

FIGURE 6.10

DETERMINATION OF DEPTH OF ELECTRON CASCADE MAXIMUM FROM RISE TIME MEASUREMENTS. DUGWAY 400m ARRAY DATA.

TABLE 6.3

DERIVED DEPTHS OF ELECTRON CASCADE MAXIMA FROM RISE TIME, 400m ARRAY DATA.

secant θ bin	mean energy (eV)	mean sec θ	mean core distance (m)	mean Rise Time (ns)	derived depth of maximum ($g\ cm^{-2}$)
1.0 - 1.1	1.6×10^{17}	1.05	303 ± 5	11.0±3.0	690 ± 120
	1.3×10^{17}	1.04	347 ± 2	16.8±1.7	680 ± 60
1.1 - 1.2	1.9×10^{17}	1.16	298 ± 6	9.1±1.9	680 ± 70
	1.6×10^{17}	1.18	349 ± 7	13.2±2.3	680 ± 120
1.2 - 1.3	1.3×10^{17}	1.26	301 ± 5	9.3±1.9	710 ± 60
	2.2×10^{17}	1.25	351 ± 5	12.6±1.9	710 ± 80
1.3 - 1.4	2.4×10^{17}	1.36	296 ± 4	8.9±1.3	740 ± 80
	1.4×10^{17}	1.36	353 ± 5	11.1±1.5	690 ± 90

depths of electron cascade maxima derived from pulse shape parameters are compared with the available data from other recent experiments. These include :

(1) Results on depths of maxima from the Haverah Park experiments;
   (a) The infilling experiment (Craig et al, 1979),
   (b) The deep water tank experiment (quoted by Linsley and Watson, 1981)
   (c) The optical Cerenkov light experiment (Hammond et al, 1978),
   (d) The Muon/Cerenkov experiment (Blake et al, 1979),
   (e) The Muon angles measurement (interpreted by McComb and Turver (1981))

(2) Depth of maximum measurements from the Russians (Antonov (interpreted by Watson and Linsley (1981), Grigoriev et al (1978), Glushkov et al (1979)). These measurements were all derived from Cerenkov light experiments.

(3) The depths of electron cascade maxima derived from FWHM measurements at Adelaide (Kuhlmann et al (1981), Thornton and Clay (1978)).

and (4) Other previous interpretations, including those of Bohm and Steinman (1979) and Tornabene (1979).

The important deduction that may be made from Figures 6.11 and 6.12 is that the depths of electron cascade maxima derived from pulse shape information in this work are consistent within the energy range of the data and with the depths of maxima derived from lateral distribution measurements from Dugway, as well as results from other experiments. The results from this work are also consistent with the computer simulations based on Feynman scaling model of an iron nucleus primary. The

FIGURE 6.11

DERIVED DEPTHS OF ELECTRON CASCADE MAXIMA FROM PULSE SHAPES COMPARED WITH DEPTHS OF MAXIMA DERIVED FROM CERENKOV LIGHT LATERAL DISTRIBUTION.

(Lateral distribution data from Andam et al, 1981)

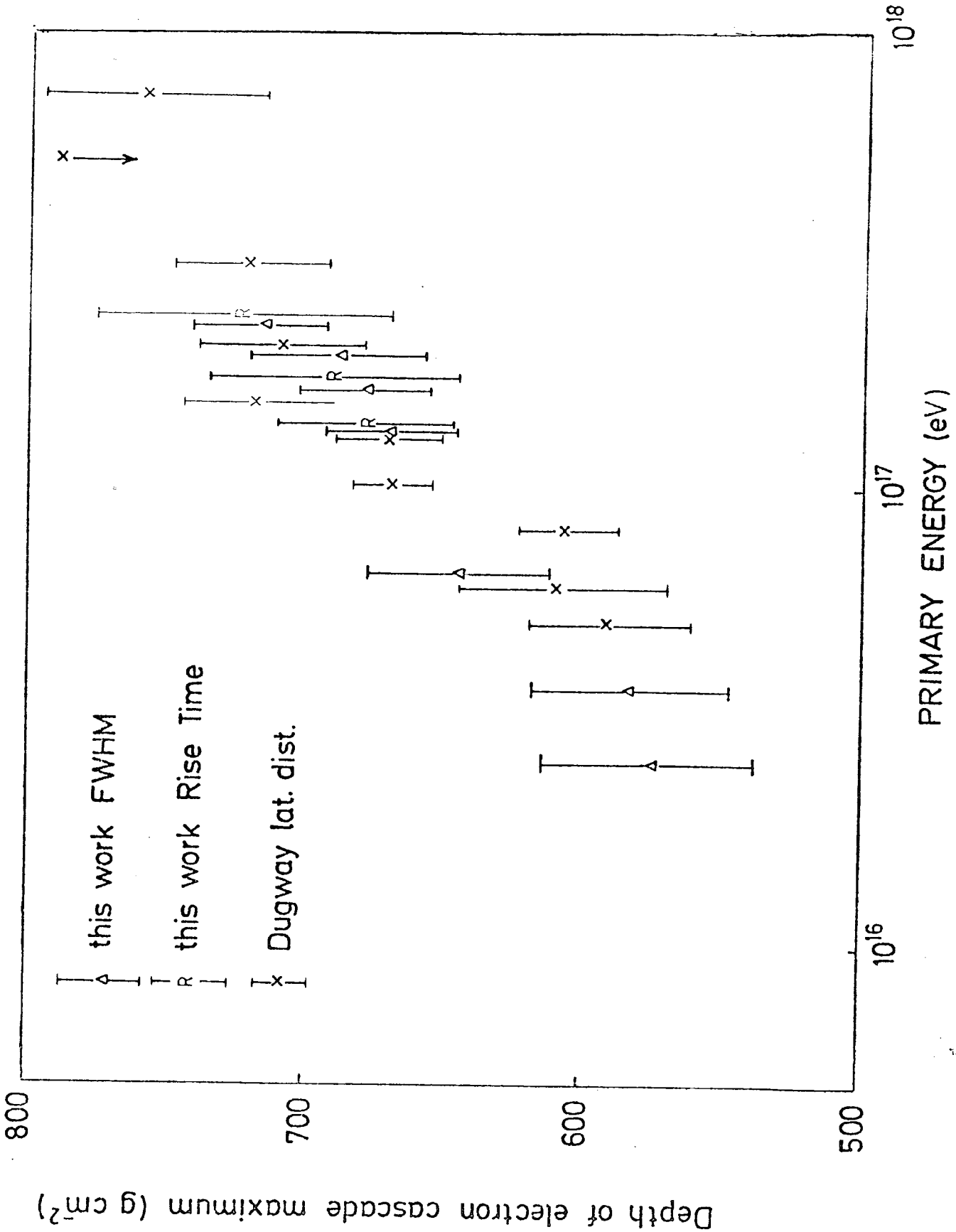
this work FWHM
this work Rise Time
Dugway lat. dist.
R
Depth of electron cascade maximum (g cm⁻²)
800
700
600
500
10¹⁶
10¹⁷
10¹⁸
PRIMARY ENERGY (eV)

FIGURE 6.12

DEPTHS OF ELECTRON CASCADE MAXIMA FROM DUGWAY PULSE SHAPES COMPARED WITH RESULTS FROM OTHER EXPERIMENTS.

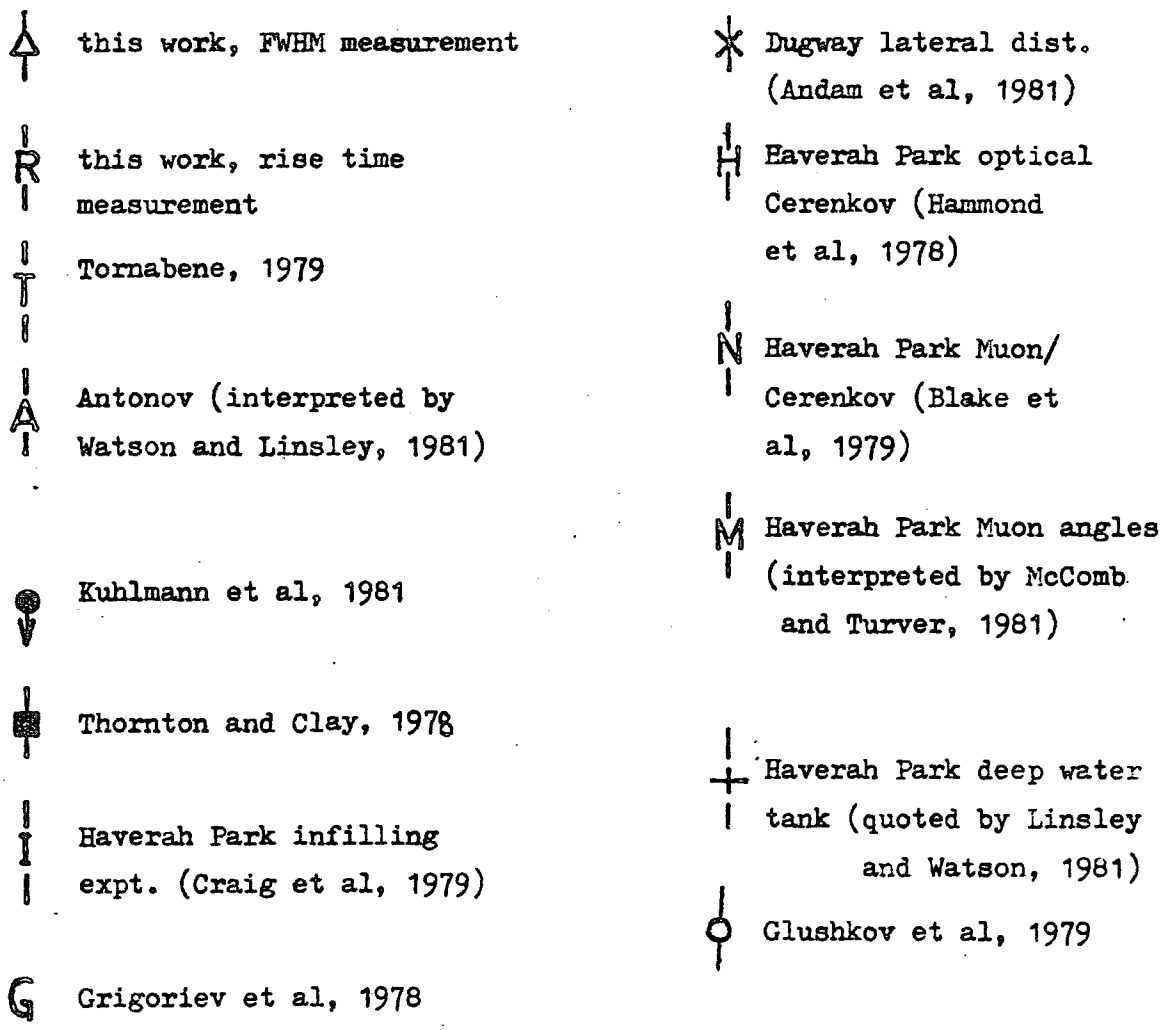

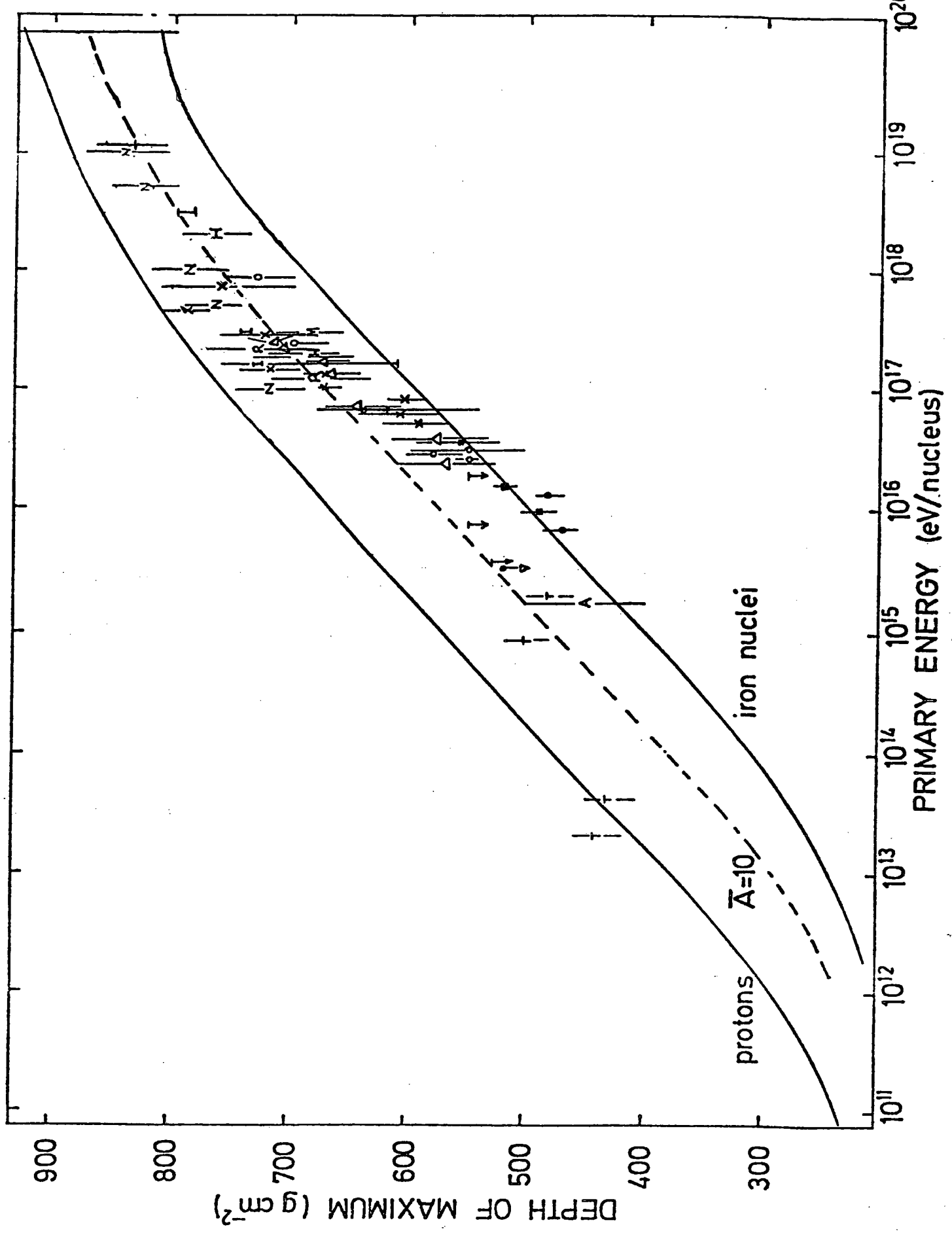
DEPTH OF MAXIMUM (g cm⁻²)
300
400
500
600
700
800
900
PRIMARY ENERGY (eV/nucleus)
10¹¹
10¹²
10¹³
10¹⁴
10¹⁵
10¹⁶
10¹⁷
10¹⁸
10¹⁹
10²⁰
protons
Ā=10
iron nuclei

depths of electron cascade maxima derived in this work are found to be independent of zenith angle.

Figure 6.12 illustrates the expected variation of depth of electron cascade maximum for a pure iron primary, a proton primary and a primary radiation with a mixture of nuclei averaging to $\bar{A} \simeq 10$. From this, it may be deduced that the results presented in this Thesis appear to favour a primary cosmic radiation comprising a mixture of heavy nuclei and protons.

CHAPTER SEVEN

CONCLUSIONS.

7.1 Overview.

This work has shown that, with an appropriate data fitting procedure, the Cerenkov light pulse shape can be reconstructed from digitised pulse information. The pulse shape parameters calculated from the reconstructed pulses have been used to deduce information about the electron cascade development of the extensive air showers.

The optical photon density at a measurable core distance, $\phi(150m)$, has been used as a primary energy estimator, and calculations based on it have been found to be in reasonable agreement with the results from other experiments. The availability of optical photon lateral distribution data from the Dugway experiment provides an alternative measure of the depth of electron cascade maximum which can be used to check the depth of electron cascade maximum determined from pulse shape parameters.

7.2 Implications of Pulse Shape Analysis for Cerenkov Light Studies.

The pulse shape parameters which have been used to deduce the electron cascade development of showers in this work are FWHM and Rise Time. It has been shown, through the comparison of experimental data with computer simulation results, that the FWHM and Rise Time can give a direct measure of the depth of electron cascade maximum of the extensive air shower from which the Cerenkov light emanates. This has been possible because of

the monotonic variation of the Cerenkov light pulse width with radial distance from the shower core, and the direct relationship between FWHM and zenith angle.

A knowledge of the depth of electron cascade maximum is expected to lead to information about the primary mass of the shower-initiating nucleon. The observed fluctuation of the pulse width can be used to predict the mass composition of the primary cosmic radiation and differentiate between a predominantly protonic primary and an iron or heavy mass primary.

Computer simulations predict a Rise Time variation with zenith angle that is not very simple and not yet fully understood. This may be due to the variation in the development of the shower which will be affected by Coulomb scattering and other electronic processes. However, as shown in Section 5.7.2 the Rise Time of the Cerenkov light pulse, at large radial distances from the core, varies monotonically with core distance. It has been possible in this work, to deduce the depth of electron cascade maximum from Rise Time measurements by choosing very narrow zenith angle bins and interpreting the observed Rise Time with the use of computer simulations.

The variation of Fall Time and Top Time with core distance and zenith angle has also been shown in this work. The Fall Time depends critically upon angular distribution of electrons and much less on longitudinal distribution. Therefore, Fall Time is not of much use in finding depth of electron cascade maximum, since its effects come in at a constant set of angles. This means that, for a given core distance, the effects of Fall Time cut off the light seen from below a given altitude from the array.

The peak height of Cerenkov light pulse has a predicted lateral distribution which is similar in shape to the pulse area lateral distribution. This is borne out by the experimental peak height lateral distribution (See Section 5.8). Therefore, the peak height, although subject to errors of pulse shape reconstruction, can be used directly in primary energy estimation. Errors due to data analysis techniques can be assessed and removed on average from the primary energy estimator.

From a knowledge of the pulse shapes of Cerenkov light, the percentage levels of the pulse may be used to reconstruct an image of the front curvature of the light and to make deductions about the longitudinal cascade development of the shower.

7.3 Suggestions for Further Work.

The pulse shape reconstruction procedures employed during this study portray an initial attempt at the analysis of the Dugway EAS data. The fitting of a unimodal quartic spline has proved to be successful for the bulk of the data, but has also shown the special problems involved in the analysis of digitised pulses. In particular, the presence of undershoot on the pulse can result in inaccurate fits for a unimodal spline, as explained in Section 5.6.1. This problem can be overcome in future work by fitting a number of splines beginning and ending on the knots, and taking a weighted spline over the entire interval, (See Figure 7.1).

For this purpose, the number of knots will have to be increased beyond the range of the data set. Hence in Figure 7.1, the knots T_{i-3}, T_{i-2}, T_{i-1} are incorporated before the first knot T_i of the data set while the knots T_{i+4}, T_{i+5}, T_{i+6} are used after the last knot of the

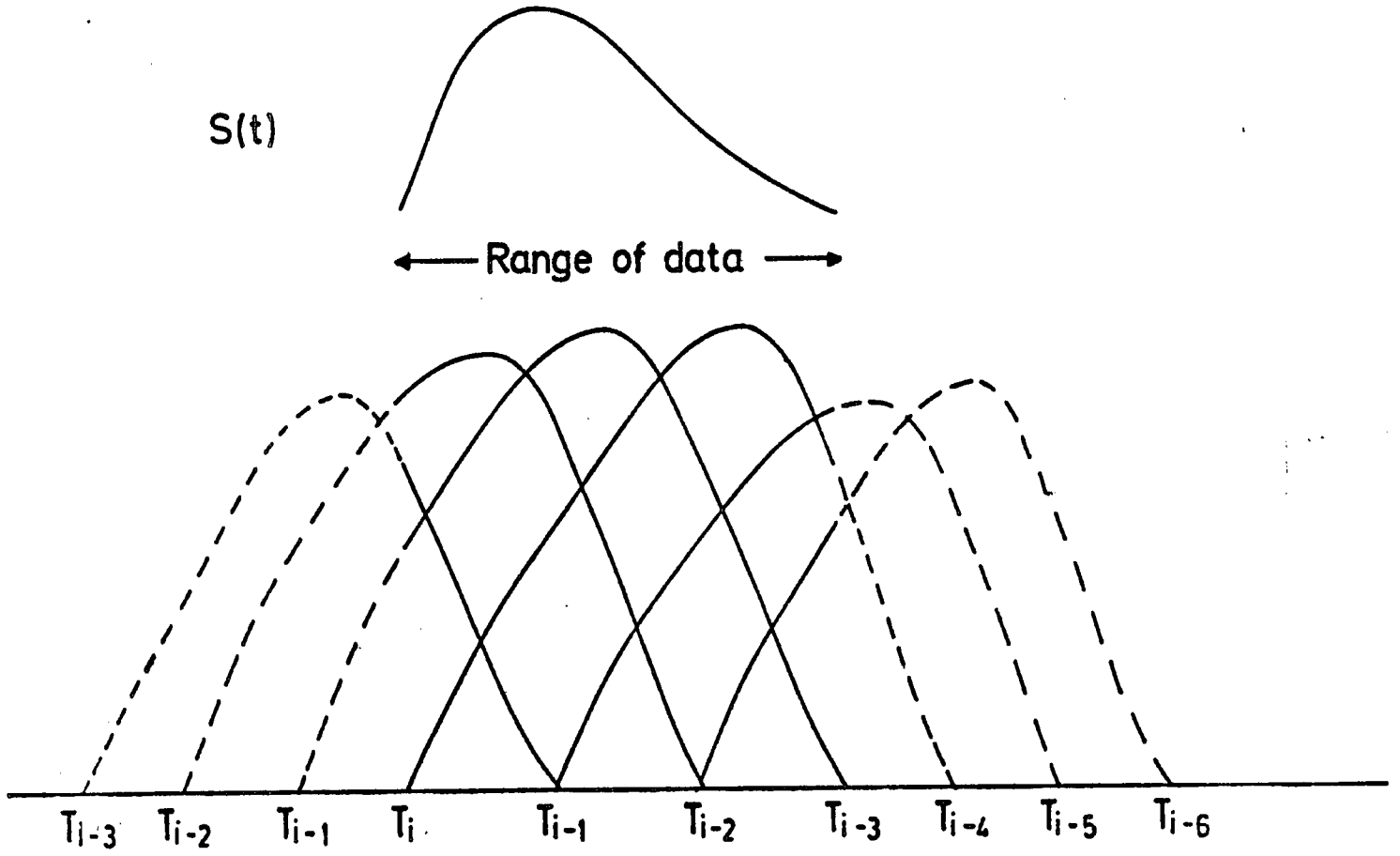

FIGURE 7.1

WEIGHTED B-SPLINES FOR NON-LINEAR LEAST SQUARES FIT.

data. Only part of each B-spline whose knots go beyond the data boundary will contribute to the final spline. These sub-splines will have less weighting than the sub-splines which span the data set.

The resultant spline $S(t)$ is therefore given by :

$$S(t) = C_i M_{4i}(t) + C_{i+1} M_{4i+1}(t) + C_{i+2} M_{4i+2}(t) + \ldots \quad \ldots + C_{i+n} M_{4i+n}(t) \qquad 7.1$$

where

$$M_{4i}(t) \ , \ M_{4i+1}(t) \ , \ \ldots \ , \ M_{4i+n}(t)$$

are the splines beginning and ending on the knots, and

$$C_i \ , \ C_{i+1} \ , \ \ldots \ , \ C_{i+n}$$

are the coefficients appropriate to each spline.

Hence, each sub-spline would be weighted according to the Section of the pulse it covers. Equation 7.1 may be solved by the matrix equation :

$$\begin{pmatrix} M_1(t_1) & M_2(t_1) & \ldots & M_n(t_1) \\ M_1(t_2) & \ldots & & M_n(t_2) \\ \vdots & & & \\ M_1(t_{n-1}) & \ldots & & M_n(t_{n-1}) \\ M_1(t_n) & \ldots & & M_n(t_n) \end{pmatrix} \times \begin{pmatrix} C_1 \\ C_2 \\ \vdots \\ C_{n-1} \\ C_n \end{pmatrix} = \begin{pmatrix} V_1 \\ V_2 \\ \vdots \\ V_{n-1} \\ V_n \end{pmatrix} \qquad 7.2$$

or

$$\underset{\sim}{M} \times \underset{\sim}{C} = \underset{\sim}{V} \qquad 7.3$$

M is a function of the knot positions only. Therefore, any pulse may be defined by :

$$S(t) = \sum_{j=1}^{n} C_j M_{j+1}(t) \qquad 7.4$$

Any future work involving pulse shape analysis could extend to extensive air shower energies below the primary energy range studied in this work, (i.e. primary energies down to $\sim 10^{15}$ eV). The reconstruction of these pulses can be accomplished by the use of weighted splines. Alternatively, since these pulses will be expected to very narrow, a reasonable estimate of the pulse width can be made from the two biggest slices.

The width parameter, M_2 , (See Chapter 4) can be used as a fast method of estimating the pulse width for these pulses. M_2 has been shown to relate closely to FWHM. From a sample of 30 showers from the Dugway data ($0^\circ < \theta \leq 35^\circ$; mean energy $\sim 3 \times 10^{16}$ eV) M_2 was calculated to find its variation with core distance. Figure 7.2 shows the dependence of M_2 on core distance. This solid line is the fit of the data points to :

$$M_2 = \alpha + \beta r^2 \qquad 7.5$$

It might be worthwhile to pursue the evaluation of M_2 in future work, because of the computing time it can save.

FIGURE 7.2

VARIATION OF M_2 WITH CORE DISTANCE FOR A SAMPLE OF THE DUGWAY DATA. ($0^\circ \leqq \theta \leqq 35^\circ$; mean energy $\simeq 3 \times 10^{16}$ eV)

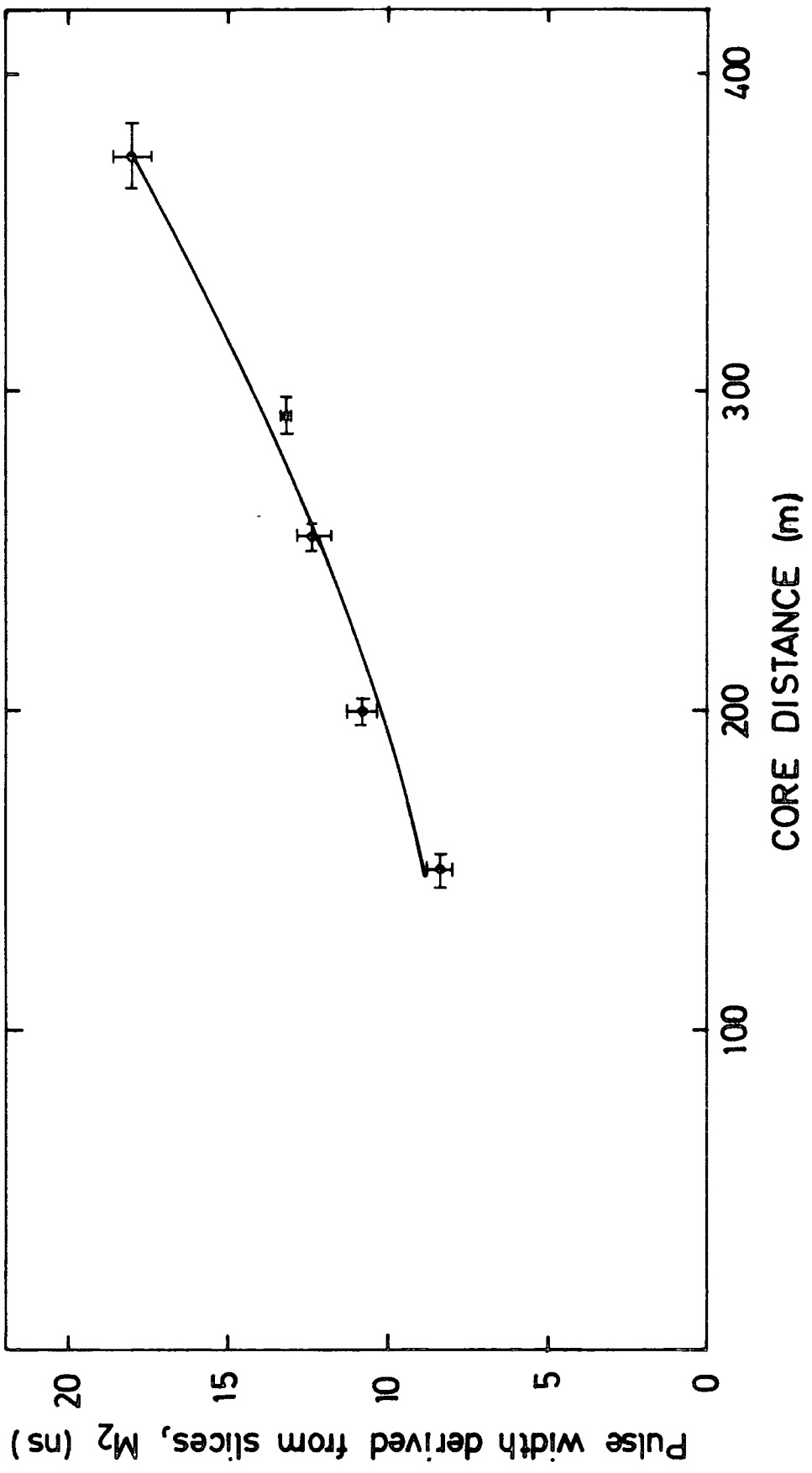
Pulse width derived from slices, M2 (ns)
0
5
10
15
20
100
200
300
400
CORE DISTANCE (m)

Further investigation could also be conducted into the relationship between the Cerenkov light pulse shape and the time delay between the light and particles, using computer simulations to interprete the measured time delay characteristics.

BIBLIOGRAPHY

Andam A., Chantler M.P., Craig M.A.B., Orford K.J., Shearer J.A.L., Turver K.E., and Walley G.M. 1979 Proc. 16th. Int. Conf. on Cosmic Rays, Kyoto, 9, 48

Andam A.A., Chantler M.P., Craig M.A.B., McComb T.J.L., Orford K.J., Turver K.E., and Walley G.M. 1981 Proc. 17th. Int. Conf. on Cosmic Rays, Paris, 6, 125

Andam A.A., Chantler M.P., Craig M.A.B., McComb T.J.L., Orford K.J., Turver K.E., and Walley G.M. 1981 Proc. 17th. Int. Conf. on Cosmic Rays, Paris, 6, 57

Berezinsky V.S., and Zatsepin G.T. 1969 Phys. Letts., 28B, 423

Berezinsky V.S., and Zatsepin G.T. 1971 Sov. J. Nucl. Phys., 13, 453

Blackett P.M.S. 1948 Physical Society Gassiot Committee Report, 34

Blake P.R., Connor P.J., Nash W.F., Mann D.M., and O'Connel B. 1979 Proc. 16th. Int. Conf. on Cosmic Rays, Kyoto, 8, 82

Boehm E., and Steinmann E.	1979	Proc. 16th. Int. Conf. on Cosmic Rays, Kyoto, 8, 294
Boley F.I., Baum J.H., Pasledge J.A. and Pereve J.H.	1961	Phys. Rev., 124, 1205
Boley F.I.	1964	Rev. Mod. Phys., 36, 792
Cerenkov P.A.	1934	Dokl. Akad. Nauk., 2, 451
Cerenkov P.A.	1937	Dokl. Akad. Nauk., 14, 101
Chantler M., Orford K.J., Shearer J.A.L., Turver K.E., and Walley G.M.	1979	Proc. 16th. Int. Conf. on Cosmic Rays, Kyoto, 9, 42
Chantler M., McComb T.J.L., Orford K.J., Shearer J.A.L., Turver K.E., and Walley	1979	Proc. 16th. Int. Conf. on Cosmic Rays, Kyoto, 9, 56
Chantler M.P., Craig M.A.B., McComb T.J.L., Orford K.J., Turver K.E., and Walley G. M.	1981	Proc. 17th. Int. Conf. on Cosmic Rays, Paris, 6, 121
Cox M.G.	1972	J. Inst. Maths. Applics., 10, 134
Craig M.A.B., McComb T.J.L., and Turver K.E.	1979	Proc. 16th. Int. Conf. on Cosmic Rays, Kyoto, 8, 180
Craig M.A.B., Orford K.J., Turver K.E., and Weekes T.C.	1981	Proc. 17th. Int. Conf. on Cosmic Rays, Paris, 1, 3

de Boor C. and Rice J.R. 1968 "Least Squares Cubic Spline Approximation I : Fixed Knots", CSD TR 20, Purdue University

de Boor C. and Rice J.R. 1968 "Least Squares Cubic Spline Approximation II : Variable Knots", CSD TR 21, Purdue University

Efimov N.N., Krasilnilov D.D. Khristiansen G.B., Shikalov F.V., and Kuzmin A.I. 1973 Proc. 13th. Int. Conf. on Cosmic Rays, Denver, 4, 2378

Feynman R.P. 1969 Phys. Rev. Letts., 23, 1415

Fletcher R. 1970 Computer Journal, 13, 317

Fomin Y.A. and Khristiansen G.B. 1971 Yad. Fiz., 14, 654

Frank I. and Tamm I. 1937 Dokl. Akad. Nauk., 14, 109

Gaisser T.K., McComb T.J.L., and Turver K.E. 1978 Rev. Mod. Phys., 50, 859

Ginzburg V.L., and Syrovatskii S.I. 1964 "The Origin of Cosmic Rays", Publ : Pergamon Press

Glushkov A.V., Grigoryev V.M., Efimov N.N., Pravdin M.I., Diminstein O.S., and Sokurov V.F. 1979 Proc. 16th. Int. Conf. on Cosmic Rays, Kyoto, 8, 158

Grigorov N.L., Gubin Yu.V. Rapoport I.D., Savenko I.A., Yakovlev B.M., Akimov V.V., and Nesterov V.E.	1971	Proc. 12th. Int. Conf. on Cosmic Rays, Hobart, 5, 1746
Grigoriev V.M., Efimov N.N., Kalmykov N.N., Nechin Yu.A., Prosin V.V., and Khristiansen G.B.	1978	Izvestiya Akademii Nauk. SSSR Seriya Fizicheskaya, 42, 1445
Grigoriev V.M., Efimov N.N., Kalmykov N.N., Nechin Yu.A., Prosin V.V. and Khristiansen G.B.	1978	Sov. J. Nucl. Phys., 27, 225
Hammond R.T., Orford K.J., Protheroe R.J., Shearer J.A.L., Turver K.E., Waddoup W.D., and Wellby D.W.	1978	Il Nuovo Cimento, 1C, 4, 315
Hess V.	1912	Physik. Zeitschr., 13, 1804
James M. and Roos M.	1975	Comp. Phys. Comm., 10, 413
Jelley J.V. and Galbraith W.	1953	Nature, 171, 349
Jelley J.V. and Galbraith W.	1955	J. Atmos. Terr. Phys., 6, 250, 304
Juliusson E.	1975	Proc. 14th. Int. Conf. on Cosmic Rays, Munich, 8, 2689

Kalmykov N.N., Nechin Yu.A., Prosin V.V., Fomin Yu.A., Khristiansen G.B., Berezhko I.A., Gregoriev V.M.,and Efimov N.N.	1979	Proc. 16th. Int. Conf. on Cosmic Rays, Kyoto, 9, 73
Kalmykov N.N., Nechin Yu.A., Prosin V.V., Efimov N.N., Fomin Yu.A., Khristiansen G.B., and Grigoriev V.M.	1981	Proc. 17th. Int. Conf. on Cosmic Rays, Paris, 6, 114
Kellerman W.	1976	Phys. Bull., June 1976, p246
Krasilnikov D.D.	1973	Proc. 13th. Int. Conf. on Cosmic Rays, 4, 2393
Krieger A.S. and Bradt H.V.	1969	Phys. Rev., 185, 1629
Kuhlmann J.D., Clay R.W., Liebing D.F., Thornton G.J., Gregory A.G. and Prescott J.R.	1981	J. Phys. G : Nucl. Phys., 7, L13
Linsley J. and Watson A.A.	1981	Phys. Rev. Letts., 46, 459
McComb T.J.L. and Turver K.E.	1981	Proc. 17th. Int. Conf. on Cosmic Rays, Paris, 6, 130
McCusker C.B.A.	1967	Proc. 10th. Int. Conf. on Cosmic Rays, S397

Malhotra P.K., Shulka P.G., Stephens S.A., Vijayalakohmi B., Boult J., Bowler M.G., Clapham V.M., Fowler P.H., Hackforth H.L., Keereetareep J. and Tovey S.N.	1966	Nature, 209, 2567
Marsden R.G., Elliot H., Hynds R.J. and Thambyahpillai T.	1976	Nature, 260, 491
Matano T., Miura I., Nagano M. Oda M., Shibata S., Tanaka Y., and Tanahashi G.	1963	Proc. 8th. Int. Conf. on Cosmic Rays, 4, 129
Millikan R.A.	1939	"Cosmic Rays", Publ : Cambridge University Press
Nelder J.A. and Mead R.	1967	Computer Journal, 7, 308
Nesterova N.M. and Chudakov A.	1955	Zh. Eksp. Teor., Fiz., 28, 384
Orford K.J. and Turver K.E.	1976	Nature, 264, 727
Orford K.J., Stubbs R.J. and Waddoup W.D.	1977	Nucl. Inst. and Meth., 146, 389
Orford K.J., Stephenson I., Turver K.E. and Walley G.M.	1981	Proc. 17th. Int. Conf. on Cosmic Rays, Paris, 6, 118
Osborne J.L., Wolfendale A.W., and Wdowczyk J.	1977	Proc. 15th. Int. Conf. on Cosmic Rays, Plodiv, 2, 182

Pollock A.M.T. and Watson A.A.	1975	Proc. 14th. Int. Conf. on Cosmic Rays, Munich, 2, 298
Pollard J.H.	1977	"A Handbook of Numerical and Statistical Techniques", Publ : Cambridge Univ. Press
Protheroe R.J.	1977	Ph.D. Thesis, Univ. of Durham
Protheroe R.J. and Turver K.E.	1977	Proc. 15th. Int. Conf. on Cosmic Rays, 8, 275
Protheroe R.J. and Turver K.E.	1979	Il Nuovo Cimento, 51A, 277
Rice J.R.	1969	"The Approximation of Functions", Vol. 2, Publ : Addison-Wesley, Reading, MA
Schoenberg I.J.	1946	Quart. Appl. Maths., 4, Part A: pp 45 - 49, Part B: pp 112 - 141
Shearer J.A.L.	1980	Ph.D. Thesis, Univ. of Durham
Smithsonian Astrophysical Observatory Staff	1969	Smithsonian Astrophysical Observatory Star Atlas, Cambridge, MA
Thornton G.J. and Clay	1978	J. Phys. G., 4, L193

Thornton G.J., Kuhlmann J.D., Liebing D.F., Clay R.W., Gregory A.G., Patterson J.R., and Prescott J.R. 1979 Proc. 16th. Int. Conf. on Cosmic Rays, Kyoto, 9, 103

Tornabene H. 1979 Proc. 16th. Int. Conf. on Cosmic Rays, Kyoto, 9, 99

Wilson C.T.R. 1901 Proc. Royal Soc., 68, 151

Wolfendale A.W. 1975 "The Origin of Cosmic Radiation", ed. J.L. Osborne and A.W. Wolfendale Publ : D. Riedel, Dordrecht-Holland